

Probing pi-conjugated polymers with circularly polarized light

Citation for published version (APA):

Lakhwani, G. (2009). *Probing pi-conjugated polymers with circularly polarized light*. [Phd Thesis 1 (Research TU/e / Graduation TU/e), Chemical Engineering and Chemistry]. Technische Universiteit Eindhoven.
<https://doi.org/10.6100/IR644292>

DOI:

[10.6100/IR644292](https://doi.org/10.6100/IR644292)

Document status and date:

Published: 01/01/2009

Document Version:

Publisher's PDF, also known as Version of Record (includes final page, issue and volume numbers)

Please check the document version of this publication:

- A submitted manuscript is the version of the article upon submission and before peer-review. There can be important differences between the submitted version and the official published version of record. People interested in the research are advised to contact the author for the final version of the publication, or visit the DOI to the publisher's website.
- The final author version and the galley proof are versions of the publication after peer review.
- The final published version features the final layout of the paper including the volume, issue and page numbers.

[Link to publication](#)

General rights

Copyright and moral rights for the publications made accessible in the public portal are retained by the authors and/or other copyright owners and it is a condition of accessing publications that users recognise and abide by the legal requirements associated with these rights.

- Users may download and print one copy of any publication from the public portal for the purpose of private study or research.
- You may not further distribute the material or use it for any profit-making activity or commercial gain
- You may freely distribute the URL identifying the publication in the public portal.

If the publication is distributed under the terms of Article 25fa of the Dutch Copyright Act, indicated by the "Taverne" license above, please follow below link for the End User Agreement:

www.tue.nl/taverne

Take down policy

If you believe that this document breaches copyright please contact us at:

openaccess@tue.nl

providing details and we will investigate your claim.

Probing π -conjugated polymers with circularly polarized light

PROEFSCHRIFT

ter verkrijging van de graad van doctor aan de
Technische Universiteit Eindhoven, op gezag van de
rector magnificus, prof.dr.ir. C.J. van Duijn, voor een
commissie aangewezen door het College voor
Promoties in het openbaar te verdedigen
op woensdag 2 september 2009 om 16.00 uur

door

Girish Lakhwani

geboren te Kanpur, India

Dit proefschrift is goedgekeurd door de promotor:

prof.dr.ir. R.A.J. Janssen

Copromotor:
dr. S.C.J. Meskers

This research has been financially supported by the Council for Chemical Sciences of the Netherlands Organization for Scientific Research (NWO-CW).

Cover Design: Girish Lakhwani
Printing: Gildeprint Drukkerijen, Enschede

A catalogue record is available from the Eindhoven University of Technology Library.

ISBN: 978-90-386-1952-1

In the memory of my late grandmother

Table of contents

1. Introduction	1
1.1 Preface	1
1.2 Chirality as a label	1
1.2.1 Intramolecular interactions	2
1.2.2 Intermolecular interactions	2
1.2.3 Cholesteric liquid crystals	3
1.3 Chiral π -conjugated polymers	3
1.4 Chiroptical spectroscopy	5
1.4.1 Optical absorption spectroscopy	5
1.4.2 Circular and linear dichroism	6
1.4.3 Circular selective reflection and scattering	7
1.4.4 Photoinduced (transient) absorbance and circular dichroism	7
1.4.5 Ellipsometry	8
1.5 The aim of the thesis	9
1.6 The layout of the thesis	9
References	12
2. The chiroptical properties of <i>chiral</i> polythiophene as a function of film thickness	15
2.1 Introduction	16
2.2 Experimental section	17
2.3 Results and discussion	17
2.4 Conclusion	21
References	21
3. Intensive chiroptical properties of <i>chiral</i> polyfluorenes associated with fibril formation	23
3.1 Introduction	24
3.2 Experimental	25
3.2.1 Material, film preparation and instrumentation	25
3.2.2 Static (SLS) and dynamic light scattering (DLS) set up	26
3.3 Results and discussion	26
3.3.1 CD of unannealed and annealed films of chiral polyfluorene at different film thicknesses	26
3.3.2 Analysis of the band shape of the intensive CD spectra	28
3.3.3 AFM on unannealed and annealed films of chiral polyfluorene	28
3.3.4 Aggregation of chiral polyfluorene in mixture of solvents	29
3.4 Conclusion	32
References	32

4. Circular differential scattering of light in films of <i>chiral</i> polyfluorene	33
4.1 Introduction	34
4.2 Experimental section	36
4.1.1 Materials	36
4.1.2 Tailor made circular selective reflection/scattering optical setup	36
4.1.3 Stokes-Müller analysis	38
4.1.4 Dissymmetry ratios	41
4.3 Results and discussion	42
4.3.1 Absorption, specular reflection and circular dichroism	42
4.3.2 Circular selective reflection	44
4.3.3 Circular selective scattering	48
4.4 Conclusion	50
References	51
5. Circular dichroism in photoinduced triplet-triplet absorption in <i>chiral</i> polyfluorene	53
5.1 Introduction	54
5.2 Experimental section	55
5.2.1 Materials and preparation	55
5.2.2 Tailor made photoinduced circular dichroism (PICD) set up	55
5.3 Results and discussion	58
5.3.1 PIA experiments on annealed <i>chiral</i> polyfluorene film	58
5.3.2 PICD experiments on annealed <i>chiral</i> polyfluorene film	59
5.4 Conclusion	62
References	62
6. β-phase in <i>chiral</i> polyfluorene forms via a precursor	65
6.1 Introduction	66
6.2 Experimental section	67
6.3 Results and discussion	67
6.3.1 α and β -phase	67
6.3.2 Precursor formation and stability	70
6.3.3 Dynamic light scattering on α and β -aggregates	71
6.3.4 Role of concentration in existence of α and β -phases	72
6.3.5 Role of cooling rate in existence of α and β -phases	74
6.3.6 Temperature dependent LD in α and β -phases	76
6.3.7 Phase diagram	77
6.4 Conclusion	78
References	79
7. Anisotropic dielectric tensor for <i>chiral</i> polyfluorene at optical frequencies	81
7.1 Introduction	82
7.2 Experimental and modeling section	85
7.2.1 Film preparation and instrumentation	85
7.2.2 Ellipsometry experiments and modeling	85
7.2.3 Optical constants of the substrates	88
7.2.4 Isotropy vs. anisotropy in the optical constants of <i>chiral</i> polyfluorene	89
7.3 Results and discussion	91
7.3.1 Anisotropic optical constants of <i>chiral</i> polyfluorene with thickness and substrate variation	91

7.3.2	Anisotropic optical constants of achiral polyfluorene	94
7.3.3	Chiral polyfluorene orientation distribution in thin films	96
7.3.4	Contribution of the pseudotensor G to the dielectric tensor of chiral polyfluorene	97
7.4	Conclusion	101
	References	101
8.	Probing charge carrier density in a p-n junction of conducting polymer and a layer of ZnO nanoparticles by spectroscopic ellipsometry	103
8.1	Introduction	104
8.2	Experimental section	106
8.3	Results and discussion	108
8.3.1	Formation of a quasi ohmic contact in an ITO/ZnO/PEDOT-PSS junction	108
8.3.2	Optical constants of layer of ZnO nanoparticles	109
8.3.3	Optical constants of layer of ZnO nanoparticles upon UV illumination (photodoping)	113
8.3.4	Anisotropic optical constants of PEDOT:PSS	115
8.3.5	Influence of UV illumination on pH-neutral PEDOT:PSS	117
8.3.6	Photodoping at ZnO nanoparticles/neutral-PEDOT:PSS interface	118
8.3.7	Estimation of a lower limit of the charge carrier density from Kelvin probe experiments	120
8.4	Conclusion	123
	References	123
	Conclusion	125
	Summary	129
	Samenvatting	133
	Acknowledgements	137
	Curriculum vitae	139

The important thing in science is not so much to obtain new facts
as to discover new ways of thinking about them.

- Sir William Bragg
British physicist (1862 - 1942)

Introduction

1.1 Preface

π -conjugated polymers¹ have a backbone consisting of alternating single and double bonds, which gives these polymers semiconducting properties. These semiconducting properties have been exploited in the last few decades for numerous applications in opto-electronic devices such as light-emitting diodes,² transistors,³ and photovoltaic cells⁴.

The optical and electronic properties of conjugated polymers strongly depend on the conformation of the backbone (folding) and on interchain contacts arising from aggregation (packing) of the polymer chains.⁵ Aggregation in polymer chains can occur in two ways: intermolecular (between polymer chains) and intramolecular (within a single polymer chain). Processing conditions used to deposit thin polymer films have a strong influence on the aggregation behavior of the polymer and largely affect the morphology of the layers.⁶ In fact one of the important unsolved questions that hinders the development in polymer electronics is how the film morphologies develop and how they can be influenced rationally by changing the deposition conditions. An understanding of the aggregation behavior of π -conjugated polymers can help to establish an approach to modify the morphology in a constructive way. This may allow for further optimization of the device performance.

To investigate the relation between the optical properties of π -conjugated polymers and their aggregates, we use *chiral* polymers. A chiral polymer has a chemical structure that is not superimposable on its mirror image. The asymmetric nature of the arrangements of the atoms in the molecules leads to a difference in the interaction with left and right circular polarized light (chiroptical effect). An example is the difference in the absorbance of left and right circular polarized light by chiral molecules. This is often referred to as circular dichroism (CD). Further sections divulge into introducing the technique and its use to investigate polymer aggregation.

1.2 Chirality as a label

The use of chiral materials is motivated by the fact that chiroptical effects in chiral polymers, molecular materials, and aggregates are very sensitive to various aspects of the molecular organization. The chirality in the materials acts as a probe allowing the use of CD

spectroscopy. The CD effect in the molecules and aggregates can arise from various types of molecular organization, as explained below:

1.2.1 Intramolecular interactions

CD in solutions of chiral biopolymers like DNA, proteins, and polypeptides, has been shown to be very sensitive to the helical conformation of the polymer backbone.^{7,8} This CD can be attributed to intramolecular interactions within the polymer backbone. Natural polymers like proteins derive their functionality from a particular conformation achieved upon folding (secondary structure). In addition, aggregation of proteins (quaternary structure) often plays a decisive role in determining functionality. These secondary and quaternary structures have been elucidated with the help of CD spectroscopy.⁹

In π -conjugated molecules like helicenes, which do not have any stereocenter as such, the asymmetry (chirality) comes from an intramolecular twist in adjacent benzene rings in either a clockwise or counterclockwise direction. These molecules can further self assemble (aggregate) in a corkscrew shape giving rise to a helical structure. Using CD spectroscopy, the different conformations of these molecules have been elucidated.¹⁰

1.2.2 Intermolecular interactions

With regard to intermolecular arrangements in molecular aggregates, it has been shown that CD and circular polarization of luminescence (CPL) are sensitive probes for the helical arrangements of molecules within the aggregate.¹¹ CD in intermolecular arrangements arises generally from exciton coupling.^{7,12}

When one of the two identical interacting molecules held in a chiral arrangement is excited with light, the excitation energy tends to resonate between the chromophores (part of the molecule that absorbs and emits light, imparting the color) of the molecules and exchange in excitation energy leads to two energy states: one higher and one lower compared to those of two non-interacting chromophores. This causes a splitting of the dipole transition (absorbance) into two transitions. This is known as exciton coupling. Sensitive to different molecular arrangements between molecules, circularly polarized light behaves selectively to these higher and lower energy transitions. This gives rise to CD.¹³

In a very dilute solution, the molecules are too far away from each other to interact. However, by increasing the concentration of the solution, or by adding a non-solvent to a molecularly dissolved solution, the molecules can be made to aggregate. The latter is often referred as solvent-induced aggregation. The intermolecular interactions giving rise to aggregation are non-covalent in nature and can arise from van der Waal forces, π - π interactions, or hydrogen bonding. Similar to crystallization, aggregation of molecules can also be induced by cooling down a molecularly dissolved solution, prepared at high temperature. This is generally referred to temperature-induced aggregation. These tools are often employed for aggregating molecules.

For small chiral molecules and oligomers, aggregation (self-assembly) has been well studied using chiroptical spectroscopy.¹⁴⁻¹⁷ Different models have been proposed to explain the growth of an aggregate.¹⁸ In a cooperative model, the binding constant of a molecule to the aggregate depends on the size of the aggregate, and often molecules bind stronger to larger aggregates. This implies that it is relatively difficult to form small aggregates. The aggregation process in this model therefore consists of two steps: first nucleus formation takes place and later the nucleus grows into a larger self-assembled structure. Small C_3 symmetrical disc shaped molecules provide a clear example of a cooperative self-assembly mechanism.^{19,20} In contrast, in an isodesmic self-assembly process²¹ the binding constant for a molecule to an aggregate is independent of the size of the aggregate. In this mechanism nucleation is not necessary and aggregates grow at a steady rate in the self-assembly process.

Using CD spectroscopy, it has been found that in order to form a chiral aggregate it is often not necessary that all the molecules in the aggregate are enantiomerically pure or have the same chirality. A variety of effects have been associated with this property: Seargent and soldiers',^{14,20,22} majority rules,²³ and chiral memory.²⁴ Quite often these effects involve changes in internal structure of pre-formed aggregates in addition to aggregate formation. The sensitivity of CD spectroscopy has made it possible to understand the subtle changes in the intermolecular interactions underlying in these mechanisms. With such an understanding on self-assembled systems, one can look forward to manipulating them into next generation materials for application,²⁵ in molecular electronics and biochemistry.

1.2.3 Cholesteric liquid crystals

CD effects have also been shown to be very sensitive to long range chiral molecular ordering. Such long range chiral molecular order occurs in cholesteric liquid crystals.²⁶ These materials can selectively reflect one of the circular polarizations of light when the pitch length of the helical molecular arrangement matches the wavelength of the light.²⁷ Under this condition the materials also show very large optical rotation. Interestingly, also optical transitions of achiral molecules can acquire large CD when dissolved in a cholesteric liquid crystal.^{28,29}

Considering π -conjugated molecules, it has been found that chiral nonameric oligofluorenes form cholesteric liquid crystals with long range order.³⁰

1.3 Chiral π -conjugated polymers

Unlike small molecules, such as oligomers and mesogens, π -conjugated polymers are polydisperse in nature. This makes the folding, aggregation, crystallization and phase behavior different from that of their small molecule counterparts. Knowledge on polymer aggregation is of high importance owing to the application in devices like solar cells, transistors, and light-emitting diodes. For example, well organized polymer structures can improve charge transport in these devices. Several types of chiral π -conjugated polymers have

been studied in the past, mainly with the aim of finding a relation between their (chir)optical properties and the molecular structure and arrangement in the condensed phase. Chiral derivatives of poly(*p*-phenylene vinylene),³¹⁻³³ polyfluorene,^{34,35} and polythiophene³⁶ are the most commonly studied polymers owing to their enormous device applications. However, the current understanding of polymer organization on a mesoscopic scale remains limited.

Similar to single and double stranded DNA, CD on polyacetylenes has shown formation of single and double stranded helices.³⁷ Intramolecular effects and intermolecular interaction with other chiral units have often been held responsible for such arrangements. However, a distinction between the individual contributions leading to the CD effect remains unclear. For oligothiophenes, CD arising due to intermolecular interactions has been explained by exciton coupling.¹³ However, for conjugate polymers such an explanation is lacking. Besides intramolecular and intermolecular interactions, long range ordering in the form of cholesteric phase is shown to exist in oligofluorenes.³⁰ CD effect arising due to long range ordering is seen in polyfluorenes as well,³⁸ but remains largely unexplained. It shows that a large number of factors may contribute to CD in conjugated polymers but the exact molecular origin of the CD effects is not well understood.

With the help of CD spectroscopy, aggregation in films as a function of polymer sidechains,³⁹ molecular weight,⁴⁰ processing conditions,^{32,41} annealing^{33,34,42} has been studied for some of aforementioned polymers. Apparently, a systematic study on chiroptical properties arising at various length scales (from nanometer to micrometer regime, i.e., larger than wavelength of light) due to intramolecular and intermolecular interactions is absent. For example, opposite CD effects can be seen in solutions of chiral polymers by changing the solvent conditions.^{32,43} These effects have been explained by proposing a formation of two different stacks under competitive conditions with respect to solvent polarity. For more non-polar solvent mixtures, a cholesteric arrangement of coplanar polymer chains has been proposed whereas for polar solvent mixtures a stack assembly of the twisted backbone chains has been assumed. However, a complete understanding of such anomalous changes in CD effects is still absent.

In some cases, it has been seen that the CD on thin films changes in magnitude and band shape upon annealing. This has often been suggested to be due to a change in molecular organization, which alters the bulk (intensive) property of the polymer. However the explanations are unclear because the link to the organization at molecular level has often been missing. For example, the CD in annealed films of a chiral poly(*p*-phenylene ethynylene) copolymer shows high dissymmetry in circularly polarized absorbance (g_{abs}), which arises during the annealing of the thin film.³³ The origins of such high g_{abs} values in absorbance were never discussed. In another case, it was noticed that CD in thin films of a chiral polyfluorene increases in magnitude with annealing temperature.⁴² This has been related to increased intermolecular order upon annealing, but has never been studied in detail. Furthermore, in some cases it has been shown that pristine films of a polymer spin coated from different solvents or solvent mixtures give different CD spectra.⁴¹ Such effects have been attributed to different molecular arrangements.

The aim of this thesis is threefold: to differentiate between intensive (independent of the size of the system) and extensive (dependent on the size of the system) chiroptical properties, to establish the origin of the chiroptical properties at a molecular level, and to distinguish various CD effects arising in polymer aggregates at different length scale interactions.

1.4 Chiroptical spectroscopy

This thesis addresses optical, chiroptical, conformational, and electronic properties of π -conjugated polymers in films using polarized light. Chirality serves as a spectroscopic ‘label’ allowing us to investigate aggregation and organization using a large variety of spectroscopic techniques involving the (circular) polarization of light, some of which are mentioned below:

1.4.1 Optical absorption spectroscopy

Absorption of light is the result of interaction of electromagnetic (light) radiation with molecules in a material.⁴⁴ The linear optical characteristics can be described in terms of a complex refractive index \tilde{n} . A representation of an electromagnetic wave \mathbf{E} with initial amplitude \mathbf{E}_0 propagating through a material with time, t , can be written as:

$$\mathbf{E}(\mathbf{r}, t) = \mathbf{E}_0 \exp(i\tilde{n}\mathbf{k}_0 \cdot \mathbf{r}) \exp(-i\omega t) \quad (1)$$

where \mathbf{r} is the position vector, ω is the angular frequency, and \mathbf{k}_0 the is the wave vector of incident light. The complex index of refraction $\tilde{n} (= n + i\kappa)$ mentioned in this equation governs the phase and amplitude change of the wave as it propagates through the medium. n stands for refractive index which describes the velocity v with which an optical signal propagates inside the material relative to the speed of light in vacuum ($v = c/n$). The extinction index κ in the complex refractive index is the measure of decay in amplitude upon propagation. This is related to the absorbance in the following manner:

$$\alpha = \frac{4\pi\kappa}{\lambda_0} \quad (2)$$

where λ_0 is the wavelength of light in free space and α is the absorption or attenuation coefficient of the material. It describes the attenuation of the intensity of light propagating in the material along x

$$I(x) = I_0 \exp(-\alpha x) \quad (3)$$

where $I(x)$ is the intensity at position x and I_0 is the incident light intensity at $x = 0$. The absorbance A by a material is defined as:

$$A = -\log_{10} \frac{I}{I_0} = \ln(10)\alpha l \quad (4)$$

where I is the intensity of light transmitted through a film with thickness l . An electromagnetic wave can have different polarizations. An arbitrary polarization of light can always be resolved into two unique components. Well known are the linear polarizations of light, where the electric field oscillates in a unique direction perpendicular to the wave vector \mathbf{k} , describing the direction of the wave. In circular polarized light, the electric field oscillates in a helical fashion and can be either right handed or left handed. A circular polarized wave can be resolved into two linear components; one along y and one along z , that are phase shifted by $\lambda/4$ with respect to each other. Elliptical polarizations have a mixed character containing both circular and linear polarized components.

Techniques like absorbance and photoluminescence are generally based on interaction of unpolarized light with matter, whereas circular dichroism spectroscopy involves circularly polarized light to study difference in absorbance by a material when it interacts with left and right circularly polarized light.

1.4.2 Circular and linear dichroism

Circular dichroism (CD) refers to a difference in absorbance (A) for left and right circular polarizations of light ($\Delta A = \text{CD} = A_L - A_R$), displayed by chiral molecules and chiral materials. For example, a simple exciton model⁷ explains a bisignate CD signal arising due to intermolecular interactions between molecules.¹³

The extent to which a molecule behaves differently to right and left circularly polarized light can be expressed by its g value (dissymmetry ratio):

$$g_{\text{abs}} = \frac{\Delta A}{A} = \frac{2(A_L - A_R)}{A_L + A_R} \quad (5)$$

In dilute solutions of chiral molecules, the intermolecular interaction is minimized and the dissymmetry ratio g is an intensive property of the solution, *i.e.* it does not depend on sample size or concentration (provided that concentration is low enough to avoid intermolecular interactions among the solute molecules). The g value is essentially a molecular property under these conditions.

For chiral molecular materials, the dissymmetry ratio g is no longer necessarily an intrinsic property of the material. An example of this is provided by cholesteric liquid crystals where the selectivity in the reflection of light depends strongly on the thickness of the film.⁴⁵ Another example is provided by thermally annealed film of chiral polyfluorene, where the dissymmetry ratio varies strongly with the thickness of the polymer film.³⁸

Linear dichroism works on the same principle as CD but utilizes linearly polarized light instead. This technique can help in knowing the alignment of the polymer chains in a film or solution.¹² Coupled together with linear birefringence, it can also cause artifacts in circular dichroism measurements.⁴⁶

1.4.3 Circular selective reflection and scattering

Previously we saw that CD is a measure of differential circularly selective absorbance. However, typical CD experiments also involve detection of the transmitted light. Apart from transmission and absorbance, incident light may also be reflected or scattered. For chiral molecules and materials the efficiency of these processes may also depend on the circular polarization of the light. For example, for cholesteric liquid crystalline materials, it is well known that if the pitch of the cholesteric helix is similar to the wavelength of incident light, one of the circularly polarized components of the light is completely reflected.⁴⁷ The reflected circularly polarized light has identical handedness as of the cholesteric helix. This technique has been often employed to study liquid crystalline materials and molecules showing a cholesteric phase.³⁴

Circular differential scattering⁴⁸ has been used to study biomolecules. The scattering contribution has been evaluated for large conglomerates of nucleic acids.⁴⁹ The studies have helped in differentiating a true CD effect resulting from transmission normal to the substrate to contribution from scattered light. These studies have been helpful in elucidating the structural information of aggregated proteins⁵⁰ or chloroplasts.⁵¹

1.4.4 Photoinduced (transient) absorbance and circular dichroism

All techniques mentioned above involve transitions from the singlet ground level to an excited singlet state. These transitions provide information about the ground state conformation of the material. A singlet state in a molecule signifies that all electrons are spin paired, whereas a triplet state signifies that one sets of spins in unpaired.

Photoinduced absorbance (PIA) is a technique that probes absorbance of light by a molecule already in an excited state, inducing a transition to a higher lying excited state. This technique provides information on excited states after they have undergone relaxation processes subsequent to their initial creation. The excited states involved can be either singlet or triplet in nature. Singlet states are generally very short-lived (picosecond time range), whereas triplets are comparatively long-lived excited states (nanosecond to milliseconds).

PIA experiments can also be performed using circularly polarized light as the probe (photoinduced circular dichroism, PICD). This transient circular dichroism technique provides information on the molecular conformation in the excited state and has been used to study various biomolecules like tRNA⁵² and heme proteins.⁵³

1.4.5 Ellipsometry

Ellipsometry is an optical technique that uses reflection of light. It is commonly used to study bulk materials and multilayered thin films.

The basic experiment involves reflection of incident polarized light off the sample and subsequent detection. These experiments involve different polarization components of the light. One component is parallel to the plane of incidence denoted as ‘ p ’ whereas the other component is perpendicular to the plane and is denoted by ‘ s ’. Linearly polarized light is the case where both p and s components are in phase with each other, whereas a circularly polarized light results when the phase difference between them is 45 degrees. Any other phase difference results in elliptically polarized light.

Comparison of polarization components before and after reflection yields information about the sample, which is in form of Ψ (amplitude) and Δ (phase) as mentioned below:

$$\tan(\psi)e^{i\Delta} = \frac{R_p}{R_s} \quad (6)$$

where R_p and R_s are the complex Fresnel reflection coefficients for p and s polarized light respectively.

$$\begin{aligned} R_p &= \frac{n_0 \cos \theta_{\text{transmission}} - \tilde{n} \cos \theta_{\text{incidence}}}{n_0 \cos \theta_{\text{transmission}} + \tilde{n} \cos \theta_{\text{incidence}}} \\ R_s &= \frac{n_0 \cos \theta_{\text{incidence}} - \tilde{n} \sin \theta_{\text{transmission}}}{n_0 \cos \theta_{\text{incidence}} + \tilde{n} \sin \theta_{\text{transmission}}} \end{aligned} \quad (7)$$

where n_0 is the refractive index of the incident light medium (which in this case is air), \tilde{n} is the refractive index of the medium (sample), and θ is the angle of the incident/transmitted light to the normal of the substrate. Ellipsometry is primarily used to determine the n and κ components of the complex refractive index \tilde{n} . From these the dielectric constant of the material can be determined.

The material under study may be isotropic or anisotropic. Let \tilde{n}_x , \tilde{n}_y , and \tilde{n}_z denote the complex refractive indices along x , y , and z directions. Here the directions x and y lie parallel to the plane of the substrate (in-plane) and the z direction is perpendicular to it (out-of-plane). The former is also referred to the ordinary component, while the latter to extraordinary component of refractive index.

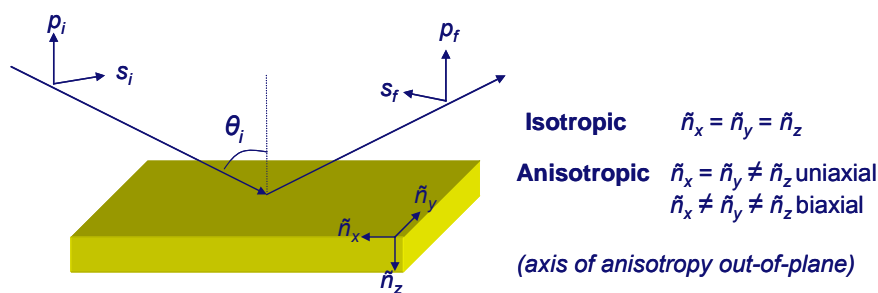


Figure 1: Isotropy and anisotropy in thin films. p and s are the polarization components of light whereas subscripts i and f stand for initial and final states during reflection.

If the optical constants do not depend on orientation, then $\tilde{n}_x = \tilde{n}_y = \tilde{n}_z$ and the film is isotropic in nature. In all other cases the film is anisotropic. Anisotropy can be uniaxial (e.g. $\tilde{n}_x = \tilde{n}_y \neq \tilde{n}_z$) or biaxial ($\tilde{n}_x \neq \tilde{n}_y \neq \tilde{n}_z$) as illustrated mentioned in Figure 1. For uniaxial systems, the axis of anisotropy is the axis along which the symmetry is broken (\tilde{n}_z in Figure 1).

Anisotropy at the molecular level can be one of the underlying causes of the macroscopic anisotropy of a molecular material but molecular anisotropy does not necessarily lead to macroscopic anisotropy. The macroscopic properties also depend of the orientation distribution of the molecules. If this is isotropic the molecular anisotropy can average out in the bulk. This is expected for films of a completely amorphous molecular material. At a single molecule level, anisotropy or isotropy depends on the structure of the molecule or single polymer chain.

1.5 The aim of the thesis

As discussed above the optoelectronic properties of conjugated polymers depend in a complex way on the conformation of the polymer backbone, interchain contacts arising from aggregation of polymer chains and long range intermolecular order. Thus, the CD effects in films of chiral π -conjugated polymer may originate on the molecular, on the intermolecular, or on the macroscopic length scale. There have been a few systematic studies on the origin of CD and there is uncertainty as to which length scale is the most relevant for understanding of the chiroptical properties.

The aim of the thesis is to use circularly polarized light as a spectroscopic tool to understand the molecular organization associated to chiroptical properties of conjugate polymers at various structural levels.

1.6 The layout of the thesis

As the title of the thesis suggests, (circularly) polarized light is used to investigate the molecular organizations giving rise to chiroptical response of the chiral polymeric materials. The chiral π -conjugated polymers investigated in this thesis are illustrated in Figure 2.

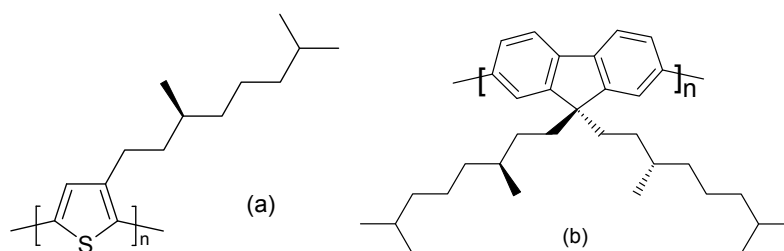


Figure 2. Structures of (a) poly[3-((3S)-3,7-dimethyloctyl)thiophene] and (b) poly[9,9-bis((3S)-3,7-dimethyloctyl)-2,7-fluorene].

The thesis is divided into eight chapters including the introduction (*Chapter 1*). Before making any progress into probing various aggregation states of chiral polymers via circularly polarized light, it is important to understand intensive and extensive properties of chiral π -conjugated polymers in general.

Chapter 2 takes an example of a chiral polythiophene to study its intensive or extensive properties. The chapter deals with the thickness dependence of CD in films of a chiral polythiophene (Figure 2a). It shows that circular polarization in absorbance, g_{abs} is independent of the film thickness and that it can be considered as an intensive property or bulk, a physical property of the material which is invariant to the size or amount of sample. Thus circular polarization in absorbance can be associated to arise on a molecular level at the site of photon absorbance.

Learning from the previous example on intensive properties in Chapter 2, similar experiments are described in *Chapter 3* on pristine films of a chiral polyfluorene (Figure 2b). Here g_{abs} is also found to be independent of film thickness. With help of AFM and solvent-induced aggregation studies, the possible origin of the intensive g_{abs} was found to arise from a helical arrangement of polymer chains within fibrillar aggregates. Upon annealing the films, g_{abs} is found to become dependent on film thickness. Therefore, for annealed films, g_{abs} is an extensive property (not a bulk property but dependent on size and amount) of the material arising from mesoscopic ordering in the film. In the following chapters, polymer organization in the chiral polyfluorene is studied more into detail.

This mesoscopic ordering induced by annealing of the film gives rise to high CD effects compared to unannealed films. Remarkably, CD effects are also observed for the thick annealed films outside the region of polyfluorene absorbance ($\lambda > 450$ nm). *Chapter 4* looks further into annealed films of chiral polyfluorene with an aim to understand the origin of these uncharacteristic CD effects. Using a tailor-made chiroptical setup, CD effects outside the absorbance band are found to originate from circularly polarized scattering from liquid crystalline domains in the film.

With mesoscopic ordering having an influence on CD effects outside the absorbance range, *Chapter 5* investigates if the high CD effects for annealed films (chiral polyfluorene), also exists in excited-state absorption. Photoinduced triplet-triplet absorption is found to show circular dichroism. This is interpreted to arise from the interaction of the local linear

polarization in triplet-triplet absorption in combination with the linear birefringence of the surrounding polymer matrix.

In previous chapters, we can find that the main focus on polymer organization was in films. Unlike films, the polymer organization in solutions is dynamic in nature. For example, during spincoating a film, polymer organization is induced by evaporation of solvent and subsequent vitrification. This causes a confined organization of polymer chains in a solid state. Whereas in solutions, manipulating the processing conditions (like concentration, temperature, solvent) allows one to study interaction of few chains to many chains. This provides a handle to study finer aspects of polymer interaction in aggregates. As discussed before, polymer aggregation in solution can be induced either via mixing of a good solvent and bad solvent (solvent-induced) or by cooling a molecular dissolved solution (temperature-induced). Solvent-induced studies in solutions of chiral polyfluorene are briefly described in *Chapter 3*, whereas temperature-induced aggregation of the same are explained in *Chapter 6*.

Through temperature-induced aggregation, so called α and β -aggregates are identified by different CD spectra. Cooling down the dilute solutions of molecular dissolved polymer often yielded in formation of α -aggregates, whereas slow controlled cooling of concentrated solutions led to formation of β -aggregates. β -aggregates were found to appear only via formation of a precursor involving cooperative folding of two or more chains.

We know that by using CD spectroscopy one essentially probes into differential absorption of the left and right circularly polarized light by the sample. This is done by detecting the intensity of complementary transmitted light. Whatever is not transmitted is assumed to be absorbed. However a part of light that is not transmitted, contributes to reflection. In *Chapter 7*, information on polymer organization is obtained from this reflection contribution by use of spectroscopic ellipsometry (SE). For achiral π -conjugated polyfluorene, SE has revealed anisotropy in thin films whereas for chiral polymer such studies were never done because of the lack of understanding of optical rotation in reflection of light. Here in *Chapter 7*, the anisotropic dielectric tensor of chiral polyfluorene is determined via SE and CD. Chirality in the polymer results in off-diagonal matrix elements in the dielectric tensor. Consequences of these off-diagonal terms in the reflection of light are further discussed. Furthermore, with help of SE and CD studies, origin of intensive CD in chiral polyfluorene (as studied in *Chapter 3*) is proposed.

Having learnt about circularly polarized light and its exploits in unearthing the polymer organization in films and solutions, its utility in understanding device phenomena was an obvious next step. With the help of *Chapter 8*, thesis reflects on the application oriented spectroscopic studies that can be performed using polarized light. *Chapter 8* utilizes spectroscopic ellipsometry to study device phenomena for a quasi p-n Ohmic junction. The ZnO/PEDOT:PSS n-p junction is studied under UV illumination. PEDOT:PSS is π -conjugated polymer often used as a hole transporting polymer in photovoltaic devices. UV illumination dopes the layer of ZnO nanoparticles and an excess of free charge carriers are

generated in the conduction band of ZnO. This causes the p-n junction to behave as an Ohmic contact for which the charge carrier density and depletion width are determined.

References

1. Feast, W.J.; Tsibouklis, J.; Pouwer, K.L.; Groenendaal, L.; Meijer, E.W. *Polymer* **1996**, *37*, 5017.
2. (a) Tang, C.W.; van Slyke, S.A. *Appl. Phys. Lett.* **1987**, *51*, 913. (b) Burroughes, J.H.; Bradley, D.D.C.; Brown, A.R.; Marks, R.N.; Mackay, K.; Friend, R.H.; Burn, P.L.; Holmes, A.B. *Nature* **1990**, *347*, 539. (c) Friend, R.H.; Gymer, R.W.; Holmes, A.B.; Burroughes, J.H.; Marks, R.N.; Taliani, C.; Bradley, D.D.C.; Dos Santos, D.A.; Brédas, J.L.; Loglund, M.; Salaneck, W.R. *Nature* **1999**, *397*, 121.
3. (a) Dimitrakopoulos, C.D.; Malenfant, P.R.L. *Adv. Mater.* **2002**, *14*, 99. (b) Siringhaus, H.; Brown, P.J.; Friend, R.H.; Nielsen, M.M.; Bechgaard, K.; Langeveld-Voss, B.M.W.; Spiering, A.J.H.; Janssen, R.A.J.; Meijer, E.W.; Herwig, P.; de Leeuw, D.M. *Nature* **1999**, *401*, 685. (c) Brown, A.R.; Pomp, A.; Hart, C.M.; de Leeuw, D.M. *Science* **1995**, *270*, 972.
4. (a) Brabec, C.J.; Dyakonov, V.; Parisi, J.; Saricifitei, N.S. (Eds.) *Organic Photovoltaics: Concepts and Realisation, Springer Series in Material Science*, Springer-Verlag, London **2003**, *60*. (b) Huynh, W.U.; Dittmer, J.J.; Alivisatos, A.P.; *Science* **1995**, *295*, 2425.
5. (a) Chen, S.H.; Su, A.C.; Han, S.R.; Chen, S.A.; Lee, Y.Z. *Macromolecules*, **2004**, *37*, 181. (b) Apperloo, J.J.; Janssen, R.A.J.; Malenfant, P.R.L.; Fréchet, J.M.J. *J. Am. Chem. Soc.* **2001**, *123*, 6916. (c) Peng, K.Y.; Chen, S.A.; Fann, W.S.; Chen, S.H.; Su, A.C. *J. Phys. Chem. B* **2005**, *109*, 9368.
6. (a) Yang, X.N.; Loos, J.; Veenstra, S.C.; Verhees, W.J.H.; Wienk, M.M.; Kroon, J.M.; Michels, M.A.J.; Janssen, R.A.J. *Nano Lett.* **2005**, *5*, 579. (b) Xin, H.; Kim, F.S.; Jenekhe, S.A. *J. Am. Chem. Soc.* **2008**, *130*, 5424.
7. Berova, N.; Nakanishi, K.; Woody, R.W. *Circular Dichroism: principles and application*, Wiley-VCH **2000**.
8. Woody, R.W. *Methods in Enzymology: Biochemical Spectroscopy* **1995**, *246*, 34.
9. (a) Chen, Y.H.; Yang, J.T.; Chau, K.H. *Biochemistry* **1974**, *13*, 3350. (b) Chen, Y.H.; Yang, J.T.; Martinez, H.M. *Biochemistry* **1972**, *11*, 4120.
10. Grimme, S.; Harren, J.; Sobanski, A.; Vogtle, F. *Eur. J. org. Chem.* **1998**, *8*, 1491. (b) Phillips, K.E.S.; Katz, T.J.; Jockusch, S.; Lovinger, A.J.; Turro, N.J. *J. Am. Chem. Soc.* **2001**, *123*, 11899.
11. Spano, F.C.; Meskers, S.C.J.; Hennebicq, E.; Beljonne, D. *J. Am. Chem. Soc.* **2007**, *129*, 7044.
12. Rodger, A.; Nordén, B. *Circular Dichroism and Linear Dichroism*, Oxford University Press **1997**.
13. Langeveld-Voss, B.M.W.; Beljonne, D.; Shuai, Z.; Janssen, R.A.J.; Meskers, S.C.J.; Meijer, E.W.; Brédas, J.L. *Adv. Mater.* **1998**, *10*, 1343.
14. Schenning, A.P.H.J.; Kilbinger, A.F.M.; Biscarini, F.; Cavallini, M.; Cooper, H.J.; Derrick, P.J.; Feast, W.J.; Lazzaroni, R.; Leclere, P.; McDonnell, L.A.; Meijer, E.W.; Meskers, S.C.J. *J. Am. Chem. Soc.* **2002**, *124*, 1269.
15. Brunsveld, L.; Zhang, H.; Glasbeek, M.; Vekemans, J.A.J.M.; Meijer, E.W. *J. Am. Chem. Soc.* **2000**, *122*, 6175.
16. Mateos-Timoneda, M.A.; Crego-Calama, M.; Reinhoudt, D.N. *Chem. Soc. Rev.* **2004**, *33*, 363.
17. Hoeben, F.J.M.; Jonkheijm, P.; Meijer, E.W.; Schenning, A.P.H.J. *Chem. Rev.* **2005**, *105*, 1491.
18. Martin, R.B. *Chem. Rev.* **1996**, *96*, 3043.
19. Jonkheijm, P.; van der Schoot, P.; Schenning, A. P. H. J.; Meijer, E. W. *Science* **2006**, *313*, 80.
20. Smulders M.M.J.; Schenning, A.P.H.J.; Meijer, E.W. *J. Am. Chem. Soc.* **2008**, *130*, 606.
21. Chen, Z.J.; Stepanenko, V.; Dehm, V.; Prins, P. Siebbeles, L.D.A.; Seibt, J.; Marquetand, P.; Engel, V.; Würthner, F. *Chem. Eur. J.* **2007**, *13*, 436.

22. (a) Brunsveld, L.; Schenning, A.P.H.J.; Broeren, M.A.C.; Janssen, H.M.; Vekemans, J.A.J.M.; Meijer, E.W. *Chem. Lett.* **2000**, *3*, 292. (b) George, S.J.; Tomovic, Z.; Smulders, M.M.J.; de Greef, T.F.A.; Leclere, P.E.L.G.; Meijer, E.W.; Schenning, A.P.H.J. *Angew. Chem.* **2007**, *46*, 8206.
23. van Gestel, J.; Palmans, A.R.A.; Titulaer, B.; Vekemans, J.A.J.M.; Meijer, E.W. *J. Am. Chem. Soc.* **2005**, *127*, 5490.
24. (a) Lauceri, R.; Purrello, R. *Supramol. Chem.* **2005**, *17*, 61. (b) Purrello, R.; Raudino, A.; Scolaro, L.M.; Loisi, A.; Bellacchio, E.; Lauceri, R. *J. Phys. Chem. B* **2000**, *104*, 10900.
25. (a) Lindsey, J.S. *New J. Chem.* **1991**, *15*, 153-180. (b) Dankers, P.Y.W.; Meijer, E.W. *Bull. Chem. Soc. Jpn.* **2007**, *80*, 2047.
26. Leforestier, A.; Livolant, F. *Biophys. J.* **1993**, *65*, 56.
27. Vries, H.D. *Acta Cryst.* **1951**, *4*, 219.
28. Saeva, F.D.; Wysocki, J.J. *J. Am. Chem. Soc.* **1971**, *93*, 5928 and references therein.
29. (a) Thisayukta, J.; Nakayama, Y.; Kawachi, S.; Takezoe, H.; Watanabe, J. *J. Am. Chem. Soc.* **2000**, *122*, 7441. (b) Watanabe, J.; Fukuda, Y.; Gehani, R.; Uematsu, I. *Macromolecules* **1984**, *17*, 1004.
30. Geng, Y.H.; Trajkovska, A.; Culligan, S.W.; Ou, J.J.; Chen, H.M.P.; Katsis, D.; Chen, S.H. *J. Am. Chem. Soc.* **2003**, *125*, 14032.
31. Meskers, S.C.J.; Peeters, E.; Langeveld-Voss, B.M.W.; Janssen, R.A.J. *Adv. Mater.* **2000**, *12*, 589.
32. Satrijo, A.; Swager, T.M. *Macromolecules* **2005**, *38*, 4054.
33. Wilson, J.N.; Steffen, W.; McKenzie, T.G.; Lieser, G.; Oda, M.; Neher, D.; Bunz, U.H.F. *J. Am. Chem. Soc.* **2002**, *124*, 6830.
34. Oda, M.; Nothofer, H.G.; Scherf, U.; Sunjic, V.; Richter, D.; Regenstein, W.; Neher, D. *Macromolecules* **2002**, *35*, 6792.
35. Oda, M.; Nothofer, H.G.; Lieser, G.; Scherf, U.; Meskers, S.C.J.; Neher, D. *Adv. Mater.* **2000**, *12*, 362.
36. (a) Bouman, M.M.; Havinga, E.E.; Janssen, R.A.J.; Meijer, E.W. *Mol. Cryst. Liq. Cryst.* **1994**, *256*, 439. (b) Koeckelberghs, G.; Cornelis, D.; Persoons, A.; Verbiest, T. *Macromol. Rapid Commun.* **2006**, *27*, 1132. (c) Koeckelberghs, G.; Vangheluwe, M.; Persoons, A.; Verbiest, T. *Macromolecules* **2007**, *40*, 8142.
37. (a) Maeda, K.; Mochizuki, H.; Watanabe, M.; Yashima, E. *J. Am. Chem. Soc.* **2006**, *128*, 1639.
38. Craig, M.R.; Jonkheijm, P.; Meskers, S.C.J.; Schenning, A.P.H.J.; Meijer, E.W. *Adv. Mat.* **2003**, *15*, 1435.
39. (a) Palsson, L.O.; Vaughan, H.L.; Monkman, A.P. *J. Chem. Phys.* **2006**, *125*, 164701. (b) Tang, H.Z.; Fujiki, M.; Motonaga, M. *Polymer* **2002**, *43*, 6213.
40. (a) Abbel, R.; Schenning, A.P.H.J.; Meijer, E.W. *Macromolecules*, **2008**, *41*, 7497. (b) Kline, R.J.; McGehee, M.D.; Kadnikova, E.N.; Liu, J.S.; Fréchet, J.M.J.; Toney, M.F. *Macromolecules*, **2005**, *38*, 3312.
41. Satrijo, A.; Meskers, S.C.J.; Swager, T.M. *J. Am. Chem. Soc.* **2006**, *128*, 9030.
42. Oda, M.; Meskers, S.C.J.; Nothofer, H.G.; Scherf, U.; Neher, D. *Synth. Met.* **2000**, *111*, 575.
43. Goto, H.; Okamoto, Y.; Yashima, E. *Macromolecules* **2002**, *35*, 4590.
44. Schellman, J.; Jensen, H.P. *Chem. Rev.* **1987**, *87*, 1359.
45. Katsis, D.; Chen, P.H.M.; Mastrangelo, J.C.; Chen, S.H.; Blanton, T.N. *Chem. Mater.* **1999**, *11*, 1590.
46. Wolffs M.; George S.J.; Tomovic, Z.; Meskers, S.C.J.; Schenning, A.P.H.J.; Meijer, E.W. *Angew. Chem.* **2007**, *46*, 8203.
47. (a) Chandrasekhar, S. *Liquid Crystals*, Cambridge University Press **1992**. (b) de Gennes, P.G. *The Physics of Liquid Crystals*, Clarendon Press, Oxford **1974**.
48. Bustamante, C.; Tinoco, I. Jr.; Maestre, M.F. *Proc. Natl. Acad. Sci. USA* **1983**, *80*, 3568.
49. Keller, D.; Bustamante, C. *J. Chem. Phys.* **1986**, *84*, 2972.
50. Phillips, C. L.; Mickols, W. E.; Maestre, M. F.; Tinoco, I., Jr. *Biochemistry* **1986**, *25*, 7803.
51. Gregory, R.P.F.; Raps, S. *Biochem. J.* **1974**, *142*, 193.
52. Milder, S.J.; Weiss, P.S.; Kliger, D.S. *Biochem.* **1989**, *28*, 2258.
53. Dartigalongue, T; Hache, F. *Chem. Phys. Lett.* **2005**, *415*, 313.

The chiroptical properties of *chiral* polythiophene as a function of film thickness*

Abstract. Circular dichroism (CD) and circular polarization of the luminescence (CPL) of spin coated films of chiral, regioregular poly[3-((3*S*)-3,7-dimethyloctyl)thiophene] are investigated as a function of their film thickness (50-500 nm). The degrees of circular polarization in absorption (g_{abs}) and in emission (g_{lum}) do not significantly depend on the film thickness and can therefore be considered as an intrinsic property of the material. This is consistent with the circular polarization in absorption and emission originating on a molecular level from a difference in the probability for absorption and emission of left and right handed circular polarized photons at the site of the optical excitation.

* Girish Lakhwani, Guy Koeckelberghs, Stefan C.J. Meskers, René A.J. Janssen, *Chem. Phys. Lett.*, **2007**, 437, 193.

2.1 Introduction

π -conjugated polymers have attracted considerable interest in the last decade because of their interesting electro-optical properties. Members of this class of materials are for instance applied as active material in light-emitting diodes and photovoltaics. In these applications the probability of photon emission and absorption is important. It has been recognized that the absorption and emission characteristics of these materials are influenced not only by the local chemical structure but also by the organization of the polymer on the mesoscopic length scale.¹⁻⁵ These structure-property relation(s) have also been investigated using molecular chirality as a label, monitoring the optical properties with circular polarized light.⁶ Incorporation of functional groups on the polymer carrying enantiopure stereocenters makes the polymer chiral and introduces a difference in the absorption of left and right circular polarized light (circular dichroism, CD) as well as a difference in the intensity of left and right polarized photoluminescence (circular polarization of luminescence, CPL).

When studying circular selective absorption or emission it is often convenient to express the results in terms of a degree of circular polarization or dissymmetry ratio (g or g_{abs}), as described in Chapter 1. When studying dilute solutions, the g value is an intrinsic property of the chiral molecule and is independent of *e.g.* concentration and optical path length. For emission of light, the g value is defined as:

$$g_{\text{lum}} = \frac{I_{\text{L}} - I_{\text{R}}}{\frac{1}{2}(I_{\text{L}} + I_{\text{R}})} \quad (1)$$

with I_{L} (I_{R}) being the intensity of left (right) polarized photoluminescence light. For the absorptive and emissive transition between the ground state and the lowest excited singlet state one expects $g_{\text{abs}} = g_{\text{lum}}$.

Studies of small (oligomeric) model compounds in solution have shown that the circular polarization may arise from the local chiral arrangement of two or more identical chromophoric groups. Here interchromophoric coupling and delocalization of the optical excitation over more than one chromophore play an important role.⁷⁻¹⁰ In practice, for small molecules with allowed optical transitions, the g -values rarely reach above 10^{-2} .

Studies on films of chiral π -conjugated polymers displaying thermotropic liquid crystalline phases have shown very high g values after thermal annealing and mesophase formation in both absorption and emission (in some cases > 0.1).^{11,12} For chiral poly[9,9-bis((3S)-3,7-dimethyloctyl)-2,7-fluorene] it was shown that the g_{abs} value depends strongly on the thickness of the polymer film and varies over more than three orders of magnitude, reaching values up to 1 for films with a thickness of 400 nm.¹³ The thickness dependence shows that in this case the g values cannot be interpreted as an intrinsic property of the material and this contradicts the interpretation of the circular polarization in terms of a difference in the probability for absorption (emission) of left and right circular polarized photons at the site of

the optical excitation. Instead, the circular polarization seems associated with the long-range order induced by thermal annealing.

In this Chapter we investigate films of a chiral regioregular polythiophene poly[3-((3S)-3,7-dimethyloctyl)thiophene] (PT811, Figure 2, Chapter 1)^{14,15} obtained by spin coating. Circular polarization in absorption and fluorescence of polythiophenes is known,^{16- 22} but a detailed analysis of the origin of the circular polarization in films has not yet been given. Here we study the degree of circular polarization as a function of film thickness for both absorption and fluorescence in order to see whether the interpretation of the circular polarization in terms of a *local* circular differential probability of absorption or emission can be falsified. Regioregular poly(3-alkylthiophenes)²³ are known to form ordered domains and certain polythiophenes even show mesomorphic behavior.²⁴ Therefore, an influence of long-range order on the chiroptical properties as observed for liquid crystals can not be ruled out a priori. As mentioned above a pronounced thickness dependence of the g values, as previously observed for a chiral polyfluorene, would argue against an interpretation in terms of the local electronic structure of the material.

2.2 Experimental section

Polymer PT811 was synthesized as described earlier.¹⁴ Films were prepared by spin coating from chloroform solution on glass substrates. The thickness was varied by changing the spin speed or, alternatively, the concentration of PT811 in the solution used for spin coating. Film thickness was measured using a Tencor P10 surface profilometer.

CD spectra were measured on a Jasco J600 spectropolarimeter. Circularly polarized luminescence spectra were measured on a home-built setup that uses a photoelastic modulator and a multichannel photon-counting detection system.^{22,25} For CPL measurements on films, the excitation light source used was a Hg lamp with a 438 nm interference filter (spectral bandwidth 4 nm). This light was depolarized by passing it through an optical fiber, and it was incident on the film with a direction parallel to the normal of the film.²⁶ The emission was detected in an in-line geometry to avoid artifacts resulting from linear polarization. A cut-off filter ($\lambda > 610$ nm) was placed before the monochromator used for emission wavelength selection. CPL error bars in Figure 2 and 3 represent two standard deviations for each measurement, estimated from repeated sampling of the degree of circular polarization in luminescence g_{lum} .

2.3 Results and discussion

In Figure 1 we show the absorption and circular dichroism spectra of films of PT811 prepared in various ways. The wavelength region studied covers the allowed optical transition from the ground state to the lowest excited singlet state (S_0 - S_1). This transition appears as a broad band with a maximum at around 525 nm. At longer wavelengths, some vibronic fine structure in the spectrum may be discerned, which is usually associated with the presence of

well ordered, aggregated material.^{3,27} In the top part of Figure 1 we illustrate the effect of the spin speed in the spin coating process on the optical properties of the film. As expected, lower spin speeds give thicker films and a higher absorbance. In the lower part of Figure 1, the spectral data for films prepared by spin coating from solutions with different concentration of polymer are shown. Here solutions with higher concentration are more viscous and hence give a thicker film after spin coating. In addition, to the changes in the magnitude of the absorbance, we also observe a small blue shift of the absorption maximum for films prepared at lower spin speeds. The blue shift is also observed for films from solutions with concentration > 6.7 mg/ml in comparison with the film coated from 6.7 mg/ml at 2000 rpm.

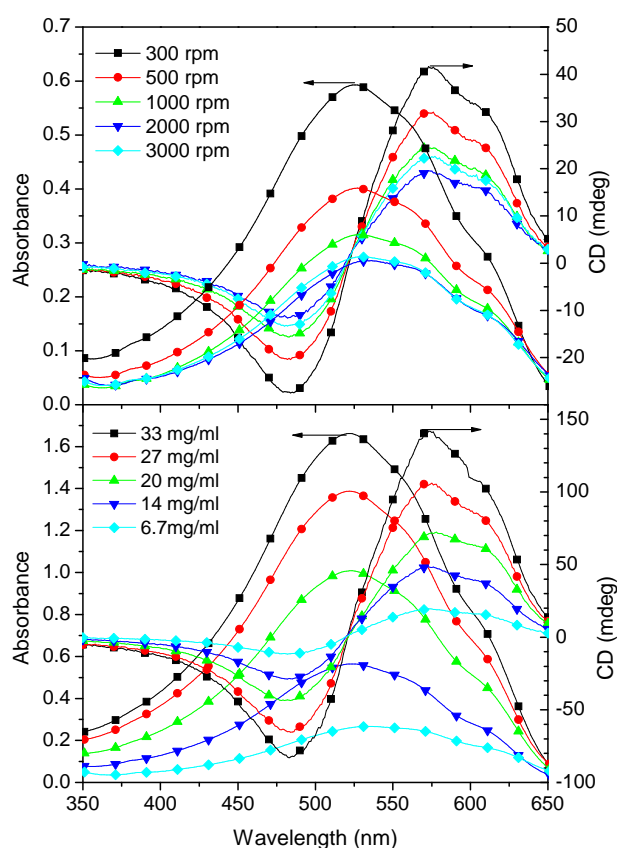


Figure 1: Absorbance and CD spectra of films of PT811 spin coated at different spin speeds from a 6.7 mg/ml CHCl_3 solution (top) and from solutions of different concentrations at 2000 rpm (bottom).

It is known that the absorption spectrum of films of poly(3-hexylthiophene) (P3HT) is sensitive to the preparation conditions of the film and the molecular weight of the polymer.³⁻⁵ For instance, it has been found that P3HT with $M_w \sim 30$ kD gives the most red shifted spectrum and polymers with both higher and lower molecular weight give a slightly blue shifted absorption spectrum. This has been interpreted in terms of the degree of crystallinity and the magnitude of the exciton bandwidth.^{3-5,27} In our case the blue shift observed at slow spin speed and high concentration may be related to a molecular arrangement with a slightly higher degree of disorder.

In Figure 1, also the CD spectra for the films are shown. The band shape of the CD spectrum shows surprisingly little variation with the preparation method; the spectra generally show a bisignate Cotton effect with a positive lobe at long wavelength and a negative lobe at shorter wavelength. The zero crossing in the CD spectrum occurs near the wavelength of maximum absorbance (525 nm). The band shape of the CD spectra is almost *conservative*, meaning that the CD amplitude or ellipticity θ divided by the photon energy integrated over the absorption band sums up to a value close to zero when the ellipticity is plotted on an energy scale:

$$\int_{\text{abs.band}} \theta(\nu) / \nu d\nu \approx 0 \quad (2)$$

These characteristics are consistent with the predictions of the coupled oscillator model for the CD.²⁸

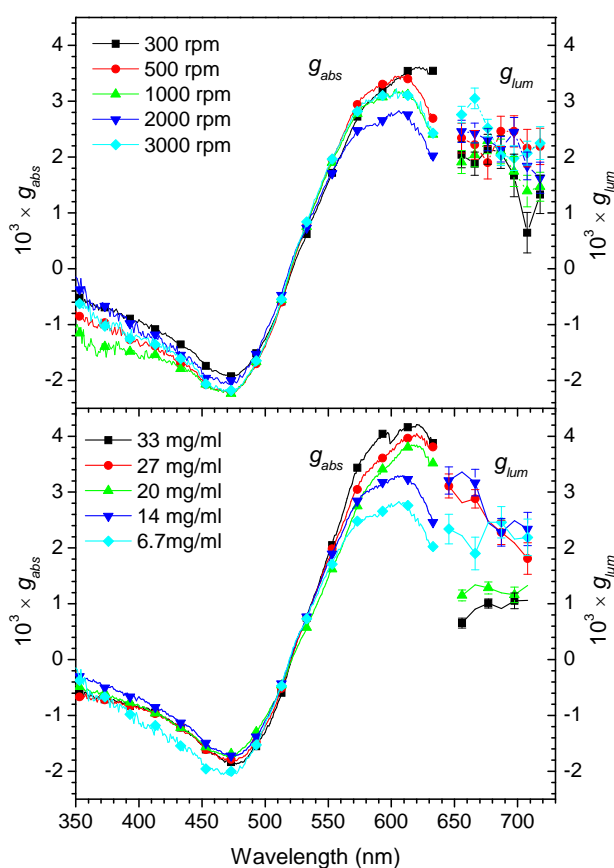


Figure 2: g_{abs} and g_{lum} spectra of films of PT811 spin coated at different spin speed from a 6.7 mg/ml CHCl_3 solution (top) and from solutions of different concentrations at 2000 rpm (bottom).

From the absorption and CD spectra, g_{abs} can be calculated and the results are shown in Figure 2. Also shown in Figure 2 are values for g_{lum} obtained from luminescence measurements. As can be seen the g_{abs} value for the negative Cotton effect near 480 nm is practically independent of film thickness. At the red edge of the absorption band near 600 nm, the observed g_{abs} values vary from +3 to +4 $\times 10^{-3}$ with the thicker films giving a higher

value. The g_{lum} values have the same sign as g_{abs} in the red wing of the absorption band and are similar in magnitude. For the thicker films, the g_{lum} value tends to be lower and a number of explanations can be given for this observation. The first is circular dichroic self-absorption which tends to reduce the g_{lum} . A second factor may be the migration of the optical excitations towards trap sites. These trap sites, which hardly contribute to the light absorption, can act as a luminescent center with polarization properties different from the bulk. Finally it has recently been shown that coupling of the electronic and vibrational motion in exciton coupled systems generally leads to g_{lum} values that change with emission wavelength, being smaller in absolute magnitude for the higher vibronic transitions in emission at longer wavelength.¹⁰ We have studied the wavelength dependence in more detail, investigating a thin film for which the g_{lum} value can be reduced by at most 0.3×10^{-3} through self absorption effects.²² As shown in Figure 3, a wavelength dependent g_{lum} is indeed observed which suggests that the excitonic bandwidth is of the same order of magnitude as the energy associated with the relaxation of the nuclear geometry in the lowest excited singlet state (0.1 eV).^{3,10}

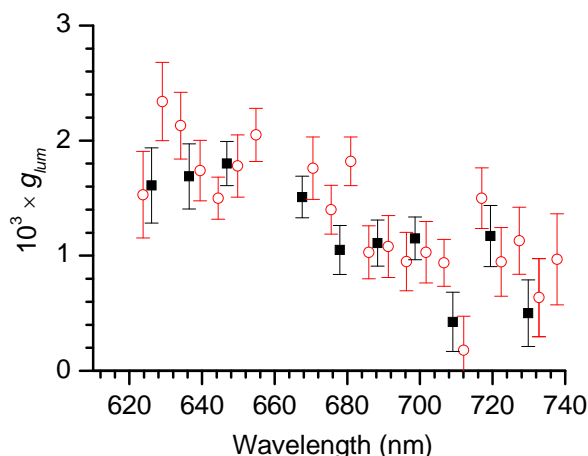


Figure 3: CPL for a spin coated film of PT811 (thickness ~ 70 nm) with excitation light incident on the side of the polymer film facing the glass support (o) and on the air side of the film (■).

The results of the absorption, CD and CPL measurements are summarized in Figure 4. In the upper part the optical density at 525 nm and the magnitude of the CD probed at 484 and 600 nm are plotted as a function of the film thickness. This plot shows an approximately linear relation between absorbance and CD with film thickness. For the thicker films a deviation for the Beer law seems to set in. From the slope of the curve, excluding the thickest film, we find the absorption coefficient $\alpha = 0.5 \times 10^5 \text{ cm}^{-1}$. The lower part of the figure shows the g_{abs} at 484 and 600 nm as well as g_{lum} at 675 nm as a function of film thickness and, as can be seen, the g_{abs} values show a thickness dependence that is very weak in comparison with that of the annealed polyfluorene films.¹³

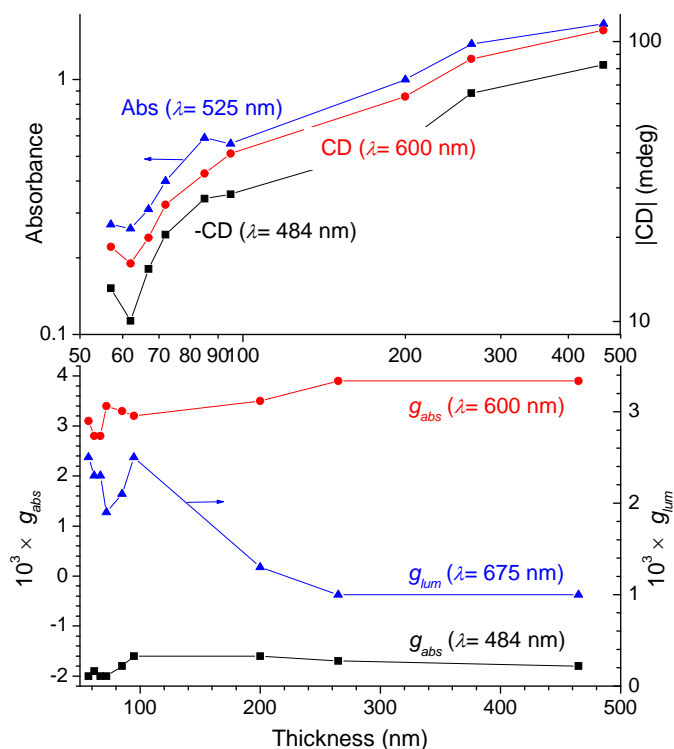


Figure 4: Top: Absorbance and CD as function of film thickness for polymer PT811 in double logarithmic representation. Bottom: degree of circular polarization in absorption (g_{abs}) probed at 484 and 600 nm wavelength and in emission (g_{lum}) probed at 675 nm plotted vs. film thickness.

2.4 Conclusion

Spin coated films of the polythiophene PT811 are characterized by degrees of circular polarization in absorption and luminescence that are nearly independent of the film thickness. This is consistent with the circular polarization arising from a circular differential probability for photon absorption or emission at the site occupied by the optical excitation at the moment of the transition.

References

1. Schwartz, B.J. *Annu. Rev. Phys. Chem.* **2003**, *54*, 141 and references therein.
2. Bunz, U.H.F. *Chem. Rev.* **2000**, *100*, 1605.
3. Chang, J.F.; Clark, J.; Zhao, N.; Sirringhaus, H.; Breiby, D.W.; Andreasen, J.W.; Nielsen, M.M.; Giles, M.; Heeney, M.; McCulloch, I. *Phys. Rev. B* **2006**, *74*, 115318.
4. Kline, R.J.; McGehee, M.D.; Kadnikova, E.N.; Liu, J.; Fréchet, J.M.J.; Toney, M.F.; *Macromolecules* **2005**, *38*, 3312.
5. Zen, A.; Pflaum, J.; Hirschmann, S.; Zhuang, W.; Jaiser, F.; Asawapirom, U.; Rabe, J. P.; Scherf, U.; Neher, D. *Adv. Func. Mater.* **2004**, *14*, 757.
6. Hoeben, F.J.M.; Jonkheijm, P.; Meijer, E.W.; Schenning, A.P.H.J. *Chem. Rev.* **2005**, *105*, 1491.
7. Berova, N.; Nakanishi, K. in: *N. Berova, K. Nakanishi, R.W. Woody (Eds.) Circular Dichroism: Principles and Applications, 2nd ed.*, Wiley-VCH: New York, **2000**.

8. Langeveld-Voss, B.M.W.; Beljonne, D.; Shuai, Z.; Janssen, R.A.J.; Meskers, S.C.J.; Meijer, E.W. Brédas, J.-L. *Adv. Mater.* **1998**, *10*, 1343.
9. Köhler, B.; Enkelmann, V.; Oda, M.; Pieraccini, S.; Spada, G.P.; Scherf, U. *Chem. Eur J.* **2001**, *7*, 3000.
10. Spano, F.C.; Zhao, Z.; Meskers, S.C.J. *J. Chem. Phys.* **2004**, *120*, 10594.
11. Oda, M.; Nothofer, H.-G.; Lieser, G.; Scherf, U.; Meskers, S.C.J.; Neher, D. *Adv. Mater.* **2000**, *12*, 362.
12. Wilson, J.N.; Steffen, W.; McKenzie, T.G.; Lieser, G.; Oda, M.; Neher, D.; Bunz, U.H.F. *J. Am. Chem. Soc.* **2002**, *124*, 6830.
13. Craig, M.R.; Jonkheijm, P.; Meskers, S.C.J.; Schenning, A.P.H.J.; Meijer, E.W. *Adv. Mater.* **2003**, *15*, 1435.
14. Koeckelberghs, G.; Samyn, C.; Miura, A.; De Feyter, S.; De Schryver, F.C.; Sioncke, S.; Verbiest, T.; de Schaezen, G.; Persoons, A. *Adv. Mater.* **2005**, *17*, 708.
15. Verbiest, T.; Sioncke, S.; Koeckelberghs, G.; Samyn, C.; Persoons, A.; Botek, E.; Andre, J.M.; Champagne, B. *Chem. Phys. Lett.* **2005**, *404*, 112.
16. Bouman, M.M.; Havinga, E.E.; Janssen, R.A.J.; Meijer, E.W. *Mol. Cryst. Liq. Cryst.* **1994**, *256*, 439.
17. Bidan, G.; Guillerez, S.; Sorokin, V. *Adv. Mater.* **1996**, *8*, 157.
18. Langeveld-Voss, B.M.W.; Janssen, R.A.J.; Meijer, E.W. *J. Mol. Struct.* **2000**, *521*, 285.
19. Langeveld-Voss, B.M.W.; Janssen, R.A.J.; Christiaans, M.P.T.; Meskers, S.C.J.; Dekkers, H.P.J.M.; Meijer, E.W. *J. Am. Chem. Soc.* **1996**, *118*, 4908.
20. Zhang, Z.; Fujiki, M.; Motonaga, M.; Nakashima, H.; Torimitsu, K.; Tang, H. *Macromolecules* **2000**, *35*, 941.
21. Langeveld-Voss, B.M.W.; Christiaans, M.P.T.; Janssen, R.A.J.; Meijer, E.W. *Macromolecules* **1998**, *31*, 6702.
22. Meskers, S.C.J.; Peeters, E.; Langeveld-Voss, B.M.W.; Janssen, R.A.J. *Adv. Mater.* **2000**, *12*, 589.
23. Sirringhaus, H.; Brown, P.J.; Friend, R.H.; Nielsen, M.M.; Bechgaard, K.; Langeveld-Voss, B.M.W.; Spiering, A.J.H.; Janssen, R.A.J.; Meijer, E.W.; Herwig, P.; de Leeuw, D.M. *Nature* **1999**, *401*, 685.
24. Ong, B.S.; Wu, Y.L.; Liu, P.; Gardner, S. *Adv. Mater.* **2005**, *17*, 1141.
25. Rexwinkel, R.B.; Schakel, P.; Meskers, S.C.J.; Dekkers, H.P.J.M. *Appl. Spectrosc.* **1993**, *47*, 731.
26. Riehl, J.P.; Richardson, F.S. *Chem. Rev.* **1986**, *86*, 1.
27. Spano, F.C. *J. Chem. Phys.* **2005**, *122*, 234701.
28. Harada, N.; Nakanishi, K. *Circular dichroic spectroscopy*, Oxford, **1983**.

Intensive chiroptical properties of *chiral* polyfluorenes associated with fibril formation

Abstract. Thin films of chiral poly[9,9-bis((3*S*)-3,7-dimethyloctyl)-2,7-fluorene] were studied using circular dichroism (CD) spectroscopy. Films spin coated from chloroform solution, show CD with a degree of polarization g_{abs} ($= + 4 \times 10^{-4}$ at 400 nm) that is independent of film thickness (50-290 nm). This implies that g_{abs} is an intensive (*i.e.* a size-independent or bulk) property of the material and related to the chiral organization of the molecules on a length scale less than 50 nm. Atomic force microscopy (AFM) on the films reveals fibrils. Addition of methanol as a non-solvent to a solution of PF811 in chloroform leads to fibril formation in solution and results in CD similar in band shape to that of the pristine spin coated films from chloroform solution and a g_{abs} comparable in magnitude. Thus the chiral molecular arrangement leading to circular dichroism is part of the internal structure of these fibrils.

3.1 Introduction

The optical and electronic properties of thin films of π -conjugated polymers depend on the polymer organization within the film.¹ The performance of polymer light-emitting diodes, field-effect transistors or polymer photovoltaic cells is intimately related to the aggregation state of the polymer chains.

Polyfluorenes (PF) are a class of π -conjugated polymers that has been studied intensively because of their excellent blue light emitting properties.² Polyfluorenes are interesting because they can occur in different liquid crystalline (LC) and (semi-)crystalline states, each with its own optoelectronic properties. Processing conditions have a strong influence on which of the conformational and crystallization states predominates in thin film deposited via e.g. spincoating. This makes PF very attractive for investigations on the relation between organization and optoelectronic properties.³

Circular dichroism (CD) spectroscopy⁴ has been used to study the molecular organization of chiral π -conjugated polymers,⁵ including polyfluorenes. Here, chirality serves as a spectroscopic ‘label’. The magnitude and sign of the CD has been shown to be very sensitive to interchain electronic interactions,⁶ but also to long range helical ordering occurring in e.g. cholesteric phases.

Solid films of chiral polythiophenes often show CD effects as demonstrated Chapter 2. It was shown that the magnitude of g_{abs} is independent of the thickness of the film. This observation indicates that g_{abs} is an *intensive* (i.e. size-independent or bulk) property of these films and that the difference in absorption of the two circular polarizations solely arises from the local molecular arrangement at the site of photon absorption. In other words g_{abs} is the bulk property *intrinsic* to the site where the excited state is created.

In contrast, for thermally annealed films of chiral poly[9,9-bis((3*S*)-3,7-dimethyloctyl)-2,7-fluorene] PF811 (Figure 2, Chapter 1), it has been shown that g_{abs} varies strongly with the thickness of the film.⁷ In this case g_{abs} is an *extensive* (i.e. depending on size) property and the origin of the chiroptical effect is *extrinsic* to the site of photon absorption.⁸ For annealed films of sufficient thickness, g_{abs} can reach very high values (~ 1). The extraordinary magnitude of these CD effects after annealing has been interpreted in terms of long range order in the film induced by thermal annealing in the liquid crystalline state.^{7,9} For thermally annealed films of oligofluorenes also very large CD effects have been observed.⁹ These CD effects were explained quantitatively, originating from chiral nematic ordering of the oligofluorenes in the film.

The extensive circular dichroism can be explained qualitatively by a change in polarization of the light before absorption. Linear birefringence in a film induces a linear polarization component when light travels through it. The direction of the induced linear polarization for left incident light will be at a 90° degree angle to the direction of linear polarization for right incident light. In films with long range order, this induced linear polarization can lead to selective absorption because the oriented molecules in the film will selectively absorb the linear polarized light. As the two circular polarizations give rise to two perpendicular linear

polarizations, one of the circular incident polarizations will be more strongly attenuated than the other. The degree of linear polarization induced before photon absorption controls the magnitude of the selective absorption and is of course dependent on the thickness of the film.

The occurrence of extensive CD effects for *e.g.* polyfluorenes, does not necessarily exclude a contribution to the CD of intensive nature. However, given the very high g_{abs} values arising from extensive effects and the small magnitude of g_{abs} that is typical for genuine intensive effects, an intensive effect can easily be overshadowed by an extensive effect. For films of chiral polyfluorene, intensive CD effects are not known. However, the existence of CD effects in dilute solution¹⁰ indicates that such intensive CD is likely to exist.

In this chapter, we describe intensive CD in films of chiral PF811 spin coated from chloroform solution based on systematic variation of the film thickness. Atomic force microscopy (AFM) on these films shows the presence of fibrillar aggregates. Solvent induced aggregation studies indicate that the intensive CD mainly results from interchain interactions between chains held in a chiral arrangement within the aggregate.

3.2 Experimental

3.2.1 Material, film preparation and instrumentation

Poly[9,9-bis((3*S*)-3,7-dimethyloctyl)-2,7-fluorene] (PF811) with amino end-groups having $M_n = 20,400$ g/mol and $M_w = 37,600$ g/mol (PDI 1.84) was synthesized by Suzuki polycondensation to the procedure reported in literature¹¹ with a small percentage (1%) of *p*-bromonitrobenzene as the end capper to control the molecular weight. Subsequent reduction by SnCl₂ in EtOH/EtOAc led reduction of the nitro- to amino- end groups. Subsequent reduction by SnCl₂ in EtOH/EtOAc led reduction of the nitro- to amino- end groups.

Films of PF811 were prepared by spin coating. The film thickness was varied by changing the concentration of the solution and/or the spin speed (in the range 500 to 4000 rpm). For films prepared from a chloroform solution, the concentration ranged between 10 to 15 mg/ml. Films with different thickness from a chloroform/methanol solvent mixture, were prepared by changing spin speed and keeping the polymer concentration constant (10 mg/ml). Thickness of the films was measured by a Veeco surface profilometer. Thermal annealing of the films was done in air at 120 °C for 10 min. For CD experiments in solution, a stock solution was prepared in chloroform (7.6×10^{-3} mg/ml). Aliquots volume of this stock solution was taken and methanol was added dropwise until reaching the desired solvent composition (in volume ratio, *v:v*). For dynamic and static light scattering, the same stock solution was used.

UV-VIS measurements were performed on a Perkin Elmer Lambda 900 UV/VIS/NIR spectrometer. CD spectra were measured on a Jasco J-815 spectropolarimeter where the sensitivity, and scan rate were chosen appropriately. Temperature dependent measurements were performed with a PFD-425S/15 Peltier-type temperature controller with a temperature range of 263-383 K and adjustable temperature gradient. CD effects in films with ellipticity > 2000 mdeg, were measured using a Perkin Elmer Lambda 900 UV/VIS/NIR spectrometer and a circular sheet polarizer (Oriol).

A Veeco MultiMode connected to a Nanoscope IV control unit was used for AFM. The scanning was done in tapping mode in air. The tips used were PPP-NCH-50 from Nanosensors, and were typically, operated at an amplitude setpoint of 1.5 V (free oscillation amplitude was 2.0 V) in order to obtain better phase images.

3.2.2 Static (SLS) and dynamic light scattering (DLS) set up

For static (SLS) and dynamic light scattering (DLS) experiments, the light output of an intensity-stabilized helium-neon laser (Spectra Physics, $\lambda = 632.8$ nm, 4.5 mW) was focused in the center of a cylindrical glass cell (Helma). The scattered light was transferred to a single photon detector (ALV/SO-SIPD) through a single mode fiber to meet the spatial coherence conditions. SLS measurements were performed with a computerized homemade goniometer, using a step size of 1 degree in the angular range of 30 to 100 degrees, corresponding to the scattering wavevector (q) of 6 to 20 μm^{-1} .

$$q = \frac{4\pi n}{\lambda} \sin(\theta/2) \quad (1)$$

where n is the refractive index of dispersant and θ the scattering angle. The integration time per angle was 5 s. The intensity signal was processed with a 320-channel Multiple Tau Digital Correlator (ALV-5000/E) using a typical acquisition time of 300 s. A temperature controller was used to stabilize the temperature at 293.0 ± 0.1 K. Evaluation of the autocorrelation function gave the value of the decay constant $\Gamma = Dq^2$, where D is the translational diffusion coefficient.

3.3 Results and discussion

3.3.1 CD of unannealed and annealed films of chiral polyfluorene at different film thicknesses

Solid films of PF811 spincoated from chloroform solution show CD. This is illustrated in Figure 1a for a film of 2.3×10^2 nm thickness. The onset of the CD band at 415 nm wavelength coincides with the onset of the first absorption band of PF811 assigned to the allowed $S_0 \rightarrow S_1$ optical transition. The band shape of the CD spectrum is bisignate with a positive maximum at a wavelength $\lambda = 400$ nm and a negative minimum at $\lambda = 360$ nm. From the CD and the absorption spectrum, g_{abs} can be calculated. g_{abs} reaches a maximum at 400 nm ($+4 \times 10^{-4}$) and a minimum at 360 nm (-2×10^{-4}). In Figure 1b we have plotted these g_{abs} values for unannealed films as a function of the thickness of the films.

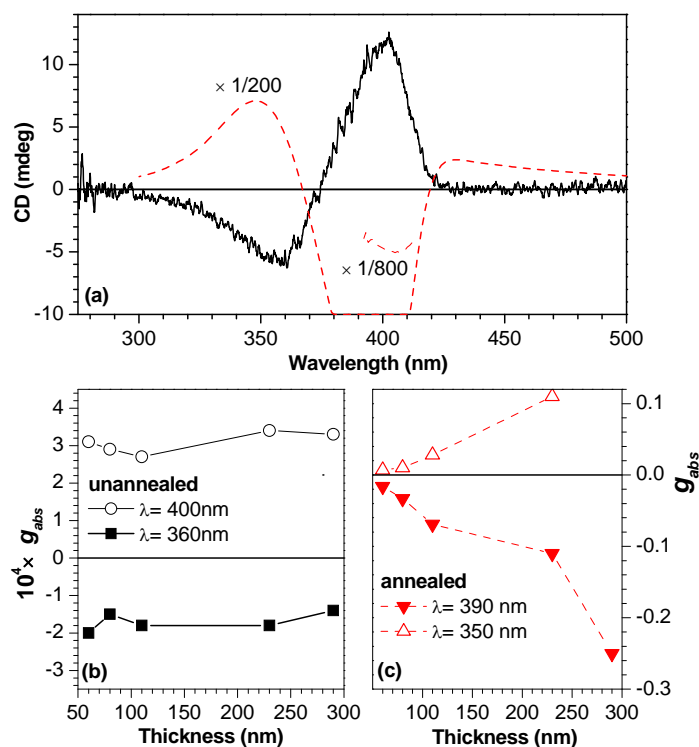


Figure 1. (a) CD spectra of film (thickness 2.3×10^2 nm) of PF811 spincoated from chloroform solution (conc. 10 mg/ml) before (solid line) and after annealing (dashed line). (b) degree of circular polarization in absorbance g_{abs} as a function of film thickness for unannealed films of PF811 spincoated from chloroform probed at 360 and 400 nm (peaks of maximum intensity CD), (c) same as b probed at 350 and 390 nm, but now after annealing at 120 °C for 10 min.

In agreement with earlier reports, we find that upon annealing of the films at 120 °C, the band shape of the CD spectrum changes and the g_{abs} values become much larger.^{4,9} For the annealed films the g_{abs} value strongly depends on film thickness (Figure 1c) and reaches a value -0.25 at 390 nm for the 2.9×10^2 nm thick film. This strong variation of g_{abs} with films thickness for the annealed films shows that in this case g_{abs} is *not* an intensive property of the material.

For the unannealed films with thickness ranging from 50 to 290 nm, we find that g_{abs} is essentially constant. Therefore we can consider g_{abs} to be an intensive property of the material, originating from a chiral molecular organization on a length scale < 50 nm. Curiously (as we shall see in section 3.3.4), a solution of PF811 in chloroform does not show any CD (Figure 3a). This suggests that the chiral molecular organization responsible for the CD effect involves intermolecular interactions.

3.3.2 Analysis of the band shape of the intensive CD spectra

The aggregation studies indicate that interchain interactions are important in the induction of the CD signal. Electronic interchain interactions can give rise to CD effects via so called exciton coupling, where two or more chains held in a chiral arrangement with respect to one

another are treated as a system of coupled oscillators. This coupled oscillator model generally leads to conservative band shapes in the CD spectra. Here *conservative* is expressed as the integral of the CD spectrum over the whole absorption band on an energy scale (eq. (2)) having a value close to zero.

$$\int_{\text{abs band}} \frac{\theta(\nu)}{\nu} d\nu \quad (2)$$

Thus the coupled oscillator model generally predicts CD band shapes which show at least one zero crossing. Below in Table 1 we analyze the intensive CD of PF811, which would determine to which degree it can be considered as conservative. The table below mentions the total area along with area of sub-sections of CD spectra (region of spectra with positive CD denoted as +ve lobe and likewise for negative region of CD as -ve lobe). For unannealed film, the total area is close to zero which supports the idea of CD in an unannealed film arising due to exciton coupling. However for an annealed film the total area is non-zero.

Films spincoated from solvent(s)	Area swept by the CD curve (Eq. 2)						
	Solution	Unannealed film			Annealed film		
Chloroform	No CD	0.25			approx. -75.4		
		- ve lobe	+ ve lobe	- ve lobe	- ve lobe	+ ve lobe	- ve lobe
		0.05	0.8	-0.6	98.3	-332.7	157.2

Table 1. Area swept by solution of PF811 in chloroform unannealed and annealed films spincoated from the same. The area is calculated using equation 2.

3.3.3 AFM on unannealed and annealed films of chiral polyfluorene

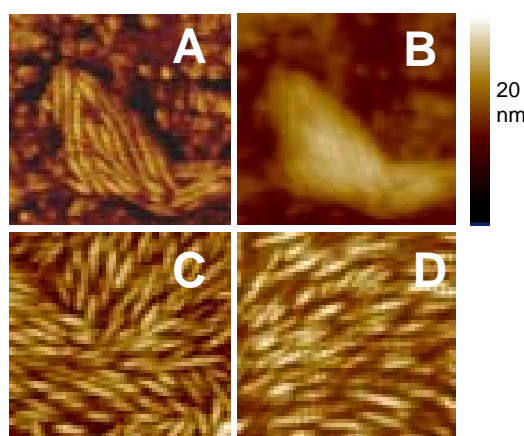


Figure 2. (A) AFM phase image of unannealed film spincoated from very dilute solution of PF811 in chloroform, and B) corresponding AFM height image (height scale 20 nm, film thickness ≤ 15 nm) of the same. (C+D) AFM phase image of unannealed (C) and annealed (D) film spincoated from very dilute solution of PF811 in $\text{CHCl}_3/\text{MeOH}$ (5:3 v/v). All images are $200 \text{ nm} \times 200 \text{ nm}$.

In order to investigate the molecular organization effect further, we have performed atomic force microscopy (AFM) on thin films of PF811 before annealing. In the height image of very thin discontinuous films (Figure 2) fibrillar, worm-like structures can be observed with a height of ~ 10 nm, a width of 10 nm and a contour length of ~ 80 nm. These fibrillar structures can also be observed in the corresponding phase image. We ascribe these fibrillar structures to aggregates of polymers chains formed during the evaporation of the solvent.

3.3.4 Aggregation of chiral polyfluorene in mixture of solvents

Addition of a non-solvent (methanol) to a solution of PF811 in the chloroform also induces a CD effect (Figure 3). Stepwise addition of methanol to the chloroform solution shows an onset of CD at a volume ratio of 5:3 (v/v $\text{CHCl}_3/\text{MeOH}$). Light scattering measurements on solutions of PF811 in $\text{CHCl}_3/\text{MeOH}$ 3:2 v/v show the formation of aggregates of polymer chains (Figure 4). Figure 4a shows that with increasing percentage of methanol, the intensity of scattered light increases. This suggests that upon raising the methanol content of the solution, more polymer chains form aggregates with a particle size of several hundred nm. This conclusion is supported by dynamic light scattering measurements as shown in Figure 4b. We notice that the diffusion decay rate decreases with increasing methanol concentration indicating a larger particle size. We conclude that the CD effect seen at volume ratio of 5:3 v/v ($\text{CHCl}_3/\text{MeOH}$) is the result of aggregation of polymer chains.

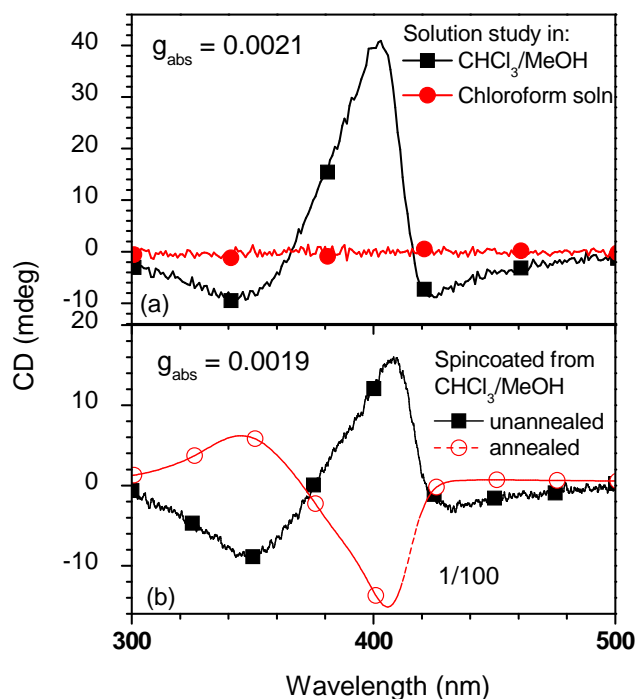


Figure 3. (a) CD spectra of PF811 in dilute chloroform solution (7.6×10^{-3} mg/ml) and $\text{CHCl}_3/\text{MeOH}$ 5:3 v/v solution (4.8×10^{-3} mg/ml) (b) CD spectra of pristine and annealed films (film thickness 3×10^2 nm approximately) of PF811 spincoated from $\text{CHCl}_3/\text{MeOH}$ 5:3 v/v (37.5% MeOH).

The aggregates formed in $\text{CHCl}_3/\text{MeOH}$ solvent mixtures (5:3 v/v) can be transferred from solution to film by spin coating the solvent mixture. The shape of the CD spectra and the magnitude of the associated g_{abs} values measured on the solution of PF811 in $\text{CHCl}_3/\text{MeOH}$ (5:3 v/v) and the films of PF811 spincoated from this solution are virtually the same (Figure 3b). Thus we conclude that the CD effect shown by the films spin coated from $\text{CHCl}_3/\text{MeOH}$ (5:3 v/v) arises from intermolecular interaction within the aggregate. The unannealed films deposited from pure CHCl_3 solution show a CD band shape (Figure 1) that strongly resembles that of the films from $\text{CHCl}_3/\text{MeOH}$ solvent mixture (Figure 3b). In addition both types of films show similar fibrillar features (Figure 2). This indicates that the intensive CD effect in the films from CHCl_3 has its origin in the chiral arrangement of polymer chains in the fibrillar aggregate structures. The magnitude of g_{abs} for the films from chloroform is however significantly lower than for $\text{CHCl}_3/\text{MeOH}$ (5:3 v/v). This may indicate a significant fraction of the chains is still in a random organization.

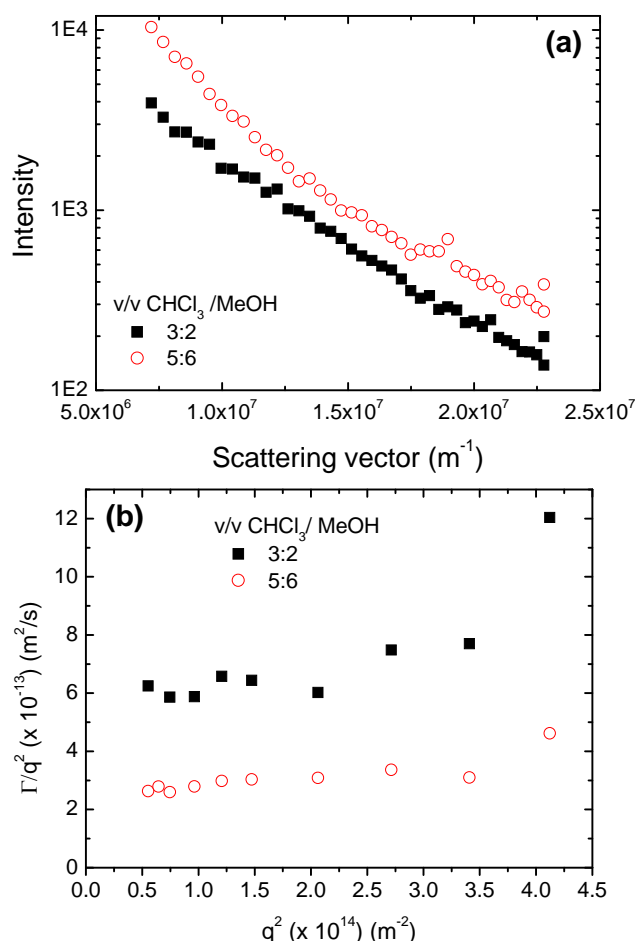


Figure 4. (a) Static, and (b) dynamic light scattering spectra for solution of PF811 in mixture of solvents (chloroform and methanol) in different ratio. Methanol was added drop wise to a freshly prepared solution of PF811 in chloroform (chloroform solution 7.6×10^{-3} mg/ml before addition of methanol).

AFM (Figure 2) indicates that the fibrillar structures observed in the films from $\text{CHCl}_3/\text{MeOH}$ remain intact upon thermal annealing. At the same time, the band shape and

magnitude of the CD for these films changes in a very similar way as observed from the films from CHCl₃. Additionally, the fibrillar structures also remain intact upon annealing thin films spincoated from CHCl₃. It seems possible that the extensive chiroptical effect in annealed films could arise from a cholesteric-like arrangement of the *fibrillar aggregates* in the annealed films. The contribution from the extensive component to the total CD varies strongly with film thickness and should vanish in the limit of very thin film. Incidentally, earlier studies done by Craig⁷ on very thin annealed films of PF811 showed a CD spectrum with the same sign as the intensive effect reported here.⁷ This can now be interpreted as the intensive contribution to the CD. The intensive chiroptical properties of the unannealed films can originate from either intramolecular chirality (e.g. a helical backbone conformation) or from an intermolecular chiral organization of chains in the fibrils (eg. via exciton coupling). The latter explanation is consistent with the CD effects arising upon aggregation of polymer chains within the thin film, distinguished by bisignate CD spectra.

3.4 Conclusion

Pristine films of chiral polyfluorene, spincoated from good solvent without any thermal treatment show intensive chiroptical properties. This indicates a local chiral molecular organization at the site of photon absorption. On annealing the films, extensive chiroptical properties are observed, originating from mesoscopic ordering in the film.

References

1. (a) McCulloch, I.; Heeney, M.; Bailey, C.; Genevicius, K.; Macdonald, I.; Shkunov, M.; Sparrowe, D.; Tierney, S.; Wagner, R.; Zhang, W.M.; Chabynyc, M.L.; Kline, R.J.; McGehee, M.D.; Toney, M.F. *Nat. Mater.* **2006**, *5*, 328. (b) Schwartz, B.J. *Ann. Rev. Phys. Chem.* **2003**, *54*, 141. (c) Hoeben, F.J.M.; Jonkheijm, P.; Meijer, E.W.; Schenning, A.P.H.J. *Chem. Rev.* **2005**, *105*, 1491.
2. Scherf, U.; Neher, D. *Adv. Polym. Sci.*, **2008**, 212.
3. (a) Grimsdale, A.C.; Müllen, K. *Adv. Polym. Sci.* **2006**, *199*, 1. (b) Scherf, U.; List, E. *Adv. Mater.* **2002**, *14*, 477. (c) Neher, D. *Macromol. Rapid. Commun.* **2001**, *22*, 1365.
4. (a) Oda, M.; Meskers, S.C.J.; Nothofer, H.G.; Scherf, U.; Neher, D. *Synth. Met.* **2000**, *111*, 575. (b) Oda, M.; Nothofer, H.-G.; Scherf, U.; Sunjic, V.; Richter, D.; Regenstein, W.; Neher, D. *Macromolecules* **2002**, *35*, 6792. (c) Oda, M.; Nothofer, H.-G.; Lieser, G.; Scherf, U.; Meskers, S.C.J.; Neher, D. *Adv. Mater.* **2000**, *12*, 362.
5. (a) Goto, H.; Okamoto, Y.; Yashima, E. *Macromolecules* **2002**, *35*, 4590. (b) Langeveld-Voss, B.M.W.; Janssen, R.A.J.; Meijer, E.W. *J. Mol. Struct.* **2000**, *521*, 285. (c) Bidan, G.; Guillerez, S.; Sorokin, V. *Adv. Mater.* **1996**, *8*, 157. (d) Bouman, M.M.; Havinga, E.E.; Janssen, R.A.J.; Meijer, E.W. *Mol. Cryst. Liq. Cryst.* **1994**, *256*, 439.
6. (a) Berova, N.; Gargiulo, D.; Derguini, F.; Nakanishi, K.; Harada, N. *J. Am. Chem. Soc.* **1993**, *115*, 4769. (b) Langeveld-Voss, B.M.W.; Beljonne, D.; Shuai, Z.; Janssen, R.A.J.; Meskers, S.C.J.; Meijer, E.W.; Brédas, J.L. *Adv. Mater.* **1998**, *10*, 1343.
7. Craig, M.R.; Jonkheijm, P.; Meskers, S.C.J.; Schenning, A.P.H.J.; Meijer, E.W. *Adv. Mater.* **2003**, *15*, 1435.
8. Saeva, F.D.; Olin, G.R. *J. Am. Chem. Soc.* **1976**, *98*, 2709.

9. (a) Geng, Y.H.; Trajkovska, A.; Katsis, D.; Ou, J.J.; Culligan, S.W.; Chen, S.H. *J. Am. Chem. Soc.* **2002**, *124*, 8337. (b) Geng, Y.H.; Trajkovska, A.; Culligan, S.W.; Ou, J.J.; Chen, H.M.P.; Katsis, D.; Chen, S.H. *J. Am. Chem. Soc.* **2003**, *125*, 14032.
10. (a) Tang H.-Z.; Fujiki, M.; Sato, T. *Macromolecules* **2002**, *35*, 6439; (b) Vanormelingen, W.; Van den Bergh, K.; Verbiest, T.; Koeckelberghs, G. *Macromolecules* **2008**, *41*, 5582.
11. Abbel, R.; Schenning, A.P.H.J.; Meijer, E.W. *Macromolecules* **2008**, *41*, 7497.

Circular differential scattering of light in films of *chiral* polyfluorene*

Abstract. Circular differential transmission in thick films (1.1 μm) of poly[9,9-bis((3*S*)-3,7-dimethyloctyl)-2,7-fluorene] is investigated. The vitrified liquid crystalline film obtained after annealing shows high circular differential transmission of light in the wavelength range where the polyfluorene does not absorb ($\lambda > 450$ nm). Using a specifically designed chiroptical setup, we show that circular selective reflection of light in which the circular polarization of the light is retained after reflection, a process which is characteristic for cholesteric liquid crystalline films, makes a negligible contribution to the differential transmission. Using an integrating sphere, it is shown that circular differential scattering can account for the observed circular differential transmission for $\lambda > 450$ nm.

* Girish Lakhwani, Stefan C.J. Meskers, René A.J. Janssen, *J. Phys. Chem. B*, **2007**, *111*, 5124.

4.1 Introduction

Polyfluorenes¹⁻⁴ (PF) are π -conjugated polymers, displaying fascinating properties. They have been studied intensively in the last decade as active material in blue polymer light-emitting diodes (LEDs). Copolymers of fluorene with other monomers can produce emission colors throughout the visible spectrum and can also be applied in polymer photovoltaic devices.⁵⁻⁸ Structure-property relations have been investigated for PF derivatives with a variety of side groups at the 9 position of the fluorene. When introducing alkyl substituents, the polymers generally show both thermotropic and lyotropic liquid crystalline phases and it has been shown that the opto-electronic properties of the polyfluorenes can be influenced by the structure and morphology of the polymer film.^{9,10}

One of the most widely studied PF derivatives is poly(9,9-di-*n*-octyl-2,7-fluorene)^{11,12} (PFO). This polymer melts at a temperature of 300 °C and displays a nematic liquid crystalline state in the temperature range 160–300 °C. Below 160 °C the polymer is crystalline. Also a mesomorphic, metastable β -phase has been identified,¹³⁻¹⁵ which forms upon solvent treatment. Poly(9,9-di-*n*-hexyl-2,7-fluorene)^{16,17} displays a phase behavior very similar to PFO, showing a nematic phase above 250 °C. Diffraction studies in combination with molecular modeling have shown that the fluorene units in PFO chains, are not coplanar but twisted with a dihedral angle between two adjacent monomers of 156–165°.¹² *Racemic* poly[9,9-di-(2-ethylhexyl)-2,7-fluorene] (PF2/6) also shows a crystalline-to-liquid-crystalline phase transition at about 160 °C. By rapid cooling from the nematic state, a vitrified molecular arrangement can be obtained and diffraction studies have shown that chains are ordered in a hexagonal lattice. Interestingly, the chains adopt a 5_2 (or possibly 5_1) helical conformation^{4,18} In the perfect 5_2 helix, the adjacent monomer units make a 144° dihedral angle. Diffraction studies on oligomeric model compounds, which adopt smectic LC phases, have confirmed the 144° torsion angle between the monomer units.¹⁹ In addition, molecular modeling has shown that the planar conformation is unfavorable.²⁰ By depositing the polymers on an alignment layer and heating the material above the Cr-N transition temperature, it has been shown for PFO and PF2/6, that the polymer chains can be oriented. In this way, the opto-electronic properties of the polymer can be influenced and a light-emitting diodes generating highly linear polarized light can be constructed.^{11,21,22}

Apart from achiral or racemic PF derivatives, *chiral* polyfluorenes have also been investigated.²³⁻²⁶ These materials also show a LC phase, and it was shown that highly circular polarized electroluminescence could be obtained from these chiral polymers after thermal annealing of the active layer above the LC transition.²⁷ The chiroptical properties of films of annealed poly[9,9-bis((3*S*)-3,7-dimethyloctyl)-2,7-fluorene] (PF811) were studied as a function of film thickness and it was found that the degree of circular polarization in absorption is strongly dependent on thickness.²⁸ This indicates that the circular polarization does not arise solely from the local molecular arrangement at the site of photon absorption, but is also influenced by the mesoscale properties of the film. Unfortunately, the structural arrangement of the chains in the chiral PF derivatives has not been investigated by *e.g.*

diffraction studies and the expected helical conformation is not supported by direct experimental evidence.

A relation between the circular polarization in absorption and emission and the mesoscopic organization of films of chiral fluorene *oligomers* was established by Chen and coworkers.^{29,30} These molecules adopt a chiral nematic ordering in the film when heated above the Cr-LC phase transition temperature. After rapid cooling, a vitrified molecular arrangement is obtained, which shows pronounced chiroptical properties. For thick films, a selective reflection band, characteristic of cholesteric ordering could in some cases be observed. The optical properties of thin films for wavelengths resonant with the absorption band could be modeled taking into account the cholesteric arrangement of the molecules in combination with the linear dichroism and linear birefringence of the molecular layers within the film.³⁰ In this approach, the polarization of photons changes from purely circular to (partially) linear as the photon moves through the material, with the two incident circular polarizations giving rise to perpendicular linearly polarized components. Linear dichroism of the molecules at the site of absorption or emission is then ultimately responsible for the dichroism observed for the film as a whole. The findings for the chiral oligofluorenes has prompted the question whether also for chiral polyfluorene polymers, the chiroptical properties originate from a cholesteric organization of the polymers chains on a mesoscopic length scale.

In this study we investigate circular differential transmission of light through thermally annealed films of the chiral PF derivative PF811. We focus on the wavelength region 450–630 nm for which the photon energy is too low to excite the polymer via the lowest allowed singlet-singlet transition. For this wavelength region differential transmission of light could, in principle, arise from circular selective scattering or reflection. The occurrence of the latter process can give evidence for the presence of cholesteric ordering, because it is well known that cholesteric phases selectively reflect one circular polarization of incident light.³¹ This reflection process distinguishes itself from reflection at a dielectric boundary by the polarization of the reflected light; upon reflection by a cholesteric LC, the circular polarization of the reflected light is retained, while reflection at the interface between two dielectrics leads to a reversal of the circular polarization. This feature allows one to probe circular selective reflection by cholesteric LCs in a specific way and in this study we describe a simple chiroptical setup by which this polarization-conserving, circular selective reflection can be detected.

Apart from selective reflection, also circular differential scattering may contribute to the circular differential transmission.³² The scattering contribution has been evaluated for large conglomerates of nucleic acids,^{33,34} and also cholesteric liquid crystals have been investigated. For the latter class of materials, the finite range in the correlation of molecular orientation and position results in circular differential scattering of light in all directions.³⁵

Here we describe a specifically designed chiroptical setup for the study of circular differentials in transmission, scattering, and reflection. With regard to the circular polarized reflection measurements, the setup can measure selectivity down to 10^{-3} level and can

distinguish between reflection in which the circular polarization is conserved and the one in which it is reversed. The latter type of reflection is expected at the boundary of two dielectric media and is usually considered to be independent of the medium chirality for light incident along the interface normal.³⁶ For specular reflection, circular selectivity has been reported.³⁷

While selective reflection of light by films of oligofluorenes has been demonstrated, we find here that for films of PF811, circular selective reflection is below our current detection limit. In contrast, we find that circular selective scattering of light can account for the observed circular differential transmission in the wavelength range from 450 to 630 nm.

4.2 Experimental section

4.2.1 Materials

PF derivative poly[9,9-bis((3*S*)-3,7-dimethyloctyl)-2,7-fluorene] (PF811, Figure 2, Chapter 1) was synthesized as described earlier.^{24,28} The M_w of the polymer is 10,000 with a PDI of 1.6. The PF films were prepared by doctor blading and 1.1 μm thick films were obtained. These films were further annealed for two hours at 120 °C, which is above the liquid crystalline temperature of polyfluorene polymer.²⁷ This method was preferred over spin coating because it can produce thicker films for which the chances of observing selective reflection are higher. These thick films did not show any significant linear polarized absorption, and no significant depolarization or texture under a polarizing microscope. The optical rotation measured at the Na-D line amounts to -0.22° .

Films with a known cholesteric ordering were prepared in the following way. The mesogens RM257 and RM82 (Merck, Germany) were mixed in ratio of 4:1, and 1% of IRG 184 (Irgacure 184, Ciba Specialty Chemicals, Switzerland) as photocure. 4.4% of the chiral dopant LC756 (Merck, Germany) was added to induce a right handed cholesteric order. The solution (xylene) was spin coated on glass substrates with polyimide alignment layer. The film was then annealed at 80 °C for 5 min., quenched rapidly and photocured in an oxygen free environment under a UV lamp.

CD spectra were measured on a Jasco J600 instrument, specular reflection on a Perkin Elmer Lambda 900 with S0086703 accessory and film thickness on a Tencor P10 surface profiler.

4.2.2 Tailor made circular selective reflection/scattering optical setup optical setup

The setup used is depicted schematically in Figure 1. A laser (HeNe or Ar⁺) is used as a linear polarized source with the polarization in the vertical direction. The beam is incident on a non-polarizing beam splitter (Thorlabs BS016). After deflection, the light is passed through a photoelastic modulator (Morvue) operating at 50 kHz, resulting in time modulated circularly polarized light. During the modulation cycle of 20 μs , the transmitted light is first linearly polarized and then becomes left circularly polarized light when the modulator reaches $\lambda/4$ retardation at 5 μs (Figure 2). Halfway the modulation cycle (10 μs) the transmitted light is

again linearly polarized along the vertical direction and, finally, at $15 \mu\text{s}$ when the retardation reaches $-\lambda/4$, the light is right circularly polarized.

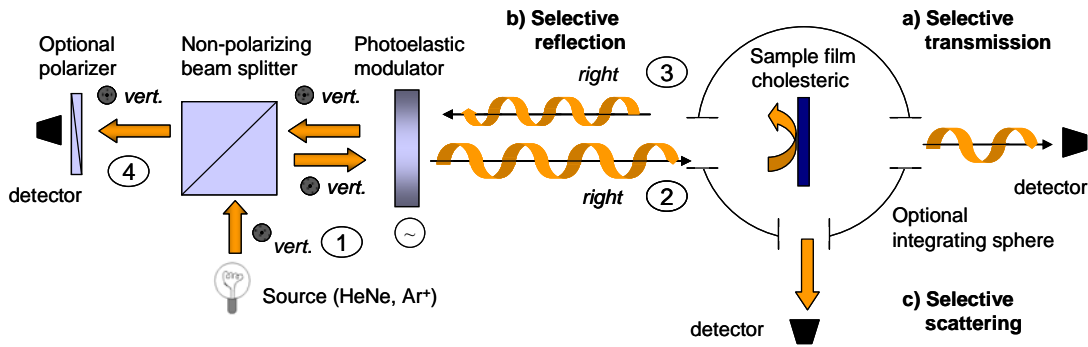


Figure 1: Schematic setup for measurement of (a) circular selective transmission (circular dichroism), (b) circular selective reflection, and (c) circular selective scattering. Here reflection by a right handed cholesteric reflector is illustrated.

The sample film is oriented such that its normal is parallel to the incoming light beam so that part of the incident circularly polarized light is reflected in the opposite direction and passes through the modulator again. If the light changes its circular polarization upon reflection (*e.g.* right \rightarrow left) then upon the second pass through the modulator it will be converted into linearly polarized light with *horizontal* polarization. Contrary, light that retains its circular polarization upon reflection is converted into *vertically* polarized light. By placing a linear polarizer after the beam splitter, in front of the Si photodiode (Thorlabs PDA 520, response up to 300 kHz) the two types of reflected light can be separated and circular selectivity in both reflection modes can be evaluated. The reflected light is recorded using either a digital oscilloscope triggered by the reference signal (Tektronix, TDS 3052) from the modulator or using a lock-in amplifier (Stanford research systems SR830). The polarization of light at different points in the experiment is listed in Table 1 for glass and for a cholesteric liquid crystalline film as reflector (see Section 4.3.2).

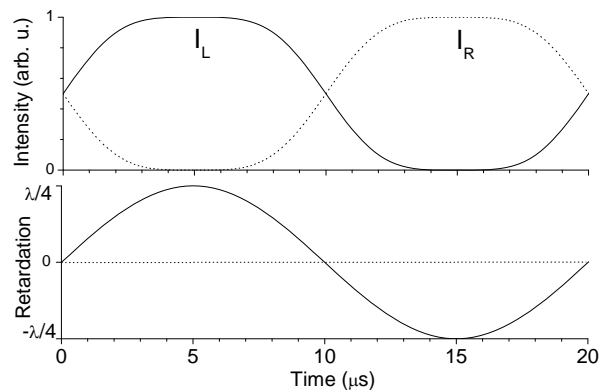


Figure 2: Schematic illustration of the action of the photoelastic modulator. Top: left and right circular intensities for light generated by passing of a linear polarized beam through the modulator rotated by 45 degrees. Bottom: optical retardation for light polarized in the direction of the applied mechanical stress as a function of time.

The setup can be adapted to measure also circular differential transmission by changing the position of the photodiode. In addition, circular differential scattering can be monitored by placing the film in an optional integrating sphere. The sphere has two exit ports. One is perpendicular to the beam direction and is used to measure the scattered light with a photodiode. The second exit is exactly opposite to the entrance port of the sphere, allowing transmitted light to leave the sphere without contributing to the scattered signal. By placing the photodetector at the exit port in the back, one can measure the differential transmission signal under the same conditions as the differential scattering.

4.2.3 Stokes-Müller analysis

In order to develop an accurate description of the reflection experiment mentioned above, the Stokes-Müller formalism has been used to model the optical signal. To consider polarization effects by our setup (Figure 1), we employ the Stokes-Müller formalism; a given polarization state is completely described by its Stokes vector and any optical element (polarizer, modulator, sample, photodiode) is defined by its 4×4 Müller matrix. The transformation of a polarization state is given mathematically by pre-multiplication of the corresponding Stokes vector with the Müller matrix of the optical devices in order of their application in the setup. The Stokes vector for polarized incident light is:

$$S_i = \begin{pmatrix} I_0 \\ I_1 \\ I_2 \\ I_3 \end{pmatrix}$$

where S_i is the Stokes vector for incident light, I_0 is the total intensity, I_1 is intensity of linear polarization of light at 45°, I_2 is intensity of circular polarization of light, and I_3 is intensity of linear polarization of light at 0°.

$$I_{out} = \text{Modulator(in)} \times \text{Sample}_{LC} \times \text{Modulator(out)} \times \text{Pol}_{vertical} \times \text{Photodiode} \times S_i \quad (1)$$

$$I_{out} = \text{Modulator(in)} \times \text{Sample}_{glass} \times \text{Modulator(out)} \times \text{Pol}_{horizontal} \times \text{Photodiode} \times S_i \quad (2)$$

Here S_i is Stokes vector for incident vertically polarized light. The I_{out} is the Stokes vector of output light (position 4 in Figure 1) after passing through all optical elements in-route in the setup. The intensity at the photodetector at position 4 in Figure 1 can now be calculated using the eq. 1 and 2 for cholesteric LC film and glass samples respectively.

$$S_i = \begin{pmatrix} 1 \\ 0 \\ 0 \\ 1 \end{pmatrix}$$

Eq. 1 and eq. 2 contain the Müller matrices for the several optical elements, which are written below.

$$\begin{aligned} \text{Pol}_{\text{vertical}} &= \frac{1}{2} \begin{pmatrix} 1 & 0 & 0 & 1 \\ 0 & 0 & 0 & 0 \\ 0 & 0 & 0 & 0 \\ 1 & 0 & 0 & 1 \end{pmatrix} & \text{Pol}_{\text{horizontal}} &= \frac{1}{2} \begin{pmatrix} 1 & 0 & 0 & -1 \\ 0 & 0 & 0 & 0 \\ 0 & 0 & 0 & 0 \\ -1 & 0 & 0 & 1 \end{pmatrix} \\ \\ \text{Modulator(in)} &= \frac{1}{2} \begin{pmatrix} 1 & 0 & 0 & 0 \\ 0 & 1 & 0 & 0 \\ 0 & 0 & C(\delta, t) & -S(\delta, t) \\ 0 & 0 & S(\delta, t) & C(\delta, t) \end{pmatrix} & \text{Modulator(out)} &= \frac{1}{2} \begin{pmatrix} 1 & 0 & 0 & 0 \\ 0 & 1 & 0 & 0 \\ 0 & 0 & C(\delta, t) & S(\delta, t) \\ 0 & 0 & -S(\delta, t) & C(\delta, t) \end{pmatrix} \\ \\ \text{Photodiode} &= \begin{pmatrix} 1 & 0 & 0 & 0 \\ 0 & 0 & 0 & 0 \\ 0 & 0 & 0 & 0 \\ 0 & 0 & 0 & 0 \end{pmatrix} \end{aligned} \quad (3)$$

where $C(\delta, t)$ and $S(\delta, t)$ are given by $\cos(\delta \sin(2\pi ft))/2$ and $\sin(\delta \sin(2\pi ft))/2$ respectively, and represent the periodic change of retardation in the quartz crystal of the modulator. δ is the amplitude of the modulation, which can be adjusted by controlling the voltage of the circuit that drives the modulator. f denotes the natural frequency of the modulator (50 kHz) and t represents time.

The Müller matrices describing the reflection by the LC film and by glass with refractive index n are given by:

$$\text{Sample}_{\text{LC}} = \frac{1}{2} \begin{pmatrix} 1 & 0 & 1 & 0 \\ 0 & 0 & 0 & 0 \\ 1 & 0 & 1 & 0 \\ 0 & 0 & 0 & 0 \end{pmatrix} \quad \text{Sample}_{\text{glass}} = \left(\frac{1-n}{1+n} \right)^2 \begin{pmatrix} 1 & 0 & 0 & 0 \\ 0 & 1 & 0 & 0 \\ 0 & 0 & -1 & 0 \\ 0 & 0 & 0 & 1 \end{pmatrix} \quad (4)$$

These matrices are derived from the general Müller matrix describing the optical properties of a (optically thin) sample³⁸:

$$\text{Sample} = f \begin{pmatrix} 1 & -LD' & CD & -LD \\ -LD' & 1 & -LB & -CB \\ CD & LB & 1 & -LB' \\ -LD & CB & LB' & 1 \end{pmatrix} \quad (5)$$

where LD is the Linear Dichroism and CB (LB) is the Circular (Linear) Birefringence in the plane of the sample (x - y). LD' and LB' are the terms at 45° to the x axis. Here, f is a factor describing the reflectivity of the sample. In Figure 3 we show reflection measurements on ordinary glass with the solid lines corresponding to the experiment and the dotted lines to the modeling of reflection at an idealized, single dielectric interface. The output of the detector is plotted versus time for three different configurations: a) without linear polarizer in front of the detector b) with a vertical linear polarizer and finally c) with a horizontal linear polarizer. When the polarizer is absent, the modeling predicts constant intensity, which is in good agreement with the experimental trace. With the vertical polarizer present, the intensity is practically zero when circular polarized light is reflected while the intensity peaks when linear polarized light bounces off the glass slide. With the horizontal polarizer in place, the reflected intensity maximizes for circular polarized light which confirms the reversal of the circular polarization upon reflection at the dielectric boundary. Incidentally, the fact that in the absence of a polarizer a constant intensity is measured shows that the combination of the non-polarizing beam splitter and the photodetector is approximately equally sensitive to both linear polarizations.

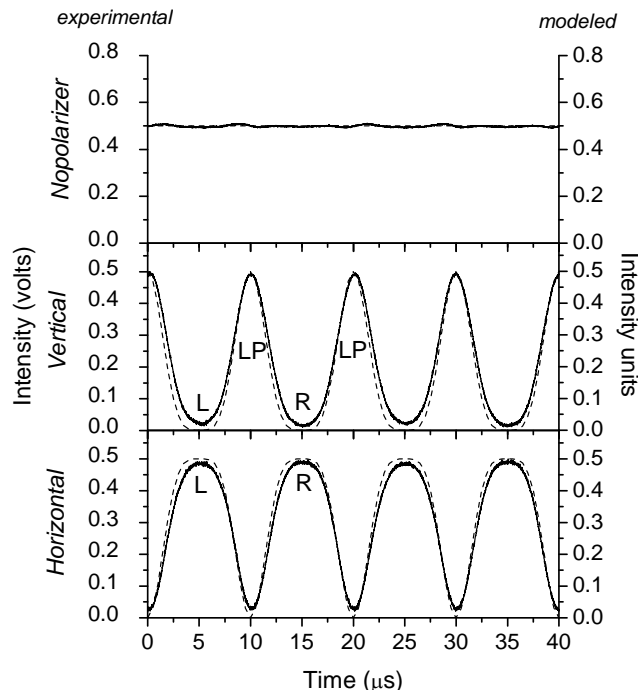


Figure 3: Experimental (solid) and modeled (dashed) intensity-time traces for reflection of light with 632 nm wavelength at normal incidence on glass slide. Top: no polarizer inserted in front of the detector at pos. 4 in Figure 2. Middle: vertical linear polarizer at pos. 4. Bottom: horizontal lin. polarizer. L, R: Left, Right circular polarized light incident on the film. LP: vertical linear polarized light. Dashed lines refer to modeling using the Stokes-Müller calculus.

4.2.4 Dissymmetry ratios

When studying circular selective absorption, transmission or reflection, it is often convenient to express the results in terms of a degree of circular polarization or dissymmetry ratio. For absorption of light the dissymmetry ratio is defined as g_{abs} , as we saw in Chapter 1.

$$g_{abs} = \frac{A_L - A_R}{\frac{1}{2}(A_L + A_R)} \quad (6)$$

For selective reflection, scattering or transmission, dissymmetry ratios may be defined in various ways and here we briefly discuss the particular definitions used in this work. We also address relation between various dissymmetry ratios. First we consider selective scattering. Using an integrating sphere as illustrated in Figure 1, one can record the intensity of scattered light for both left and right circular polarized incident light (I_S^L and I_S^R). The g value for scattering can then be defined as:

$$g_{scat} = \frac{I_S^L - I_S^R}{\frac{1}{2}(I_S^L + I_S^R)} \quad (7)$$

If it is assumed that there is no absorption and because the integrating sphere allows one to collect the light scattered in all directions, the intensity of detected scattered light will be proportional to the difference of the intensities of the incident (I_0) and transmitted (I_T) beam. The averaging of the scattered intensity over all directions is important, because Tinoco et al. have shown that the circular differential scattering varies strongly with the scattering angle and can even change sign.³⁹

$$I_S \propto (I_0 - I_T) \quad (8)$$

If the loss in intensity upon transmission through the film is small, I_T can be expressed in a Taylor series:

$$I_T = I_0(1 - A' \ln 10 + \dots) \quad (9)$$

where A' is the apparent absorbance resulting from the scattering. The relations (6)-(9) then imply:

$$g_{scat} \cong \frac{A'_L - A'_R}{\frac{1}{2}(A'_L + A'_R)} = g_{abs}' \quad (10)$$

We recall that this relation has been derived under the premise that the reduced intensity of the transmitted beam is due to scattering of light only. When recording the intensity of transmitted light upon irradiation with either left or right circular polarized incident light (I_T^L and I_T^R) one can define a g value for transmission:

$$g_{\text{trans}} = \frac{I_T^L - I_T^R}{\frac{1}{2}(I_T^L + I_T^R)} \cong \frac{(A_R - A_L) \ln 10}{(1 - \frac{1}{2}(A_R + A_L) \ln 10)} = \frac{A_R - A_L}{(\log e - \frac{1}{2}(A_L + A_R))} \quad (11)$$

In the reflection measurements we can distinguish between the reflection in polarization of the incoming light is retained (LL,RR) and the reflection in which it is reversed (LR,RL). Accordingly we can define two g -values for reflection:

$$g_{\text{refl}}^{\text{LL,RR}} = \frac{I_{\text{refl}}^{\text{LL}} - I_{\text{refl}}^{\text{RR}}}{\frac{1}{2}(I_{\text{refl}}^{\text{LL}} + I_{\text{refl}}^{\text{RR}})} \quad (12)$$

$$g_{\text{refl}}^{\text{LR,RL}} = \frac{I_{\text{refl}}^{\text{LR}} - I_{\text{refl}}^{\text{RL}}}{\frac{1}{2}(I_{\text{refl}}^{\text{LR}} + I_{\text{refl}}^{\text{RL}})} \quad (13)$$

where cholesteric liquid crystals are characterized by high values for $g_{\text{refl}}^{\text{LL,RR}}$, while $g_{\text{refl}}^{\text{LR,RL}}$ can be expected to be zero for reflection at normal incidence. In the case where the optical loss after transmission of light through a film is small and solely due to selective reflection of light one finds in analogy to eq. 10 that $g_{\text{refl}} = g_{\text{abs}}'$.

4.3 Results and Discussion

4.3.1 Absorption, specular reflection and circular dichroism

Before addressing the circular polarized reflection and scattering measurements we first discuss the optical characterization of the polyfluorene films using conventional methods. In Figure 4, absorption, reflection and circular dichroism (CD) spectra are shown for the doctor bladed film and after thermal annealing. The absorption spectrum shows the well known S_0 - S_1 transition of polyfluorene near 400 nm. After thermal annealing, the maximal absorbance is reduced and saturates at optical density ~ 2 . Optical microscopy shows that this is due to formation of pinholes, a process that could not be avoided when working with these thick films (1.1 μm) prepared by doctor blading. The specular reflection (middle) shows a sigmoidal feature in the wavelength region that coincides with the absorption band which can be attributed to the strong dispersion in the refractive index of the material near the allowed optical transition. Upon annealing, the reflectivity near the onset of the absorption band (~ 430 nm) actually decreases, while the apparent optical density in this wavelength region increases. This indicates that upon annealing, the scattering of light over large angles becomes more

prominent as the setup for measuring specular reflection records only light scattered close to the film normal with a limited acceptance angle. The reflection spectra for both the annealed and as cast film show pronounced oscillations in the higher wavelength region which can be interpreted in terms of interference between the wave reflected from the top air-polymer interface and the wave reflected of the bottom polymer-glass interface. From these reflection spectra there are no indications for the presence of a selective reflection band associated with cholesteric ordering.

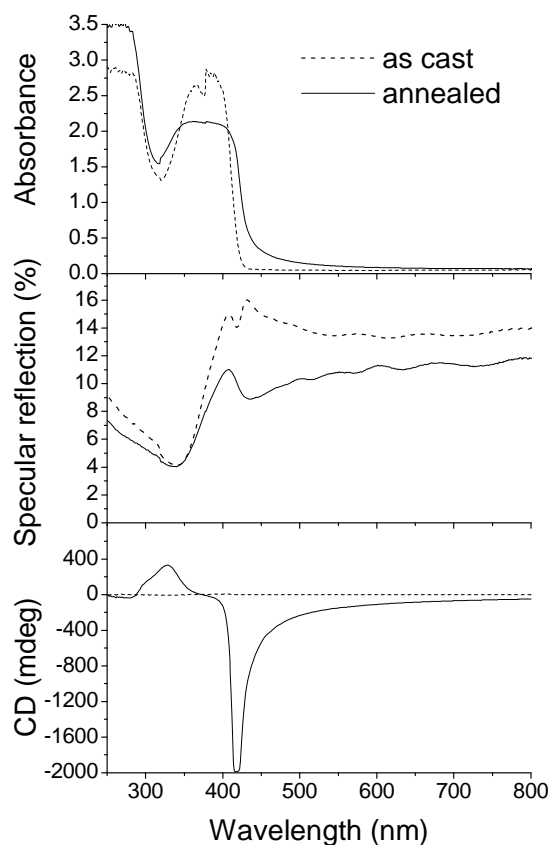


Figure 4: Absorbance, reflection and CD spectra of polyfluorene PF811 films as cast and after annealing (120 °C for 2 h).

Consistent with earlier reports,^{23,24,28} the CD of the polymer films as cast is very small (less than 10 mdeg in this case). Upon annealing, very large Cotton effects arise in the wavelength interval 410–420 nm that even exceed the detection limit of the commercial spectrometer (2 deg). For wavelengths from 350 to 400 nm, the CD is affected by the pinholes. Curiously, the annealed films show very high CD effects that extended into the wavelength range where the polymer no longer absorbs light (450–650 nm). The CD in this wavelength region (450–650 nm) has different sign from the CD shown in Figure 1 in Chapter 3. This is likely due of the lower molecular weight of the PF811 used here and difference in processing conditions. g_{abs} ' at 543 nm, as calculated using eq. 6, is -4.1×10^{-2} . In this wavelength region, the photon energies are too low to excite the conjugated polymer and an interpretation of the circular differential transmission in this wavelength region in terms of selective absorption of light is

not viable. Possible causes for the differential transmission are either selective reflection of light or selective scattering. Below we first address the selective reflection.

4.3.2 Circular selective reflection

The setup shown in Figure 1 is used to verify the occurrence of circular selective reflection as a result of cholesteric liquid crystalline ordering in the sample. In order to test the setup we first investigated a known cholesteric material with a selective reflection band matched with the wavelength of a HeNe laser.

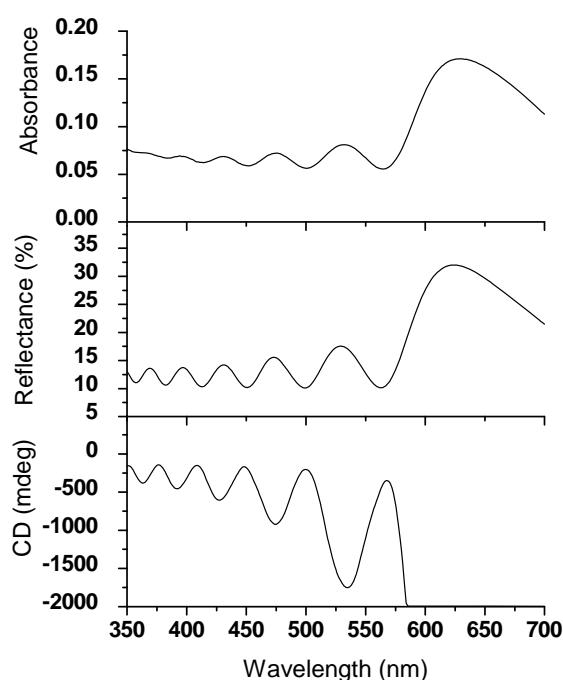


Figure 5: Absorbance, specular reflectance, and CD of a red reflecting, cholesteric liquid crystalline film made from commercially available mesogens (see Experimental).

In Figure 5 some optical characteristics of the cholesteric film are illustrated. The transmission and reflection spectra show a selective reflection band near 630 nm and at shorter wavelengths subsidiary fringes can be observed.⁴⁰ These fringes are characteristic for reflection by thin films. The circular differential transmission for wavelengths in the selective reflection is very high (> 2 deg) and cannot be measured directly with the commercial CD spectrometer. In the fringes, the apparent circular dichroism is much smaller and can be recorded. Here, the apparent g_{abs} ' values are very high: $g_{\text{abs}}' = -1.3$ at 539 nm and $g_{\text{abs}}' = -0.3$ at 363 nm.

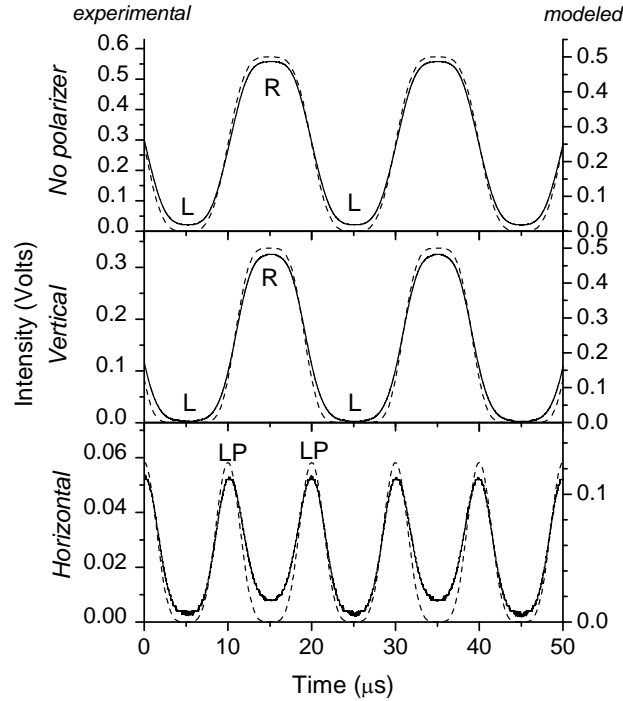


Figure 6: Experimental (solid) and modeled (dashed) intensity-time traces for curves for reflection at normal incidence from a cholesteric liquid crystalline film (see Experimental) as recorded with the setup in Figure 1 at 632 nm wavelength. See also legend Figure 3.

Sample	Phase of mod. cycle (rad)	Polarization at position n ^a				Intensity at photodiode ^b		
		1	2	3	4	No Pol.	V Pol.	H pol.
Glass	0, π , 2π	V	V	V	V	$\tilde{n}/2$ ^c	$\tilde{n}/2$	0
	$\pi/2$	V	R	L	H	$\tilde{n}/2$	0	$\tilde{n}/2$
	$3\pi/2$	V	L	R	H	$\tilde{n}/2$	0	$\tilde{n}/2$
R Cholesteric LC	0, π , 2π	V	V	R	R	1/4	1/8	1/8
	$\pi/2$	V	R	R	V	1/2	1/2	0
	$3\pi/2$	V	L	-	-	0	0	0

(a) V (H): vertical (horizontal) linear polarized light. (b) with no polarizer at pos. 4, Figure 2 and with vertical and horizontal polarizer. (c) $\tilde{n} = [(1-n)/(1+n)]^2$, with n the refractive index of glass.)

Table 1: Polarization of the light at various positions in the setup for selective reflection, see Figure 1.

Predictions for the intensity of light after reflection off glass and a right handed cholesteric liquid crystalline film relative to the intensity of light incident on the film.^a

In Figure 6 we illustrate the selective reflection of light by a cholesteric liquid crystal as measured using the setup illustrated in Figure 1. The solid lines show experimental time-intensity traces for light reflected off the commercial material, while the dotted lines show predictions for an idealized circular selective reflector. When the linear polarizer in front of the detector (at pos. 4 in Figure 1) is left out, selective reflection of right circular polarized light is immediately apparent. Upon inserting a linear polarizer, we can selectively probe for light that has retained its circular polarization after being reflected. With a vertical polarizer the intensity of right circular polarized light is comparable to that in the absence of the

polarizer but with a horizontal polarizer the intensity of the reflected R light is reduced to almost zero. This confirms the retention of the circular polarization upon reflection by the cholesteric layer. Analyzing the time intensity trace with the vertical linear polarizer using eq. 12 we find a very large g value: $g_{\text{refl}}^{\text{LL,RR}} = -1.5$. Upon close inspection of the time trace with the horizontal linear polarizer, we see there is some reflected intensity when right light is incident on the film. This may be explained in terms of some depolarization of the light upon reflection. Using eq. 13 we find $g_{\text{refl}}^{\text{LR,RL}} = -0.7$. Control experiments performed on glass (Figure 3) yield g_{refl} values around 2×10^{-3} , which we consider as the detection limit for the current setup. With the horizontal polarizer, we see a maximum in the reflected intensity when linear, vertical polarized light is incident on the film. Of this linearly polarized incident light, the right circular component is reflected and its intensity is reduced by a factor 0.5 at the beam splitter and by another factor 0.5 at the horizontal polarizer, where a linear component of the circular polarized reflected light is selected. In total, the intensity of the reflected light at the detector is then at maximum 1/8 of the intensity of light incident on the film.

In summary, reflection measurements on a cholesteric film illustrate the usefulness of the optical setup in Figure 1 for measuring the selective reflection of light at normal incidence. We find that reflection of light by a thin film of cholesteric material is highly circular selective, even when the wavelength of light differs considerably from the pitch of the cholesteric stack. We now turn our attention to possible selective reflection of light by films of PF811. In Figure 7 we show the intensity-time trace for reflection of light with 543 nm wavelength from a 1.1 μm thick film of PF811. As can be seen, the traces resemble more strongly to those of the glass substrate (Figure 3) than those of the cholesteric LC material (Figure 6). In particular, the intensity of reflected light recorded with the vertical polarizer reaches a minimum for circular polarized incident light and shows no appreciable selectivity ($g_{\text{refl}}^{\text{LL,RR}} = -3 \times 10^{-3}$, Table 2) taking into account the experimental uncertainty (Table 2, data for glass).

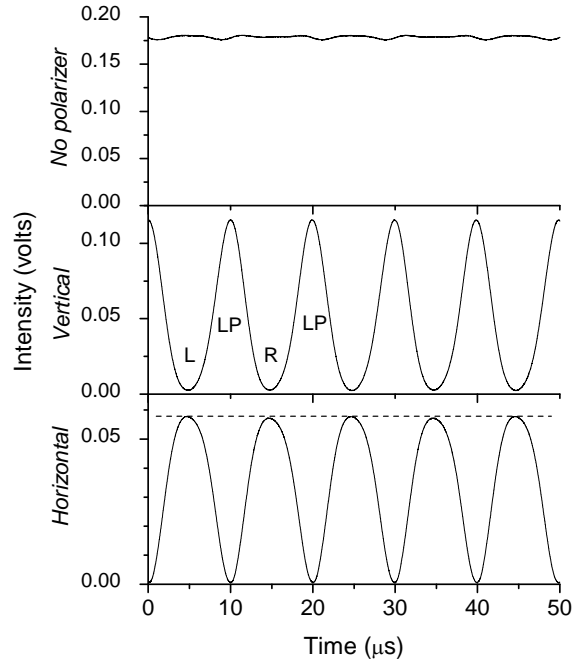


Figure 7: Intensity-time curves for reflection of time modulated circularly polarized light with 543 nm wavelength, reflected by an annealed film of PF811. See also legend Figure 4.

Sample	Dissymmetry ratio	Wavelength (nm)				
		435	458	488	542	632
Glass	$g_{\text{refl}}^{\text{RL,LR}}$	8×10^{-4}	4×10^{-4}	4×10^{-4}	1×10^{-3}	2×10^{-3}
	$g_{\text{refl}}^{\text{LL,RR}}$	-6×10^{-4}	-7×10^{-4}	-1×10^{-3}	-2×10^{-3}	-2×10^{-3}
Cholesteric LC	$g_{\text{refl}}^{\text{LL,RR}}$	-0.32	-	-	-0.95	-1.5
PF811	$g_{\text{refl}}^{\text{LL,RR}}$	-	-2×10^{-3}	-2×10^{-3}	-3×10^{-3}	-5×10^{-3}

Table 2: g_{refl} values obtained by selective reflection experiments on glass, cholesteric liquid crystalline film and annealed polyfluorene film at different wavelengths of incident circularly polarized light.

In Figure 8 we show additional measurements at 458 nm including the vertical polarizer. Also at this wavelength the selectivity of the reflection is very low ($g_{\text{refl}}^{\text{LL,RR}} = -2 \times 10^{-3}$, Table 2). The fact that the intensity of reflected light reaches a minimum when circular polarized light is incident on the film indicates that possible Bragg type reflection from the bulk of the polymer layer is insignificant in comparison with reflection at the dielectric interfaces air-polymer and/or polymer-glass. This finding also holds for the other wavelengths investigated in the range 458–632 nm. If circular differential reflection were to be the sole cause of the differential transmission, it is expected that $g_{\text{refl}} = g_{\text{abs}}$ but this is clearly not the case. Therefore we conclude that the reflection measurement do not give any indication for circular selective reflection as the origin of the anomalously high circular differential transmission of the polyfluorene films.

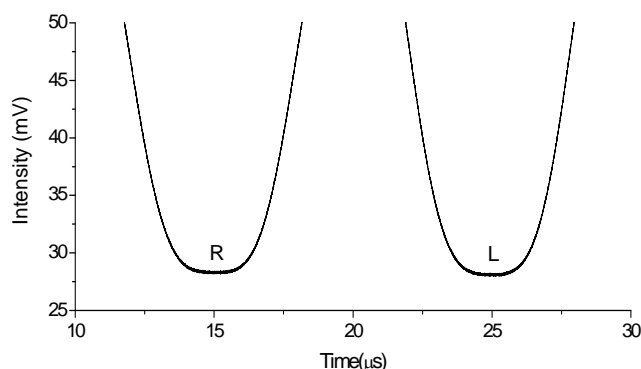


Figure 8: Intensity-time curve for reflection of time modulated circularly polarized light with 458 nm wavelength, reflected by an annealed film of PF811. A vertical polarizer has been inserted before the photodiode.

4.3.3 Circular selective scattering

Apart from selective reflection, also circular selective scattering of light may contribute to the circular differential transmission for the films of PF811 and $\lambda > 450$ nm. Therefore circular selective scattering was evaluated experimentally using an integrating sphere as shown in Figure 1. The detection limit for circular selective scattering was set by testing a solution of achiral ZnO nanoparticles in acetone. In addition a film of ZnO particles drop cast on a glass slide was evaluated (Table 3). The g_{scat} calculated from these control experiments is generally in the order of 10^{-3} .

In Figure 9 we show the intensity vs time trace for light transmitted through the film of PF811 and also for the light scattered by the film. Transmission measurements clearly indicate preferential transmission of left circular polarized light, which is in agreement with the sign of the CD effect in Figure 4. Moreover, the g -value determined for transmission g_{trans} in the integrating sphere measurement (see Figure 10) matches quite well with the g_{trans} value as calculated from conventional absorbance and CD measurements in Figure 4, using eq. 11.

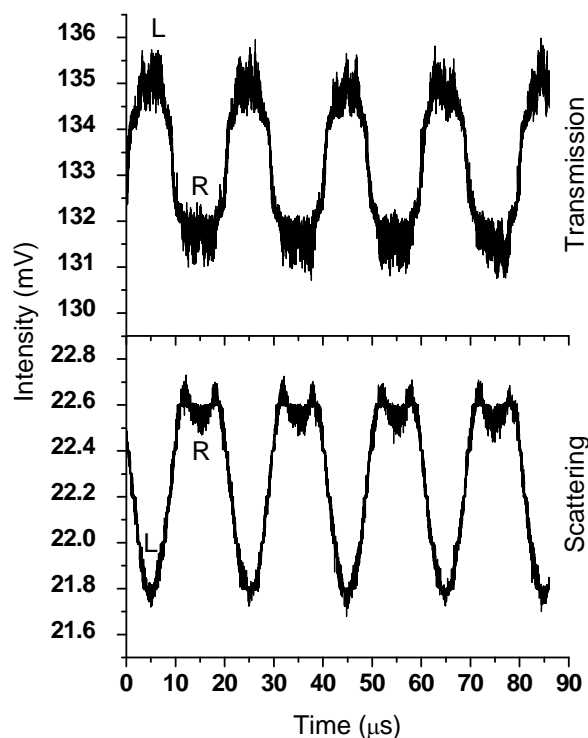


Figure 9: Intensity-time curves for transmitted (upper) and scattered (lower) light of annealed (120 °C, 2 h) film of PF811 at 458 nm wavelength upon irradiation with time modulated circularly polarized incident light using an integrating sphere (Figure 1)

Wavelength (in nm)	Polyfluorene film			ZnO/Acetone	
	$g_{\text{scat}}(\times 10^{-2})$ polymer side	$g_{\text{scat}}(\times 10^{-2})$ glass side	$g_{\text{scat}}(\times 10^{-2})$ rotated 90° ^a	Solution $g_{\text{scat}}(\times 10^{-2})$	Film $g_{\text{scat}}(\times 10^{-2})$
458	-3.7	-3.8	-	-	-
476	-3.6	-4.0	-	-	-
488	-3.0	-4.0	-3.6	-0.1	-0.1
542	-5.0	-5.0	-4.0	-0.05	-0.2
632	-3.3	-3.0	-3.2	-	-

a) Rotated 90° around the normal to the film. Illumination incident on the polymer side.

Table 3: Wavelength dependent g_{scat} values of annealed polyfluorene film and ZnO nanoparticles.

The circular differential scattering signal recorded simultaneously with the differential transmission, shows preferential scattering of right circular polarized incident light by the film of PF811 (Figure 9). The g value for scattering at 458 nm is quite high, $g_{\text{scat}} = -3.7 \times 10^{-2}$, and well above the detection limit as determined from the measurements on achiral material. In addition, scattering measurements with light incident on the back side of the film were performed as well as measurement on films rotated 90° around the normal vector. All these measurements yield very similar g_{scat} values. The g_{scat} values from the experiment can be compared to those calculated using eq. 10, assuming that all differential transmission arises

from selective scattering. For 458 nm wavelength this yields $g_{\text{scat}} = -3 \times 10^{-2}$, a value close to that obtained with direct scattering measurements (Figure 10).

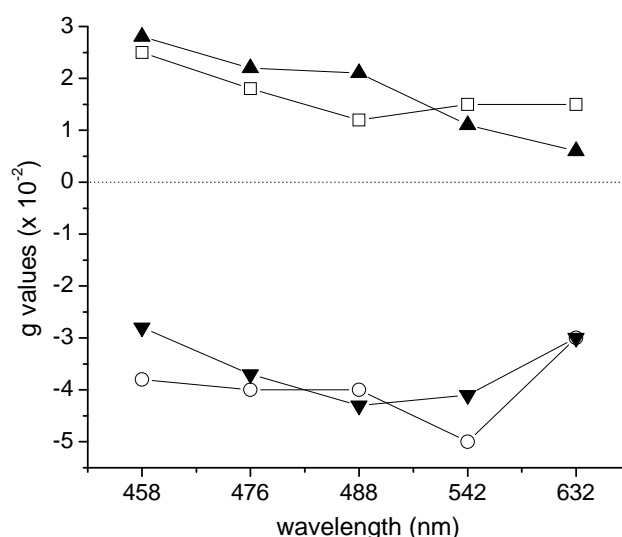


Figure 10: g -Values for transmission g_{trans} , at different wavelengths measured directly with setup illustrated in Figure 1 (\square -) and calculated from data in Figure 5 using eq. (11) (\blacktriangle -). g -Values for scattering g_{scat} measured with an integrating sphere (\circ -) and calculated using eq. (7) from data in Figure 5 (\blacktriangledown -), assuming that all differential transmission is due to selective scattering.

These transmission and scattering measurements have been extended to other wavelengths and the results are summarized graphically in Figure 10. As can be seen, values for g_{scat} from measurements of the intensity of scattered light and values calculated for g_{scat} from differential transmission measurement differ at most by 30 % from one another. This implies that the circular differential transmission for wavelengths $\lambda > 450$ nm can be accounted for in an almost quantitative way by circular selective scattering of light.

4.4 Conclusion

Annealed films of chiral polyfluorene show strong circular differential scattering of light for wavelengths longer than those corresponding to the allowed S_0 - S_1 transition. In contrast, circular selective reflection of light makes up only an insignificant contribution to the circular differential transmission of light. These measurements provide the first quantitative analysis of scattering and reflection for chiral π -conjugated polymers, which may, in a next step, be interpreted in terms of the arrangement of the chiral polymer chains in the film. The relatively high values of the scattered intensity are consistent with the presence of relative small, poorly aligned domains within the film. The latter inference is consistent with optical microscopy which yields a featureless image, without any indications for the presence large birefringent ordered domains. In this study we have not yet studied the optical properties of the film for wavelengths resonant with the lowest allowed optical transition of the polymer and the interesting question arises whether the optical properties of the film for these wavelengths are

influenced by the mesoscopic structure of the film. Here, control over the mesoscopic ordering, may allow one influence the in and out-coupling of light leading to enhanced absorption or emission.

References

1. Grimsdale, A.C.; Müllen, K. *Adv. Polym. Sci.* **2006**, *199*, 1.
2. Scherf, U.; List, E. *Adv. Mater.* **2002**, *14*, 477.
3. Neher, D. *Macromol. Rapid. Commun.* **2001**, *22*, 1365.
4. Knaapila, M.; Stepanyan, R.; Lyons, B.P.; Torkkeli, M.; Monkman, A.P.; *Adv. Funct. Mater.* **2006**, *16*, 599.
5. Zhang, F.; Mammo, W.; Andersson, L. M.; Admassie, S.; Andersson, M.R.; Inganäs, O. *Adv. Mater.* **2006**, *18*, 2169.
6. Wang, P.; Abrusci, A.; Wong, H.M.P.; Svensson, M.; Andersson, M.R.; Greenham, N.C. *Nano Lett.* **2006**, *6*, 1789.
7. Shikler, R.; Chiesa, M.; Friend, R.H. *Macromolecules* **2006**, *39*, 5393.
8. Chen, P.; Yang, G.; Liu, T.; Li T.; Wang, M.; Huang, W. *Polym. Int.* **2006**, *55*, 473.
9. Sirringhaus, H.; Wilson, R.J.; Friend, R.H.; Inbasekaran, M.; Wu, W.; Woo, E.P.; Grell, M.; Bradley, D.D.C. *Appl. Phys. Lett.* **2000**, *77*, 406.
10. Chunwaschirasiri, W.; Tanto, B.; Huber, D.L.; Winokur, M.J. *Phys. Rev. Lett.* **2005**, *94*, 107402.
11. Grell, M.; Bradley, D.D.C.; Inbasekaran, M.; Woo, E.P. *Adv. Mater.* **1997**, *9*, 798.
12. Chen, S.H.; Chou, H.L.; Su, A.C.; Chen, S.A. *Macromolecules* **2004**, *37*, 6833.
13. Grell, M.; Bradley, D.D.C.; Ungar, G.; Hill, J.; Whitehead, K.S. *Macromolecules*, **1999**, *32*, 5810.
14. Chen, S.H.; Su, A.C.; Chen S.A. *J. Phys. Chem. B* **2005**, *109*, 10067.
15. Dias, F.B.; Morgado, J.; Macanita, A.L.; Da Costa, F.P.; Burrows, H.D.; Monkman, A.P. *Macromolecules* **2006**, *39*, 5854.
16. Chen, S.H.; Chou, H.L.; Su, A.C.; Chen, S.A. *J. Phys. Chem. B* **2006**, *110*, 4007.
17. Teetsov, J.; Fox, M.A. *J. Mater. Chem.* **1999**, *9*, 2117.
18. Lieser, G.; Oda, M.; Miteva, T.; Meisel, A.; Nothofer, H.G.; Scherf, U.; Neher, D. *Macromolecules* **2000**, *33*, 4490.
19. Chi, C.; Lieser, G.; Enkelmann, V.; Wegner, G. *Macromol. Chem. Phys.* **2005**, *206*, 1597.
20. Marcon, V.; Van der Vegt, N.; Wegner, G.; Guido Raos, G. *J. Phys. Chem. B* **2006**, *110*, 5253.
21. Grell, M.; Knoll, W.; Lupo, D.; Meisel, A.; Miteva, T.; Neher, D.; Nothofer, H.-G.; Scherf, U.; Yasuda, A. *Adv. Mater.* **1999**, *11*, 671.
22. (a) Chung, S.-F.; Wen, T.-C.; Chou, W.-Y.; Guo, T.-F. *Jpn. J. Appl. Phys.* **2006**, *45*, L60. (b) Misaki, M.; Ueda, Y.; Nagamatsu, S.; Chikamatsu, M.; Yoshida, Y.; Tanigaki, N.; Yase, K. *Appl. Phys. Lett.* **2005**, *87*, 243503. (c) Sakamoto, K.; Usami, K.; Uehara, Y.; Ushioda, S. *Coll. Surfaces A* **2006**, *284-285*, 635. (d) Trajkovska, A.; Kim, C.; Marshall, K.L.; Mourey, T.H.; Chen, S.H. *Macromolecules* **2006**, *39*, 6983. (e) Yang, X.H.; Neher, D.; Lucht, S.; Nothofer, H.; Guntner, R.; Scherf, U.; Hagen, R., Kostromine, S. *Appl. Phys. Lett.* **2002**, *81*, 2319.
23. Oda, M.; Nothofer, H.-G.; Lieser, G.; Scherf, U.; Meskers, S.C.J.; Neher, D. *Adv. Mater.* **2000**, *12*, 362.
24. Oda, M., Meskers, S.C.J., Nothofer, H.G., Scherf, U., Neher, D. *Synth. Met.* **2000**, *111*, 575.
25. Nothofer, H.-G.; Oda, M.; Neher, D.; Scherf, U. *Proc. SPIE - Int. Soc. Opt. Eng.* **2000**, *4107*, 19.
26. Nothofer, H.-G.; Meisel, A.; Miteva, T.; Neher, D.; Forster, M.; Oda, M.; Lieser, G.; Sainova, D.; Yasuda, A.; Lupo, D.; Knoll, W.; Scherf, U. *Macromol. Symp.* **2000**, *154*, 139.
27. Oda, M.; Nothofer, H.-G.; Scherf, U.; Sunjic, V.; Richter, D.; Regenstern, W.; Neher, D. *Macromolecules* **2002**, *35*, 6792.
28. Craig, M.R.; Jonkheijm, P.; Meskers, S.C.J.; Schenning, A.P.H.J.; Meijer, E.W. *Adv. Mater.* **2003**, *15*, 1435.
29. Geng, Y.H.; Trajkovska, A.; Katsis, D.; Ou, J.J.; Culligan, S.W.; Chen, S.H. *J. Am. Chem. Soc.* **2002**, *124*, 8337.

30. Geng, Y.H.; Trajkovska, A.; Culligan, S.W.; Ou, J.J.; Chen, H.M.P.; Katsis, D.; Chen, S.H. *J. Am. Chem. Soc.* **2003**, *125*, 14032.
31. De Vries, H. L. *Acta Cryst.* **1951**, *4*, 219.
32. Bustamante, C.; Tinoco, I., Jr.; Maestre, M.F. *Proc. Natl. Acad. Sci. USA* **1983**, *80*, 3568.
33. Keller, D.; Bustamante, C. *J. Chem. Phys.* **1986**, *84*, 2972.
34. Phillips, C.L.; Mickols, W.E.; Maestre, M.F.; Tinoco, I., Jr. *Biochemistry* **1986**, *25*, 7803.
35. Tinoco, I.; Jr.; Mickols, W.; Maestre, M.F.; Bustamante, C. *Ann. Rev. Biophys. Biophys. Chem.* **1987**, *16*, 319.
36. Ivanov, O.V.; Sementsov, D.I. *Cryst. Rep.* **2000**, *45*, 487.
37. Silverman, M.P.; Badoz, J.; Briat, B. *Opt. Lett.* **1992**, *17*, 886.
38. Schellman, J.; Jensen, H.P. *Chem. Rev.* **1987**, *87*, 1359.
39. Tinoco, I., Jr.; Maestre, M.F.; Bustamante, C.; Keller, D. *Pure & Appl. Chem.* **1984**, *56*, 1423.
40. Chandrasekhar, S. *Liquid Crystals* Cambridge University Press 1992, Cambridge.

Circular Dichroism in photoinduced triplet-triplet absorption in *chiral* polyfluorene

Abstract. At 77 K, thermally annealed films of chiral poly[9,9-bis((3*S*)-3,7-dimethyloctyl)-2,7-fluorene] show photoinduced absorption (PIA) band near 1.5 eV due to a transition from the lowest triplet state to a higher triplet state. This photoinduced absorption is found to show circular dichroism CD. Dividing this CD by the magnitude of the PIA, we find that the selectivity for absorption of left circular polarized light over right circularly polarized light is remarkably high and characterized by a dissymmetry ratio $g = +0.2$. The unusual magnitude of g is interpreted as arising from extrinsic CD, *i.e.* from the interaction of the local linear polarization of the triplet-triplet absorption with the linear birefringence of the surrounding polymer matrix.

5.1 Introduction

Circular dichroism spectroscopy involves the measurement of the difference in absorbance between left and right circular polarized light by chiral molecules or materials. This form of linear spectroscopy is usually performed in continuous wave mode and is normally applied to the samples in their electronic ground state. In the last few decades, this method has been extended to cover circularly polarized absorption from excited states and the associated effect can be termed photoinduced circular dichroism (PICD). PICD provides information on the structure and dynamics of the chiral molecules in their excited state. The first reports described circular dichroism in photostationary triplet-triplet absorption.¹ Later developments involved time resolved methods using short light pulses to excite the sample.²⁻⁴ These methods have been used to study light induced conformational changes in e.g. small molecules⁵ and proteins.⁶ More recently, also time resolved vibrational circular dichroism has been reported.⁷ So far photoinduced circular dichroism (PICD) has been carried out on (frozen) solutions of molecules. Here we study PICD on films of chiral poly[9,9-bis((3*S*)-3,7-dimethyloctyl)-2,7-fluorene] (PF811).

Polyfluorenes are π -conjugated polymers that are well known for their blue light-emitting properties in polymer light-emitting diodes (pLED). Use of *chiral* polyfluorene polymers in pLEDs results in circular polarized electroluminescence with a surprisingly large degree of circular polarization $g_{EL}=2(I_L-I_R)/(I_L+I_R)$ that can reach up to 1. This large degree of polarization g is achieved only after thermal annealing of the film to its liquid crystalline state followed by rapid cooling. Such large values of g have been interpreted in terms of a cholesteric arrangement of polymer chains in a vitrified chiral nematic liquid crystalline state.⁸

The photophysical behavior of polyfluorene has been investigated in considerable detail. In a pure film, a long lived excited state has been observed which is assigned to an excited triplet state (T_1).⁹⁻¹² The T_1 state gives rise to a photoinduced absorption (PIA) resulting from a dipole allowed transition from the T_1 to a higher lying triplet state T_n . The PIA signal shows a single, relatively narrow band in the near infrared region of the spectrum with a maximum intensity around 1.5 eV.

Here we investigate the circular dichroism in the T_1 - T_n photoinduced absorption in a thermally annealed film of chiral polyfluorene. The main question is whether the large degree of circular polarization observed in ground state chiroptical measurements also transfers to the excited state absorption. The results are of importance in understanding the origin of the chiroptical response in solid films of π -conjugated polymer. Excited state optical properties of polyfluorenes have been utilized to realize optical switching in polymer films.¹³ Results reported here also provide an insight into the feasibility of using the circular polarization of light in all optical switching in polymer materials.

5.2 Experimental section

5.2.1 Materials and preparation

The films were prepared by spincoating a chloroform solution (22.5 mg/ml) of chiral polyfluorene (poly[9,9-bis((3*S*)-3,7-dimethyloctyl)-2,7-fluorene], PF811, Figure 2, Chapter 1) at 1000 rpm. The details regarding polymer synthesis can be found in Chapter 3. The thickness of the film was measured by Veeco surface profilometer and was found to be ~290 nm. Thermal annealing of the films was done in air at 120 °C for 10 minutes. UV-VIS measurements were done on a Perkin Elmer Lambda 900 UV/VIS/NIR spectrometer. The CD effect in this particular annealed film with ellipticity > 2000 mdeg, was measured using a Perkin Elmer Lambda 900 UV/VIS/NIR spectrometer and a circular sheet polarizer (Oriel). The absorbance and g_{abs} of the spincoated film are shown in Figure 1 below. The band shape of the CD spectrum of this film is similar to seen before (Figure 1, Chapter 3).

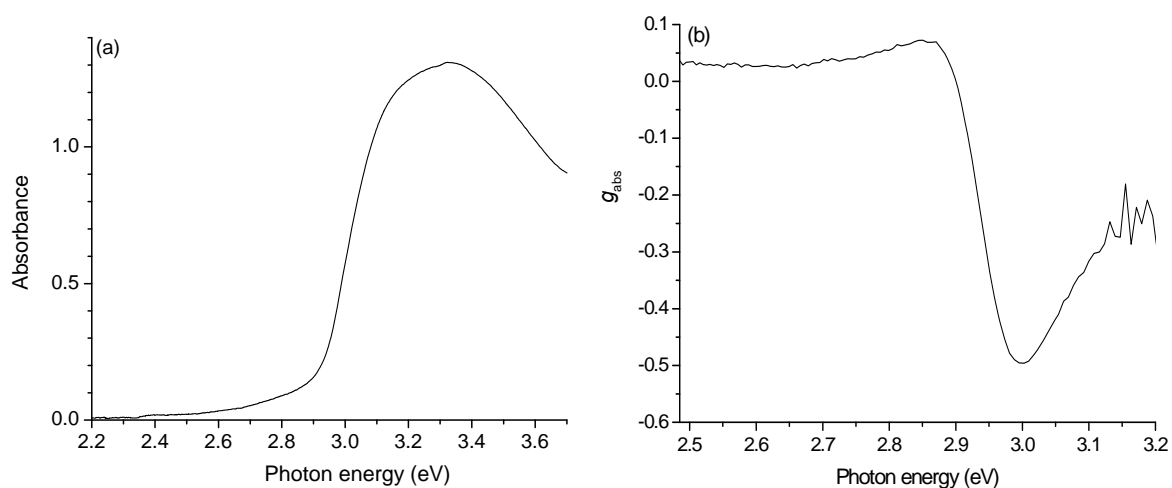


Figure 1: (a) Absorbance, and (b) CD spectrum of a thick PF811 film.

5.2.2 Tailor made photoinduced circular dichroism (PICD) set up

In order to measure photoinduced absorbance effects, a tailor-made set up was installed as shown in Figure 2. The sample was held in an N_2 flow cryostat at $T = 77$ K. The incident laser light (argon ion laser, Spectra-Physics type 2020, 365 nm, 60 mW) was allowed to pass through a chopper at 75 Hz. White light (halogen lamp) was used as probe. The intensity of the white light transmitted through the sample (T) was determined first by modulating it at a known frequency. In order to probe the PIA signal, the white light intensity was kept constant, whereas the laser light was modulated at 75 Hz. Fluorescence corrections were made to the PIA signal. However, the entire fluorescence could not be rectified. The setup measures PIA and fluorescence in separate scans and takes a difference in the values to obtain the corrected PIA. Owing to very high fluorescence from these thick annealed films, 100% corrections are not achieved. Some residual fluorescence signal remains in the high energy region of the PIA spectrum around 2.8 eV.

When the modulated laser light illuminates the sample during one half of the modulation period, the photoinduced absorption associated with the triplet-triplet transition gives rise to a reduction of the transmission ($\Delta T^{\text{ONOFF}} = T^{\text{ON}} - T^{\text{OFF}}$) at wavelength of the probe light. The associated PIA signal is the normalized differential transmission ($\Delta T^{\text{ONOFF}}/T$).

Defining absorbance A in the traditional way we write:

$$A = -\log\left(\frac{T}{T_0}\right) \quad (1)$$

where T_0 is the transmitted light intensity and T is the intensity of the incident light.

The differential absorbance (PIA) recorded between on and off laser modes can now be expressed as:

$$\begin{aligned} \text{PIA} &= \Delta A^{\text{ONOFF}} = A^{\text{ON}} - A^{\text{OFF}} = -\log\left(\frac{T^{\text{ON}}}{T_0}\right) + \log\left(\frac{T^{\text{OFF}}}{T_0}\right) \\ &= -\log\left(\frac{T^{\text{ON}}}{T^{\text{OFF}}}\right) = \frac{-1}{\ln 10} \cdot \ln\left(\frac{T^{\text{ON}}}{T^{\text{OFF}}}\right) \cong \frac{-1}{\ln 10} \left(\frac{\Delta T^{\text{ONOFF}}}{T_0}\right) \\ \rightarrow \text{PIA} &= \frac{-1}{\ln 10} \left(\frac{\Delta T^{\text{ONOFF}}}{T_0}\right) \end{aligned} \quad (2)$$

where we have used the Taylor expansion to approximate the logarithmic function:

$$-\ln\left(\frac{T^{\text{ON}}}{T^{\text{OFF}}}\right) \cong 1 - \frac{T^{\text{ON}}}{T^{\text{OFF}}} \cong \frac{T^{\text{OFF}} - T^{\text{ON}}}{T_0} = -\frac{\Delta T}{T_0} \quad (3)$$

The PIA signal was recorded by feeding the detector output directly into a lock-in amplifier (Stanford research systems SR830) and monitoring the intensity of transmitted light with chopper frequency as the reference (Figure 2). The detector signal was fed in directly to lock-in amplifier (B) bypassing (A).

In order to measure PICD, the probe light has to be circularly polarized. This was achieved by passing the probe light through a linear calcite polarizer and subsequently through a photoelastic modulator (PEM, Morvue) held at $\lambda/4$ retardation wavelength and rotated by 45 degrees from the vertical axis. The PEM operates at 50 kHz. After passing through the sample, the probe light is depolarized using a Rochon prism or alternatively a multicrystalline sapphire plate. The laser light used to excite the sample was also depolarized in order to avoid photo-selective excitation of polymer chains with a particular orientation.

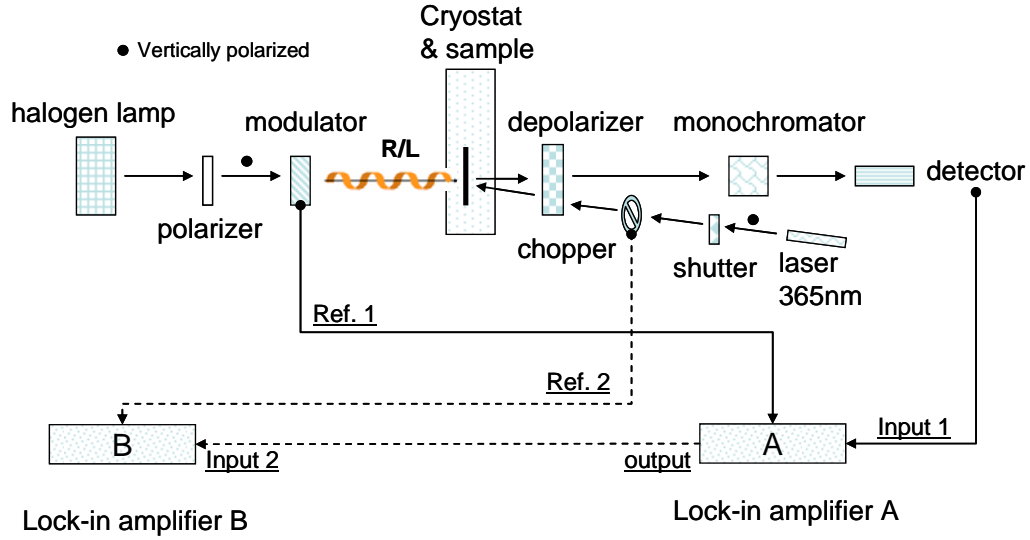


Figure 2: PICD set-up.

To measure the PICD a double lock-in method was used. The signal from the detector is first analyzed for components at 50 kHz using a lock-in amplifier (A). This records the circular differential transmission by the sample. Illuminating the sample with the time-modulated laser light, the circular differential transmission signal picked up by amplifier (A) will now oscillate between two values. One corresponds to the ground state CD and the other to the ground state CD plus the PICD. This modulation occurs at the same frequency as the modulation of the laser light and can be recorded by feeding the output of lock-in amplifier (A) into a second lock-in amplifier (B) with the frequency of the chopper (modulating the laser light) as reference. Here it is important that the time constant for the first lock-in amplifier (A) is set short enough in order for its output to follow the second modulation. Here we used a time constant of 10 μsec . The lock-in amplifier is autophased during the measurement of scattered laser light through the sample. The phase angle recorded for PIA and PICD measurements is relative to this measurement.

In summary, the output signal of lock-in amplifier (A) corresponds the circular differential transmission ($\Delta T_{LR} = T_L - T_R$) and oscillates between $\Delta T_{LR}^{\text{ON}}$ and $\Delta T_{LR}^{\text{OFF}}$. These latter values are related to the circular dichroism in the dark and light period of the modulation cycle:

$$\begin{aligned} \Delta A_{\text{CD}}^{\text{OFF}} &= A_{\text{L}}^{\text{OFF}} - A_{\text{R}}^{\text{OFF}} = -\log\left(\frac{T_{\text{L}}^{\text{OFF}}}{T^{\text{OFF}}}\right) + \log\left(\frac{T_{\text{R}}^{\text{OFF}}}{T^{\text{OFF}}}\right) \\ &= -\log\left(\frac{T_{\text{L}}^{\text{OFF}}}{T_{\text{R}}^{\text{OFF}}}\right) \cong \frac{-1}{\ln 10} \frac{T_{\text{R}}^{\text{OFF}} - T_{\text{L}}^{\text{OFF}}}{T^{\text{OFF}}} = -\frac{-1}{\ln 10} \left(\frac{\Delta T_{\text{LR}}^{\text{OFF}}}{T^{\text{OFF}}}\right) \end{aligned}$$

$$\rightarrow \Delta A_{CD}^{OFF} = -\frac{1}{\ln 10} \left(\frac{\Delta T_{LR}^{OFF}}{T^{OFF}} \right) \quad (4)$$

$$\begin{aligned} \Delta A_{CD}^{ON} &= A_L^{OFF} - A_R^{OFF} = -\log \left(\frac{T_L^{ON}}{T^{ON}} \right) + \log \left(\frac{T_R^{ON}}{T^{OFF}} \right) \\ &= -\log \left(\frac{T_L^{ON}}{T_R^{ON}} \right) \cong \frac{-1}{\ln 10} \frac{T_R^{ON} - T_L^{ON}}{T^{ON}} = -\frac{1}{\ln 10} \left(\frac{\Delta T_{LR}^{ON}}{T^{ON}} \right) \end{aligned}$$

$$\rightarrow \Delta A_{CD}^{ON} = -\frac{1}{\ln 10} \left(\frac{\Delta T_{LR}^{ON}}{T^{ON}} \right) \quad (5)$$

Lock-in amplifier (B) is used to record the amplitude of this oscillation (ΔT_{LR}^{ON} and ΔT_{LR}^{OFF}) and the PICD can now be obtained by dividing this output by the white light intensity T using the relation.

$$PICD = \Delta A_{CD}^{ON} - \Delta A_{CD}^{OFF} \cong \frac{-1}{\ln 10} \left[\frac{\Delta T_{LR}^{ON}}{T^{ON}} - \frac{\Delta T_{LR}^{OFF}}{T^{OFF}} \right] \cong \frac{-1}{\ln 10} \left[\frac{\Delta T_{LR}^{ON} - \Delta T_{LR}^{OFF}}{T_0} \right] \quad (6)$$

The PICD is expected to be linearly dependent on the magnitude of the photoinduced absorption. Therefore this quantity itself is not very characteristic for the material. If we divide the PICD by the PIA, we obtain a quantity, g_{PICD} which would describe the degree of circular polarization in the photoinduced CD. g_{PICD} is expected to be independent of the experimental parameters controlling the magnitude of the PIA signal.

$$g_{PICD} = \frac{PICD}{|PIA|} \quad (7)$$

Here we take the absolute magnitude of the PIA signal to determine g . In our case we study only pure photoinduced absorption and not bleaching so that the PIA > 0 .

Photoinduced linear dichroism (PILD) can be recorded using the same setup after changing the retardation of the PEM to $\lambda/2$ instead of $\lambda/4$ and detecting the second harmonic of the modulation frequency (i.e. 100 kHz) using lock-in amplifier (A).

5.3 Results and Discussion

5.3.1 PIA experiments on an annealed chiral polyfluorene film

Films of PF811 show PIA in the near infrared region of the spectrum (Figure 3) with a maximum around 1.53 eV. For photon energies lower than 1.4 eV, no significant

photoinduced absorption is observed (Figure 3). This is consistent with triplet-triplet photoinduced absorption in this material.^{9,12} At high photon energies (>2.5 eV), the fluorescence from the polyfluorene can be observed, showing a vibronic progression that is characteristic for this transition.

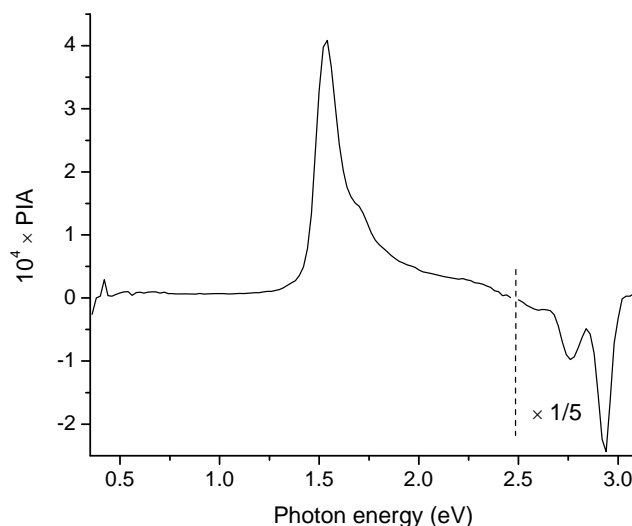


Figure 3: PIA of an annealed film of the PF811 (Power 50 mW, 3.55 eV, modulation frequency 275 Hz, $T = 77\text{K}$)

5.3.2 PICD experiments on annealed chiral polyfluorene film

For films of PF811 we observe a PICD signal (Figure 4a). Here the PICD is plotted along with the PIA signal measured under the same conditions. The PICD reaches a magnitude of approximately 1×10^{-4} at 1.53 eV and this maximum coincides with that of the PIA. The PICD and PIA signals follow practically the same band shape. At the maximum (1.53 eV), the PIA is approximately 5 times larger than the PICD. Because of the similarity in band shape and peak position, we assign the PICD to the triplet-triplet transition of the material. This assignment is further supported by the similar dependence of the two signals on the frequency of modulation of the primary UV excitation beam (Figure 4b). The intensity of both the PIA and PICD decays with increasing frequency with a dependence that may be described by a power law. This indicates a broad distribution of lifetimes for the triplet state with some triplets having a lifetime exceeding 10 ms.

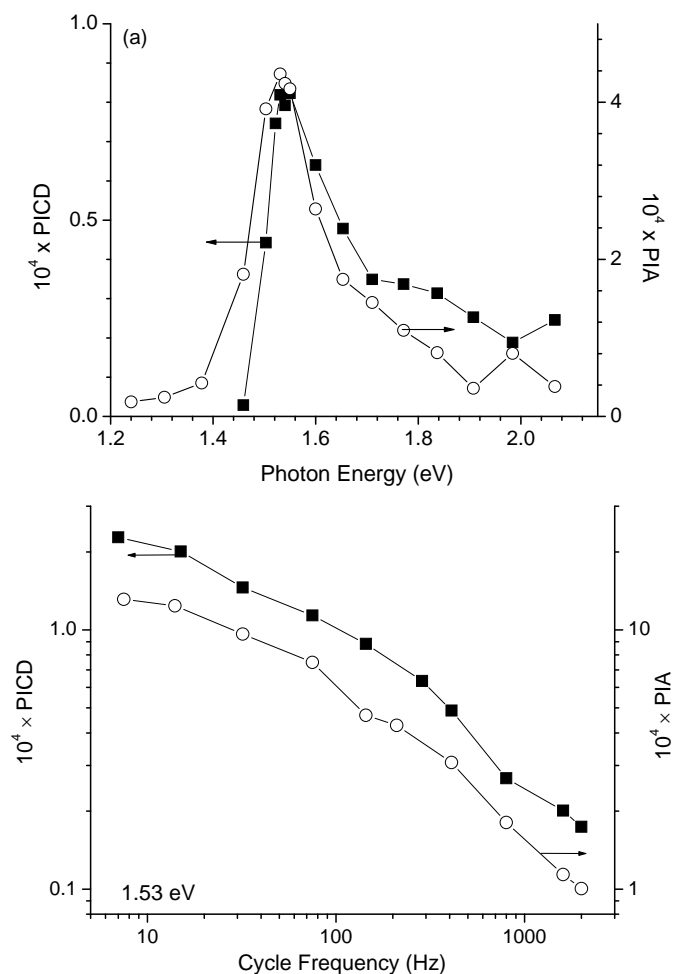


Figure 4: PICD (■-) and PIA (-○-) spectrum of the PF811 film with respect to (a) photon energy, and (b) modulation frequency. The lines joining the points are to guide the eye. Experiments are done at modulation frequency of 75 Hz, at temperature of 77K, and at laser excitation 3.55 eV. The signal is monitored at 1.53 eV.

The dependence of the PICD and PIA signals on the intensity of incident light is also very similar. This is illustrated in Figure 5. When the power of the incident laser light (I) is low (<30 mW), the PIA and PICD vary approximately linearly with I ($\propto I^{0.9}$). At higher power, the dependence of the PIA and PICD signal is clearly sub linear in I . The change in power dependence is accompanied by a change in the phase angle of the PIA and PICD signals. This phase angle is virtually the same for both signals, which further supports the assignment of both signals to a triplet-triplet transition. At low power, the phase angle is close to -37° which indicates that the triplet state has an average lifetime that is comparable in magnitude to the period of the UV modulation (13 ms). At higher power, the phase angle becomes smaller in absolute magnitude, indicating a decrease in the average lifetime of the long lived excited states. This indicates that at high excitation density, the triplet excitations decay via the bimolecular triplet-triplet annihilation mechanism, whereas at low excitation density the triplets decay mainly monomolecularly. This type of behavior is characteristic for triplet excitations in π -conjugated polymers.¹⁴

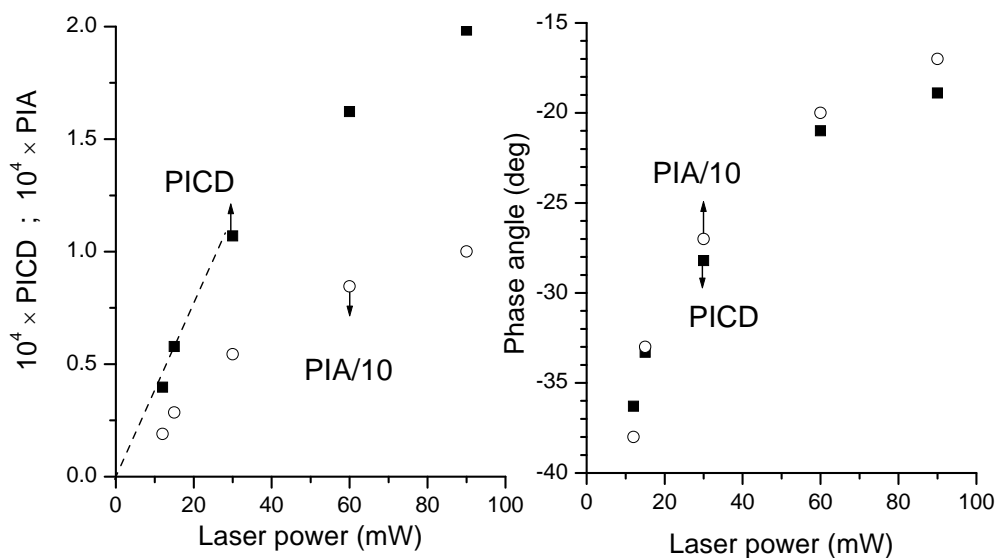


Figure 5: (a) Amplitude and (b) phase angle of the PICD and PIA signals of the PF811 film. Experiments are done at modulation frequency of 75 Hz, at temperature of 77K, and at laser excitation 3.55 eV. The signal is monitored at 1.53 eV.

As discussed above, the PICD and PIA spectra in the neighborhood of the triplet-triplet absorption show a very similar band shape. The band shape of a CD spectrum often gives an indication on the origin of the circular differential absorption. Systems with identical chromophoric groups held in a chiral arrangement usually give rise to a bisignate CD spectrum.¹⁵ Here a positive and a negative CD lobe are separated by a zero crossing that usually occurs at the same photon energy as the maximum of absorbance. This bisignate band shape can be explained by the coupled oscillator model. The monosignate band shape observed in the PICD indicates that the coupled oscillator model does not apply to the PICD. This is of course not surprising, because the density of triplet excitations is very low. Therefore interactions between transition dipole moments for the triplet-triplet transition of two triplet excitations are negligible because of the large distance between the triplet excitations.

An important indication on the origin of the observed PICD comes from considering the magnitude of the degree of circular polarization in the photoinduced triplet-triplet transition PICD: $g_{\text{PICD}} = +0.2$ at 1.53 eV. This value of g_{PICD} found here is considerably larger than reported for the triplet-triplet absorption in binaphthyl derivatives ($g \approx 10^{-3}$)^{1c} or for heme proteins ($g \approx 10^{-4}$).¹⁶ Furthermore it is also much larger than g_{abs} for dipole allowed transitions in helically folded polymers or chiral small molecules in dilute solutions ($g_{\text{abs}} = 10^{-2}$ to 10^{-3}). Because of this discrepancy in magnitude, it seems unlikely that the PICD arises from the helical conformation of the polyfluorene chain that carries the triplet excitation.

In order to check for a possible artifact associated with the combination of a net linear dichroism in the triplet-triplet absorption and a linear birefringence somewhere in the optical system, net linear dichroism in the PIA (PILD) was measured. The degree of linear polarization $g_{\text{PILD}} = 2(I_V - I_H)/(I_V + I_H)$ is found to be very low: at 1.53 eV we measure $|g_{\text{PILD}}| =$

0.006. This is two orders of magnitude lower than g_{PICD} . Hence instrument imperfections resulting in any artificial contributions to the PICD are unlikely.¹⁷

A possible explanation for the large magnitude of g_{PICD} may be given by the extrinsic mechanism for CD effects.¹⁸ This type of mechanism is operative for e.g. cholesteric liquid crystals in which achiral dyes are dissolved.¹⁹ The extrinsic CD arises from a combination of local linear dichroism (LD) of the achiral dye in combination with local linear birefringence (LB) of the liquid crystalline host. Here it is important to stress that in multidomain liquid crystalline samples, the net linear dichroism of the dye molecules can vanish but that the apparent CD signal originating from the combination of local LD and LB can still give a net average effect. To explain the large g values in PICD in a qualitative way, we assume that the annealed PF811 has a multidomain vitrified chiral nematic structure. Because of the multidomain structure of the film, the overall linear dichroism would be negligible. Upon illumination, some chains will host a long lived triplet excitation that gives rise to the allowed triplet-triplet transition. This transition probably has a transition dipole moment that is oriented along the chain direction. These triplet excitations could play a role similar to achiral dye molecules dissolved in a cholesteric matrix. The local anisotropic nature of the individual triplet-triplet transitions may now, in combination with the linear birefringence of the cholesteric matrix surrounding the triplet excitation, give rise to large extrinsic CD.

5.4 Conclusion

Our results show that by making use of the extrinsic mechanism for CD, very large degrees of circular polarization in photoinduced transition of π -conjugated polymers is feasible. In some respect, this may be similar to the use of chiral polyfluorene in light-emitting diodes, where very large degrees of circular polarization can also be achieved. Given the large degrees of circular polarization possible and the reported applications of polyfluorenes in all-optical switching, it becomes interesting to consider the possibility to make use of circular polarization of light in these switching processes.

References

1. (a) Tetreau, C. *J. Phys. Chem.*, **1986**, *90*, 4993. (b) Tetreau, C.; Lavalette, D.; Balan, A. *J. Phys. Chem.* **1985**, *89*, 1699. (c) Tetreau, C.; Lavalette, D.; Cabaret D.; Geratgthy, N.; Welvart, Z. *J. Phys. Chem.* **1983**, *87*, 3234. (d) Lavalette, D.; Tetreau, C. *J. Phys. Chem.* **1983**, *87*, 3226.
2. (a) Goldbeck, R.A.; Kim-Shapiro, D.B.; Klinger, D.S. *Annu. Rev. Phys. Chem.* **1997**, *48*, 453. (b) Klinger, D.S.; Lewis, J.W. *Rev. Chem. Intermediates* **1987**, *8*, 367.
3. (a) Terazima, M. *Mol. Phys.* **1996**, *88*, 1223. (b) Neyer, D.W.; Rahn, L.A.; Chandler, D.W.; Nunes, J.A.; Tong, W.G. *J. Am. Chem. Soc.* **1997**, *119*, 8293.
4. Niezborala, C.; Hache F. *J. Opt. Soc. Am. B* **2007**, *24* 1012.
5. Niezborala, C.; Hache, F. *J. Am. Chem. Soc.* **2008**, *130*, 12783.
6. Xie, X.; Simon, J. D. *J. Am. Chem. Soc.* **1990**, *112*, 7802.

7. (a) Bonmarin, M.; Helbing, J. *Optics Letters* **2008**, *33*, 2086. (b) Rhee, H.; June, Y.-G.; Lee, J.-S.; Lee, K.-K.; Ha, J.-H.; Kim, Z.H.; Jeon, S.-J.; Cho, M. *Nature* **2008**, *458*, 310.
8. (a) Geng, Y.H.; Trajkovska, A.; Katsis, D.; Ou, J.J.; Culligan, S.W.; Chen, S.H. *J. Am. Chem. Soc.* **2002**, *124*, 8337. (b) Geng, Y.H.; Trajkovska, A.; Culligan, S.W.; Ou, J.J.; Chen, H.M.P.; Katsis, D.; Chen, S.H. *J. Am. Chem. Soc.* **2003**, *125*, 14032.
9. (a) King, S.M.; Vaughan, H.L.; Monkman, A.P. *Chem. Phys. Lett.* **2007**, *440*, 268. (b) Monkman, A.; Rothe, C.; King, S.; Dias, F. *Adv. Polym. Sci.* **2008**, *212*, 187.
10. Rothe, C.; King, S.M.; Dias, F.; Monkman, A.P. *Phys. Rev. B* **2004**, *70*, 195213.
11. Cadby, A.J.; Lane, P.A.; Mellor, H.; Martin, S.J.; Grell, M.; Giebeler, C.; Bradley, D.D.C.; Wohlgenannt, M.; An, C.; Vardeny, Z.V. *Phys. Rev. B* **2000**, *62*, 15604.
12. Hayer, A.; Khan, A.L.T.; Friend, R.; Kohler, A. *Phys. Rev. B*, **2005**, *71*, 241302.
13. (a) Virgili, T.; Marinotto, D.; Lanzani, G.; Bradley, D.D.C. *Appl. Phys. Lett.* **2005**, *86*, 091113. (b) Vishnubhatla, K.C.; Clark, J.; Lanzani, G.; Ramponi, R.; Osellame, R.; Virgili, T. *Appl. Phys. Lett.* **2009**, *94*, 041123. (c) Perissinotto, S.; Lanzani, G.; Zavelani-Rossi, M.; Salerno, M.; Gigli, G. *Appl. Phys. Lett.* **2007**, *91*, 191108.
14. van Hal, P.A.; Christiaans, M.P.T.; Wienk, M.M.; Kroon, J.M.; Janssen, R.A.J. *J. Phys. Chem. B* **1999**, *103*, 4352.
15. Berova, N.; Nakanishi, K.; Woody, R.W. *Circular Dichroism: principles and application*, Wiley-VCH **2000**.
16. Dartigalongue, T.; Hache, F. *Chem. Phys. Lett.* **2005**, *415*, 313.
17. Wolffs, M.; George, S.J.; Tomovic, Z.; Meskers, S.C.J.; Schenning, A.P.H.J.; Meijer, E.W. *Angew. Chem. Int. Ed.*, **2007**, *46*, 8203.
18. Saeva, F.D.; Olin, G.R. *J. Am. Chem. Soc.* **1976**, *98*, 2709.
19. Chen, S. H.; Katsis, D.; Mastrangelo, J. C.; Schmid, A.W.; Tsutsui, T.; Blanton, T. N. *Nature* **1999**, *397*, 506.

β -phase in *chiral* polyfluorene forms via a precursor*

Abstract. Chiral poly[9,9-bis((3*S*)-3,7-dimethyloctyl)-2,7-fluorene] shows temperature induced aggregation in 1-octanol. For polymer concentrations > 0.01 mg/ml and cooling rates ≤ 10 °C/h, aggregates form, showing characteristics of the β -phase of polyfluorene. At higher cooling rates and/or lower concentration another type of aggregate forms (α). α and β -phases are distinguished by absorption, fluorescence, and circular dichroism (CD) spectroscopy. Temperature dependent CD and dynamic light scattering show that the β -phase forms only via a precursor aggregate, whose formation is concentration, temperature, and time dependent. The yield of β -phase can be optimized by choosing processing conditions that favor formation of the precursor.

* Girish Lakhwani, Stefan C.J. Meskers *Macromolecules*, **2009**, 42, 4220.

6.1 Introduction

In the previous chapters we discovered chiroptical properties of chiral polyfluorene, poly[9,9-bis((3*S*)-3,7-dimethyloctyl)-2,7-fluorene] (PF811). Not only did we define intensive and extensive properties in films of PF811, but we also saw other circularly selective phenomena in scattering and photoinduced absorbance. What has been discussed briefly so far is the chiroptical properties of PF811 in solutions. In chapter 3, solvent-induced aggregation was discussed, whereas here we study temperature induced aggregation in detail. Here we investigate PF811 in solution and identify different aggregates (phases) by CD spectroscopy. We further investigate into the mechanism of formation of these aggregates and develop an understanding on them *via* a phase diagram.

Crystallization of macromolecules can be a multistep process. In a number of cases, intermediates present in the early stages of crystallization have been identified such as transient mesophases,¹ precrystalline aggregates,² or crystallization precursors.³ It has been recognized that the final morphology obtained in polymer processing is often imposed by such precursor structures present early on in the crystallization process.⁴ For π -conjugated polymers, film morphology directly influences their optoelectronic properties, such as charge carrier mobility and light emission characteristics.⁵ Therefore, when trying to optimize these properties, knowledge of precursor structures in the aggregation of π -conjugated chains is of paramount importance. Here we investigate aggregation of *chiral* polyfluorene PF811^{6,7} in 1-octanol and distinguish two chiral polymorphs (α and β). For the formation of only one of these polymorphs, we identify a precursor structure. Formation of this precursor is a time and concentration dependent process. By choosing processing conditions favorable to precursor formation, one can control which of the polymorphs is formed upon aggregation (α or β).

The polyfluorenes constitute a class of π -conjugated polymers for which organization in solid phase and functional properties have been investigated in considerable detail. For instance, poly[9,9-di-*n*-octyl-2,7-fluorene] (PFO)⁸ can form a crystalline phase (α) below 160 °C. Besides this α -phase, also a mesomorphic β -phase has been identified⁹ which can be induced by *e.g.* solvent treatment. This β -phase can be distinguished from α by its optical properties: the absorption and luminescence band associated with the allowed transition between the ground and the lowest excited singlet state for β are red shifted in comparison with those for α -phase. This indicates a larger effective conjugation length for π -electrons along the backbone in the β -phase, resulting from a special conformation of the polymer backbone.¹⁰ Several processing conditions are known to favor induction of β -phase.^{9,11} Although a number of characteristic diffraction features have been identified for the β -phase in PF derivatives with linear side chains,¹² the structure of the β -phase has not yet been resolved and a detailed mechanistic understanding of its formation is still lacking.

6.2 Experimental section

The polymer used is *chiral* PF poly[9,9-bis((3*S*)-3,7-dimethyloctyl)-2,7-fluorene] (PF811, Figure 2, Chapter 1) with amino end-groups having $M_n = 20,400$ g/mol and $M_w = 37,600$ g/mol (PDI 1.84). The details regarding polymer synthesis can be found in Chapter 3. Stock solutions of PF811 were prepared by dissolving the polymer in 1-octanol at high temperatures.

CD and linear dichroism (LD) spectra were measured on a Jasco J-815 spectropolarimeter where the sensitivity, time constant, and scan rate were chosen appropriately. Temperature dependent measurements were performed with a PFD-425S/15 Peltier-type temperature controller with a temperature range of 263-383 K and a controlled cooling/heating rate. In these temperature dependent measurements, absorption can be measured simultaneously with the CD. The temperature corresponding to the onset of the CD effect, T_{aggr} , is defined as the temperature at which the CD signal rises above the noise level (≥ 2 mdeg). Unless stated otherwise, CD and absorption spectra pertain to an optical path length of 1 cm. UV-VIS absorption measurements at room temperature were done on a Perkin Elmer Lambda 900 UV/VIS/NIR spectrometer. Fluorescence measurements were performed on an Edinburgh Instruments FS920 double-monochromator luminescence spectrometer using a Peltier-cooled, red-sensitive photomultiplier. Scattering experiments were done using a Zetasizer Nano ZS, with 632 nm light and detection at an angle of 173° , in the temperature range 283-263 K. Equivalent hydrodynamic radii were determined by fitting the Siegert relation¹³ including a single exponential decay function to the experimental correlation function. From the decay constant ($\Gamma = Dq^2$) we estimate the hydrodynamic radius using the Stokes Einstein relation for a spherical particle.

6.3 Results and discussion

6.3.1 α and β -phase

To investigate the aggregation of the *chiral* polyfluorene PF811 in 1-octanol we use temperature and time dependent CD. PF811 is dissolved in 1-octanol by heating it to 90°C . At this temperature, the solutions show no significant CD effect (see Fig. 1), indicating that the polymer chains are present as free random coils. Upon cooling, the solubility of the rigid rod like polymer is lowered and chains aggregate. During controlled cooling of the hot solution containing 0.010 mg/ml of polymer at a rate of 10°C/h , we see the induction of a bisignate CD signal at temperatures $T < 50^\circ\text{C}$ see Fig. 1a. These CD features are associated with the electronic transition from the ground state to the lowest excited singlet state of the polymer (S_0 - S_1). The CD signal reaches a minimum at a wavelength of 350 nm and a maximum at 420 nm. We assign these features to a (semi-) crystalline state of the polymer: α -phase.

For a polymer concentration of 0.014 mg/ml, we find different CD features under the same conditions (Fig. 1b). At $-10\text{ }^{\circ}\text{C}$, the CD signal shows minima at 333 nm and 410 and a maximum at 430 nm. This indicates the formation of a different polymorph at high concentration. This polymorph is characterized by a long wavelength shoulder in the absorption spectrum near 425 nm (Fig. 2a). This shoulder is also observed for the β -phase in achiral polyfluorene. Upon excitation of this phase via the long wavelength transition with 425 nm light, we observe a structured fluorescence spectrum with rather narrow vibronic bands (Fig. 2b). The bands are red shifted with respect to those from the α -phase by about 20 nm. These features are indicative of a highly ordered β -phase. Upon heating, the long wavelength shoulder vanishes from the spectrum at $T = 70\text{ }^{\circ}\text{C}$ (Fig. 2c). This marks the melting temperature of the β -phase.

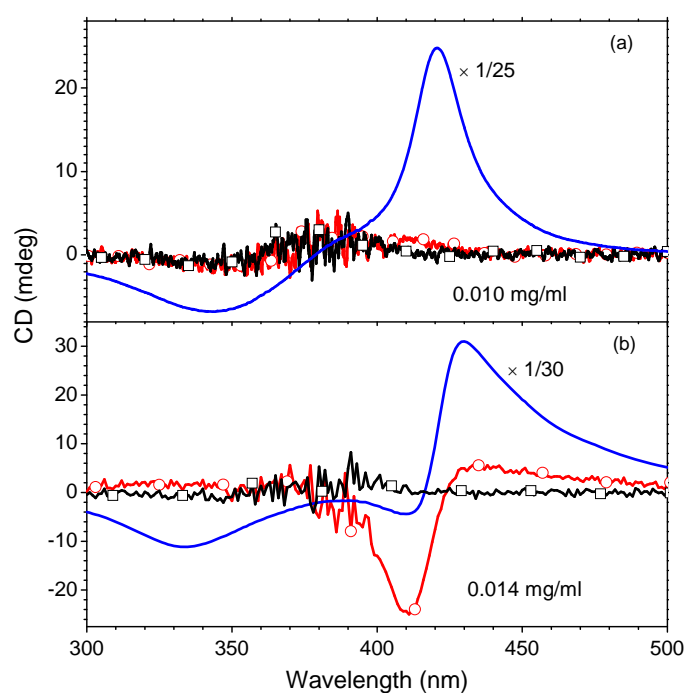


Figure 1: CD spectra of (PF811) chiral PF in 1-octanol at (a) 0.010 mg/ml and (b) 0.014 mg/ml concentration (bottom) at $T = 90\text{ }^{\circ}\text{C}$ ($-\square-$), $T = 50\text{ }^{\circ}\text{C}$ ($-o-$) and $T = -10\text{ }^{\circ}\text{C}$ ($—$) at a cooling rate of $10\text{ }^{\circ}\text{C}/\text{h}$.

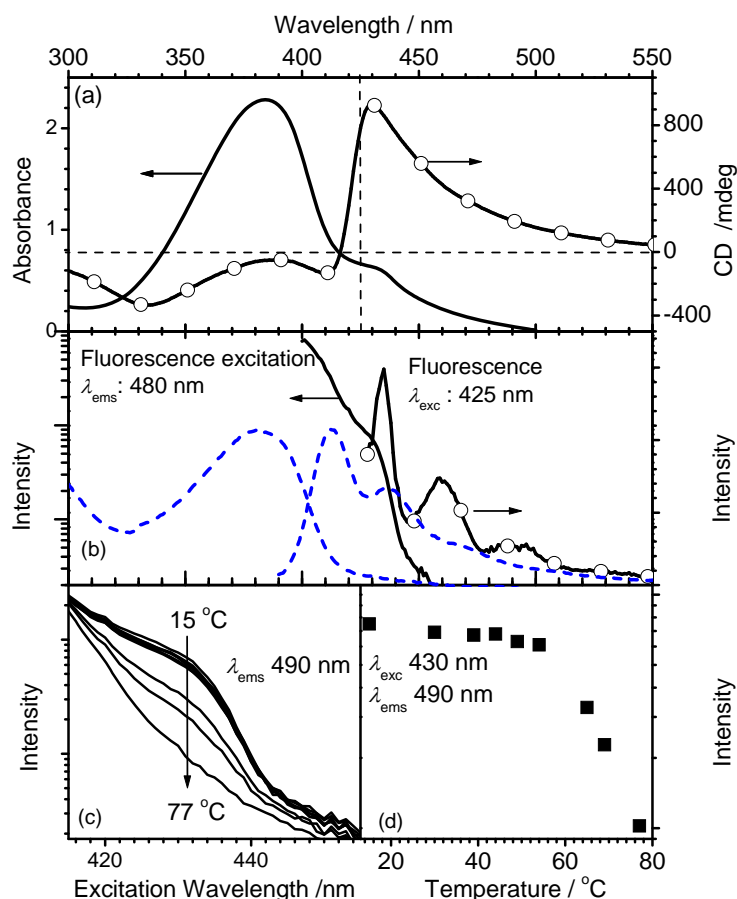


Figure 2: (a) Absorption and CD spectra for PF811 (0.014 mg/ml) in 1-octanol at room temperature. (b) Corresponding fluorescence and fluorescence excitation spectra. Wavelength of excitation: 425 nm and of emission detection: 480 nm. The blue dashed lines show absorption and fluorescence (excitation at 380 nm) for PF811 at 0.001 mg/ml (c) Temperature dependence of the long wavelength shoulder in the excitation spectrum of PF811 as shown in (b). Fluorescence monitored at 490 nm. (d) Corresponding fluorescence intensity upon excitation at 430 nm as a function of temperature.

An important question regarding the formation of the β -aggregates is whether this phase is actually ‘pure’ or whether it is a mixture of phases whose CD spectrum contains contributions from the various constituent types of aggregates. As mentioned before, the β -phase melts at a relatively high temperature (>70 °C) while the α -aggregates obtained at low concentration melt already below 60 °C. To investigate whether the so-called β -phase is actually a homogenous phase or a mixture, we have monitored the CD spectrum of a solution containing β -phase at low temperature (-10 °C) and also at a temperature just around the melting temperature (70 °C). These spectra are illustrated in Fig. 3. As can be seen the band shape of the CD spectrum at -10 °C and +70 °C are almost the same. In particular the ratio between the negative Cotton effect at 416 nm and the positive Cotton effect at 440 nm is virtually the same at the two temperatures. From this we conclude that there are no indications for the β -phase being mixtures of different types of aggregates with different melting temperatures.

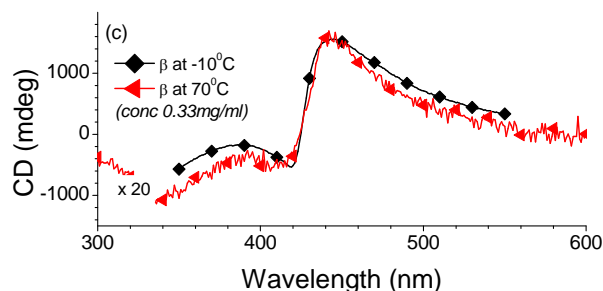


Figure 3: CD spectra of β aggregate at $-10\text{ }^{\circ}\text{C}$ and at $70\text{ }^{\circ}\text{C}$. The CD spectrum at $70\text{ }^{\circ}\text{C}$ is obtained by heating the solution of PF811 in 1-octanol (conc. 0.33 mg/ml) from $-10\text{ }^{\circ}\text{C}$ at a rate of $10\text{ }^{\circ}\text{C/h}$.

6.3.2 Precursor formation and stability

Interestingly, we find that the β -phase does not form in a single step from the molecularly dissolved state but involves a precursor. This precursor can be observed in the temperature dependent CD spectra while cooling to temperatures near $T = 50\text{ }^{\circ}\text{C}$, just before the onset of aggregation (Fig. 1b). The precursor is characterized by a CD band shape with a single minimum at 410 nm . Importantly, we find that in cooling experiments, the induction of the β -phase is invariably accompanied by the occurrence of the precursor in the early stages of aggregation. Under those conditions where the α -phase is formed, this precursor is not observed (Fig. 1a, 6 & 8).

The involvement of the precursor in the formation of the β -phase can be illustrated further by looking at the CD signal at 416 nm as a function of temperature (Fig. 4a). At low concentration (0.006 mg/ml) the CD signal measured at $T = 45\text{ }^{\circ}\text{C}$ is slightly positive, showing that the precursor does not form under these conditions. Upon further cooling we observe formation of α -phase with an onset of aggregation at $T_{\text{aggr}} = 40\text{ }^{\circ}\text{C}$. Upon further cooling to $-10\text{ }^{\circ}\text{C}$, and subsequent heating, this phase melts again around $50\text{ }^{\circ}\text{C}$. By contrast, at higher polymer concentration (0.014 mg/ml), the emergence of a negative Cotton effect for $T < 50\text{ }^{\circ}\text{C}$ indicates the formation of the precursor. Below $40\text{ }^{\circ}\text{C}$, the negative CD signature for the precursor signature gives way to the positive CD of the β -phase. Upon cooling to $-10\text{ }^{\circ}\text{C}$ and subsequent heating to $90\text{ }^{\circ}\text{C}$, we see that the β -phase melts around $70\text{ }^{\circ}\text{C}$. The large hysteresis indicates that the precursor structures assemble further in a cooperative manner forming the β -phase. Consistent with this, the precursor signature is not observed in the heating run of CD experiments. The CD band shape of the β -phase hardly changes upon heating to $70\text{ }^{\circ}\text{C}$, which indicates that this phase is homogeneous (Fig. 3). The intensity under the long wavelength shoulder at 425 nm that is the main characteristic of the β -phase, is only a fraction of the total intensity under the S_0 - S_1 absorption band near 390 nm . This low relative intensity, which is also observed for achiral polyfluorene,¹⁴ indicates that not all polymer chains in the β -phase may have a backbone conformation with extended conjugation causing the long wavelength absorption. This suggests that the β -phase accommodates different backbone conformations and may not be a ‘pure’ phase at the molecular level.

Time dependent CD measurements show that the precursor is stable in time at $T = 45^\circ\text{C}$ (Fig. 4c). At this temperature, the precursor is characterized by a monosignate CD spectrum (Fig. 4b). After rapid cooling ($> 600^\circ\text{C/h}$) of the solution containing the precursor from 45°C to -10°C , a CD spectrum results (Fig. 4d) that shows some similarity with that of the precursor but is markedly different from that of the β -phase (Fig. 1b). Thus formation of the β -phase from precursor is a time dependent phenomenon and may be interpreted in terms of cooperative aggregation of precursor structures. From the same solution, the α -phase is obtained when quenching directly from 90°C to -10°C .

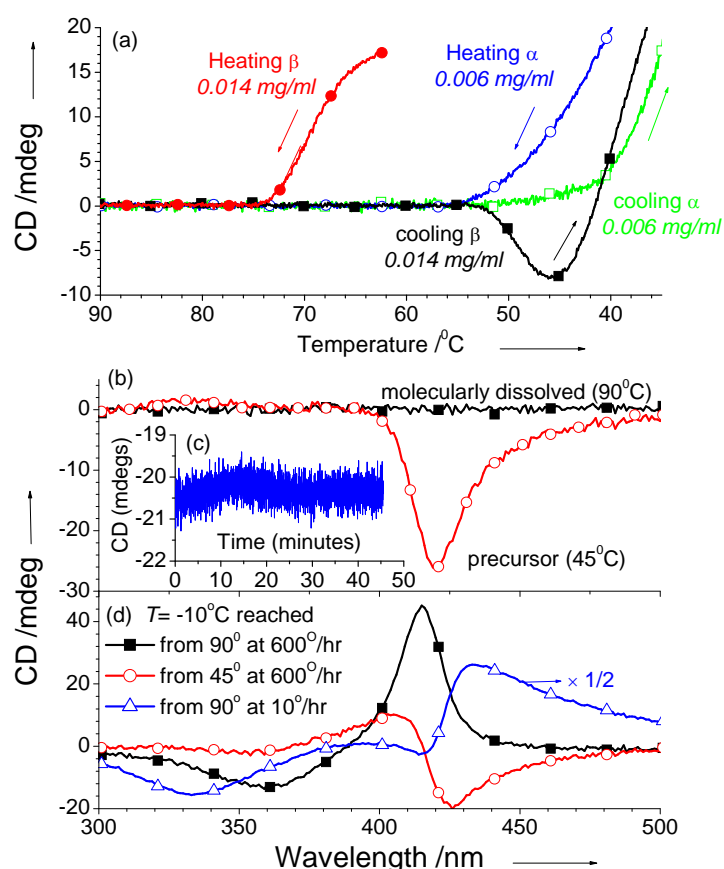


Figure 4: (a) CD of PF811 in 1-octanol monitored at 416 nm as a function of temperature upon cooling at 10°C/h from $T = 90^\circ\text{C}$ to -10°C . Data for two different concentrations: 0.006 mg/ml (open symbols) and 0.014 mg/ml (filled symbols). (b) CD spectra of PF811 at $T = 90^\circ\text{C}$ and 45°C (0.04 mg/ml , 1 mm optical path length, cooling from 90°C at 10°C/h). (c) Time evolution of the CD at 416 nm and 45°C . (d) CD spectra at -10°C upon rapid cooling ($> 600^\circ\text{C/h}$) the solutions shown in (b) from 90°C ($-\blacksquare-$) and from 45°C ($-o-$). Slow cooling from 90°C at 10°C/h ($-\triangle-$).

6.3.3 Dynamic light scattering on α and β -aggregates

Further evidence for the involvement of a precursor in the temperature induced aggregation of PF811 at slow cooling rates, comes from dynamic light scattering experiments. Figure 5 illustrates changes in light scattering upon cooling a solution of PF811 in 1-octanol (0.33 mg/ml) at fast (60°C/h) and slow (10°C/h) cooling rate. As can be seen in Fig. 5a, at slow

cooling rate, the scattered intensity rises above the base level at already a temperature of 64 °C, while at fast cooling rates the onset occurs at lower temperatures. Examining the intensity of scattered light in a broader temperature range (Fig. 5b), we observe a distinct shoulder in temperature range 64-55 °C upon slow cooling. This is consistent with a biphasic aggregation, involving a precursor. At fast cooling the shoulder is absent. Analysis of the autocorrelation function of the intensity of scattered light for slow cooling (Fig. 5c) confirms that in the temperature range 64-55 °C, small aggregates are formed that grow into larger ones at lower temperature. Taking into account the temperature dependent viscosity and refractive index of 1-octanol,¹⁵ we estimate an average equivalent hydrodynamic radius of the aggregates upon slow cooling of 1 and 2 × 10² nm at resp. 57.5 and 20 °C respectively. For fast cooling (Fig. 5d) the corresponding numbers are 0.6 and 1 × 10² nm. Here the lower value of the correlation function at 1 μs, shows that the intensity of light scattered by the aggregates is still comparable to the intensity of light scattered by the solvent.

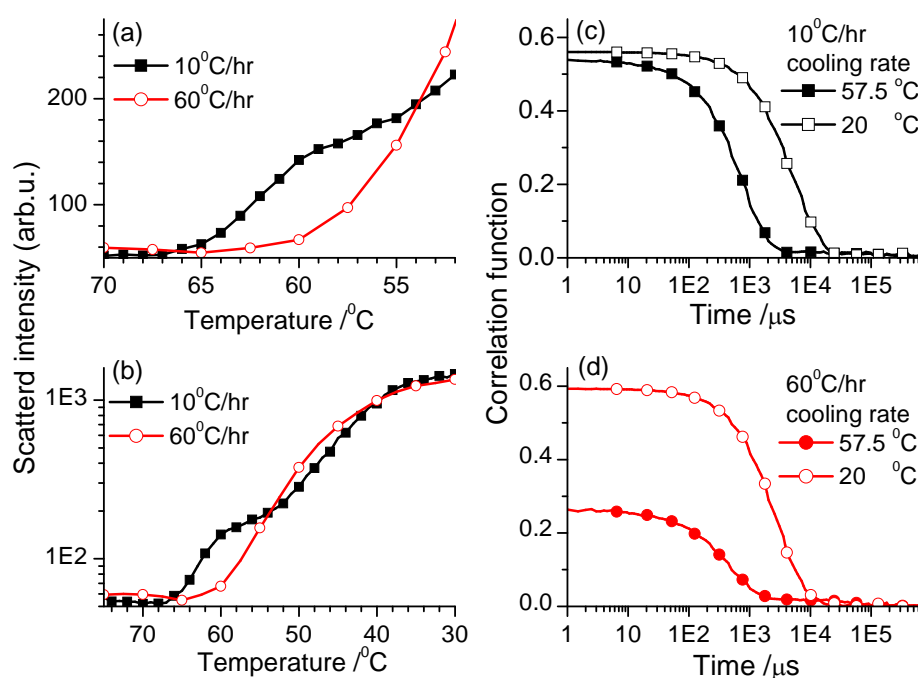


Figure 5: Dynamic light scattering measurements on a solution of PF811 in 1-octanol (0.33 mg/ml) upon cooling the solution down from 90 °C to room temperature at different cooling rates. a,b) intensity of scattered light for cooling rates of 10 °C/h (-■-) and 60 °C/h (-○-). c,d) Autocorrelation function for the fluctuating intensity of scattered light recorded at 57.5 and 20 °C for cooling rates of 10 °C/h (-■-, -□-, c) and 60 °C/h (-●-, -○-, d).

6.3.4 Role of concentration in existence of α and β -phases

Formation of the β -phase is found to be dependent on the concentration and cooling rate. It is found that at high concentrations (≥ 0.014 mg/ml) and slow cooling rates (≤ 10 °C/h), β -phase can be obtained. Failing of either of the above conditions yields α aggregates. In Fig. 6, we illustrate this concentration dependence further by showing the CD spectra for different

concentrations of PF811 in 1-octanol. Spectra were obtained by first heating the solutions to 90 °C and then cooling to -10 °C at a controlled rate of 10 °C/h. During this cooling, spectra were recorded at intervals of 10 °C. Spectra recorded at 90 °C, 50 °C and -10 °C are shown in Fig. 6. At 90 °C none of the solutions shows any significant CD effect, indicating that at this temperature all molecules are molecularly dissolved. Based on the CD features observed at 50 °C and -10 °C, we can now distinguish two different aggregation processes. One occurs at low, the second at high polymer concentrations.

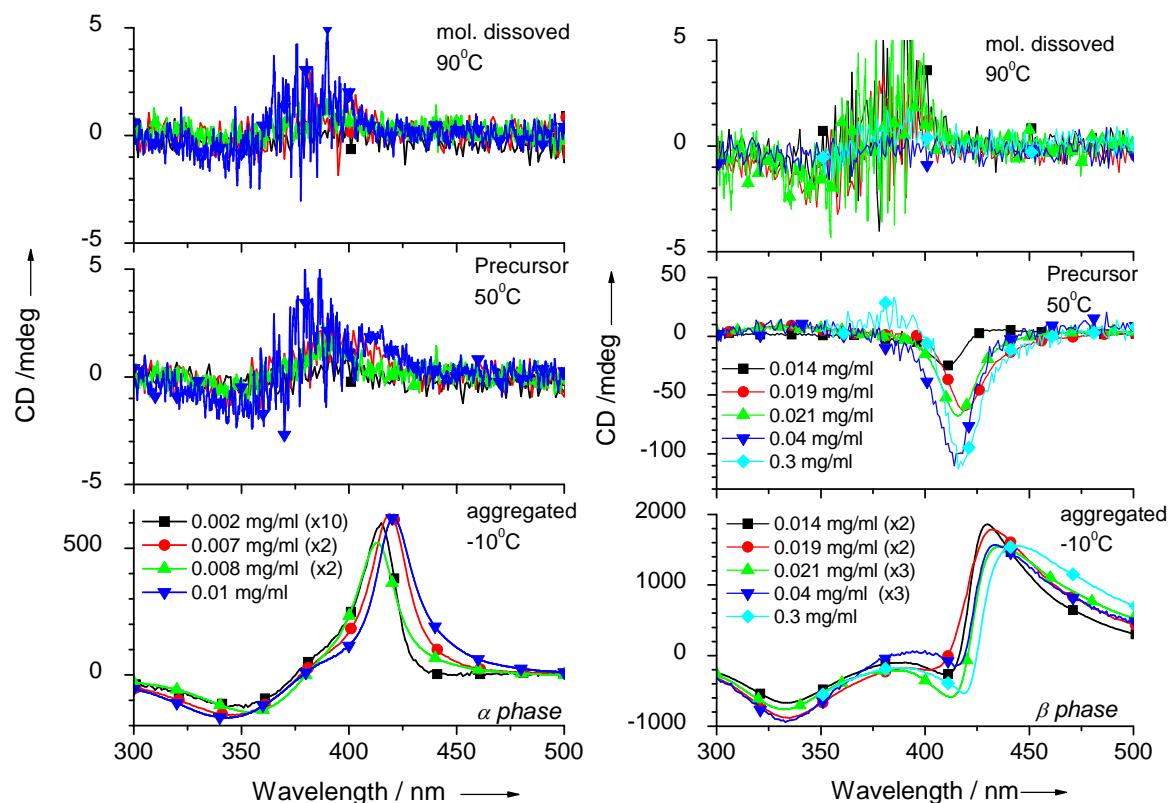


Figure 6: CD spectra at 90 °C (top), 50 °C (middle), and -10 °C (bottom) of solution of PF811 in 1-octanol at varying concentrations yielding different aggregates in α (left) and β (right) identifiable by different resultant CD spectra at -10 °C. The cooling rate in all cases is 10 °C/h. Solutions with polymer concentrations of 0.04 and 0.33 mg/ml were studied using an optical path length of 1 mm. Results shown were rescaled to an optical path length of 1cm by multiplication with a factor of 10.

The aggregation process for solutions with polymer concentration ≤ 0.01 mg/ml is characterized by the absence of any significant CD effect at 50 °C. Depending on the concentration, a significant CD effect sets in the temperature range 45 – 30 °C (Fig. 4). For this concentration range, CD spectra taken at -10 °C show a significant CD for wavelengths of around 345 nm where a negative extremum occurs. For wavelengths around 415 nm we observe a positive CD effect. These characteristics are taken to be indicative of α -aggregates.

For sample solutions with polymer concentration exceeding 0.01 mg/ml, a significant CD is already recorded at 50 °C. Here we observe a single negative CD effect featuring an extremum near wavelengths of 415 nm. Upon further cooling to -10 °C, the CD spectrum changes significantly and at -10 °C we observe minima with a net negative CD at 330 nm and

at 420 nm combined with a positive maximum in the CD around 435 nm. These features were assigned to β -phase. As can be seen from the collection of spectra in Fig. 6, in all cases where β type aggregation is observed at $-10\text{ }^{\circ}\text{C}$, we also observe a significant, monosignate CD effect at $50\text{ }^{\circ}\text{C}$, that is assigned to a precursor.

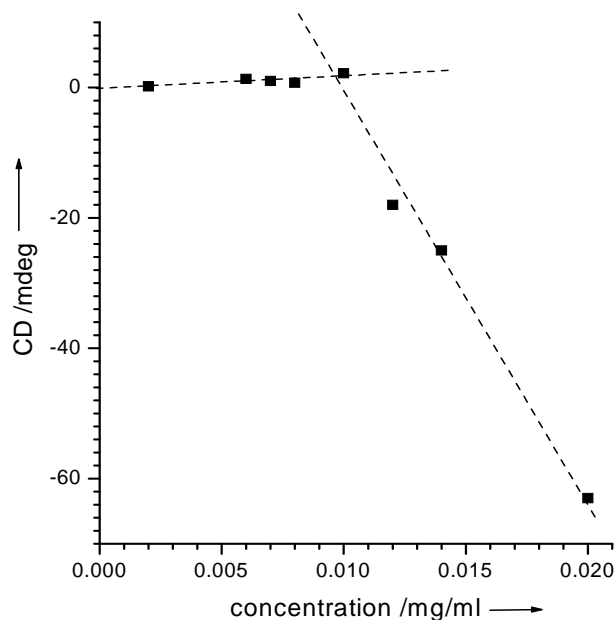


Figure 7: Variation in the CD intensity at 416 nm at $50\text{ }^{\circ}\text{C}$ upon slow cooling from $90\text{ }^{\circ}\text{C}$ ($10\text{ }^{\circ}\text{C}/\text{h}$) as a function of concentration. Data shown here are also shown in Fig. 4a, but here they are plotted on a linear concentration scale.

Here it is important to stress that the concentration dependence of the CD signal that we observe here is different from the trivial linear concentration dependence that one may expect for normal CD measurements on dissolved small molecules. As CD is in essence an absorption measurement, in case of non-interacting molecules one normally expects a linear variation in the CD intensity with concentration. The variation of CD amplitude that we observe for PF811 in 1-octanol is clearly different from linear, see Fig. 7. This is a direct indication for the involvement of intermolecular interactions in the formations of the chemical species that gives rise to the monosignate CD trace at $50\text{ }^{\circ}\text{C}$.

6.3.5 Role of cooling rate in existence of α and β -phases

Fig. 8 (a-c) shows the influence of the cooling rate upon formation of precursor and β -aggregate for three different concentrations. It can be seen that at low concentration (0.006 mg/ml) irrespective of the cooling rate, α aggregate formation predominates. At higher concentrations β -aggregate formation is also observed for cooling rates rate of $30\text{ }^{\circ}\text{C}$ and higher. However for cooling rates of $10\text{ }^{\circ}\text{C}/\text{h}$ and concentrations $> 0.01\text{ mg/ml}$, formation of β -aggregates is observed (Fig. 8 b, c).

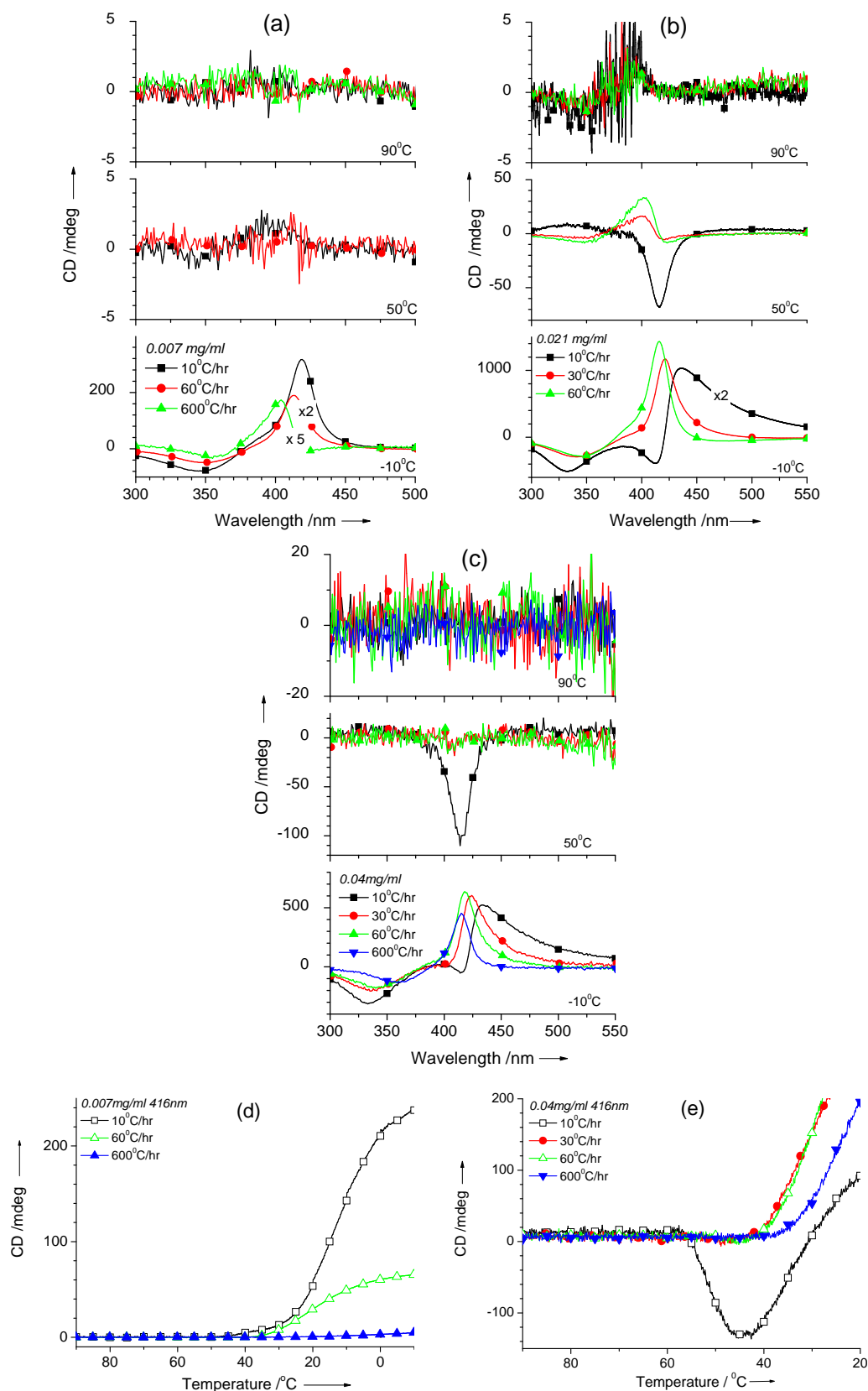


Figure 8: CD spectra at 90 °C (top), 50 °C (middle), and -10 °C (bottom) of solution of PF811 in 1-octanol at different cooling rates with respect to varying concentrations: (a) 0.007 mg/ml, (b) 0.021 mg/ml, and (c) 0.04 mg/ml. Cooling curves of solution of PF811 in 1-octanol at (d) 0.007 mg/ml and (e) 0.04 mg/ml with respect to varying cooling rates. All measurements were monitored at 416 nm wavelength.

Fig. 8 (d-e) shows the CD monitored at 416 nm for different cooling rates and for two concentrations of polymer. At low concentration we only observe positive CD signal which we attribute to formation of α -aggregates. At very high cooling rates the CD amplitude is much smaller than after slow cooling. We interpret this by assuming formation of aggregates with an amorphous structure upon very rapid cooling. At high concentration (0.04 mg/ml) and slow cooling rate of 10 °C/h we observe negative CD in the temperature range 55 – 30 °C that may be attributed to precursor formation. At higher cooling rates the negative CD effects are not observed indicating that precursor formation is a time dependent process.

6.3.6 Temperature dependent LD in α and β -phases

CD spectra can contain artificial contributions which do not have their origin in chirality at the (supra-) molecular level.¹⁶ Especially when the sample under study shows significant linear dichroism (LD), CD measurements are prone to such errors. Large LD may occur when studying large aggregates.¹⁷ For the aggregation of PF811, LD has been measured in separate experiments, at different concentrations and cooling rates (Fig. 9). We find that LD signals are relatively small. Furthermore, no significant changes in the LD signal are observed in the temperature range where the aggregation sets in and where the CD signal rises from zero (T_{aggr}). In Fig. 9a, the onset of aggregation is marked by the rise of the absorption signal. We therefore conclude that there are no indications for large artificial contributions to the measured CD signal related to LD.

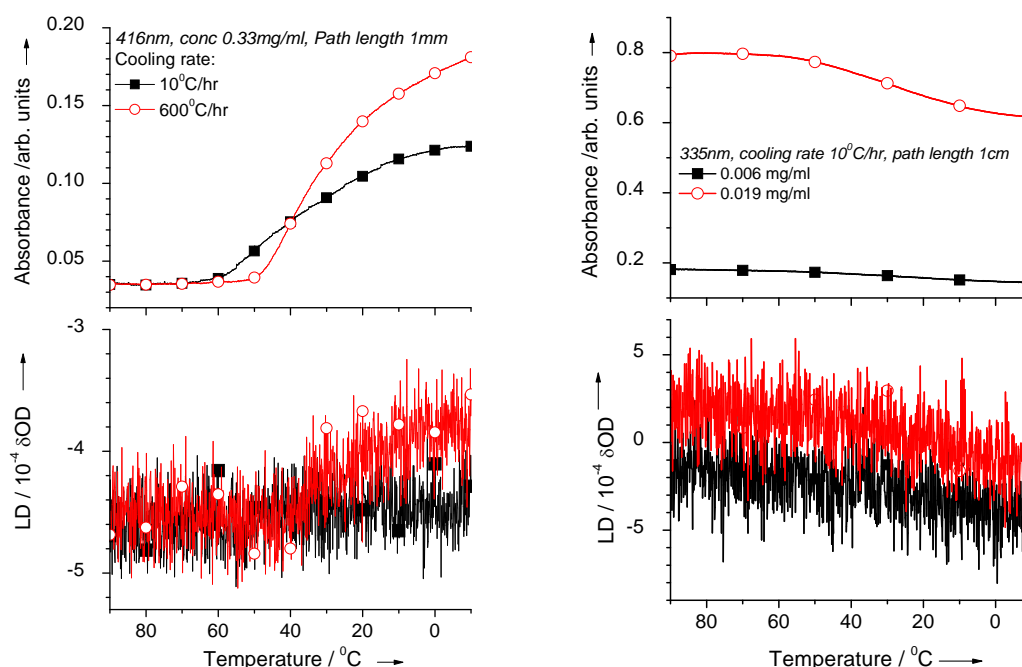


Figure 9: (Left) Absorbance and Linear Dichroism (LD) of solutions of PF811 in 1-octanol (0.33 mg/ml, 1 mm path length) recorded at 416 nm for two different cooling rates (10 °C/h and 600 °C/h). (Right) Corresponding results for different concentrations (0.006 and 0.019 mg/ml, 1 cm path length, wavelength 416 nm, fixed cooling rate of 10 °C/h).

6.3.7 Phase diagram

The magnitude of the CD effect after cooling to 50 °C as a function of concentration is shown in Fig. 11. For concentrations below 0.01 mg/ml, the CD effect is negligible. For concentrations exceeding 0.01 mg/ml, we observe negative CD, marking the formation of the precursor. This non-linear dependence of the negative CD effect from the precursor on concentration, shows that precursor formation involves intermolecular interactions between several polymer chains coming together to form the precursor. This is reminiscent of the formation of the triple helix from collagen mimicking peptides.¹⁸

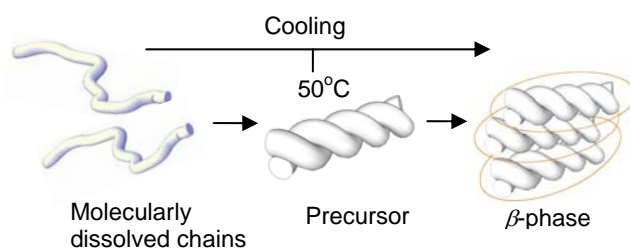


Figure 10: Schematic illustration of the formation of β -phase via precursor.

The monosignate CD band shape of the precursor may be explained by a helical conformation of the backbone of the polyfluorene.^{19,20} Diffraction studies²¹ and molecular modeling^{6,22} on achiral polyfluorene have indicated that helical conformations approximately described by 5_1 (or 5_2) are particularly stable. For the β -phase, helices close to 2_1 have been proposed.¹⁰ The absence of the bisignate CD band shape expected for exciton coupling between chains held in a chiral arrangement²³ can only be explained assuming that, the polyfluorene chains are oriented in the same direction in the precursor. A possible structural model for the precursor could be intertwined helices as shown in Figure 10. Molecular modeling studies on chiral oligofluorene indicate the possibility of such intertwined helices.²⁴

At cooling rates exceeding 10 °C/h, the precursor (and β -phase) is not formed (Figure 8). This indicates that formation of precursor is an intrinsically slow process, involving e.g. concerted folding of long random coils (Figure 10). The dependence of β -phase formation is further illustrated in Fig. 11b. Here the temperature at which the CD sets is plotted as a function of concentration upon cooling. The character of the aggregates obtained at -10 °C (α/β) is illustrated by the different symbols. As can be seen, the β -phase is obtained for concentrations > 0.01 mg/ml. This demarcation between α/β formation coincides with the onset concentration for formation of precursor. Formation of the β -phase can also be inhibited by increasing the rate of cooling. For cooling rates of 30 °C/h and higher, the α -phase is obtained instead of the β -phase. These data points can also be represented in a different way where the type of aggregate obtained is plotted as a function of cooling rate and concentration. Fig. 12 shows such a kinetic phase diagram.

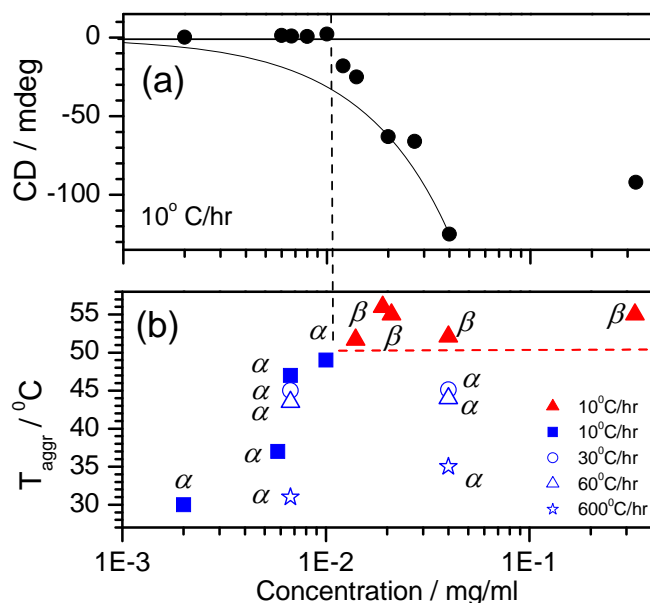


Figure 11: (a) Maximum precursor CD observed at 50 °C in the neighborhood of 416 nm for different concentrations upon cooling from $T = 90$ °C at a rate of 10 °C/h. The curved solid line illustrates a linear relation between CD and concentration. b) Temperature at which the CD signal at 416 nm sets in and nature of the CD band shape (α/β , see text) upon further cooling to -10 °C at 10 °C/h (filled symbols). Open symbols: corresponding data for faster cooling rates.

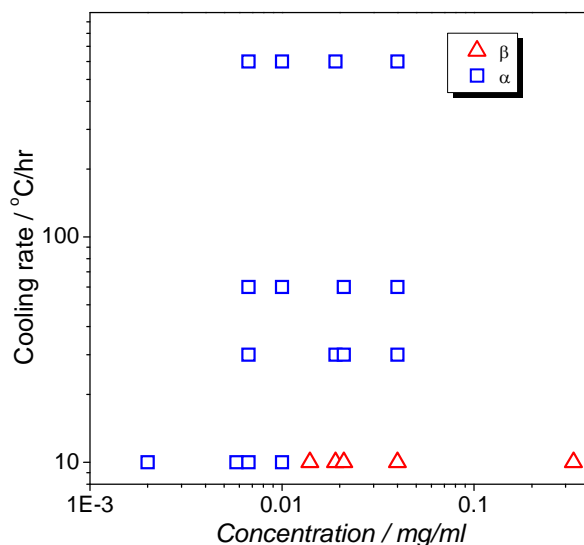


Figure 12: Kinetic phase diagram for formation of α and β aggregates.

6.4 Conclusion

In summary, we have shown that a particular polymorph (β) of chiral polyfluorene exists, whose formation involves a meta-stable, precursor. Due to the fact that formation of the other polymorph (α) does apparently not proceed via this precursor, one can promote β -phase formation by choosing those processing conditions that favor precursor formation.

References

1. (a) Keller, A.; Cheng, S.Z.D. *Polymer* **1998**, *39*, 4461. (b) Sirota, E. B.; Herhold, A. B. *Science* **1999**, *283*, 529.
2. (a) Schaper, A.; Georgalis, Y.; Umbach, P.; Raptis, J.; Saenger, W. *J. Chem. Phys.* **1997**, *106*, 8587. (b) Allegra, G.; Meille, S.V. *Adv. Polym. Sci.* **2005**, *191*, 87.
3. (a) Häfele, A.; Heck, B.; Kawai, T.; Kohn, P.; Strobl, G. *Eur. Phys. J. E* **2005**, *16*, 207. (b) Yang, L.; Somani, R.H.; Sics, I.; Hsiao, B.S.; Kolb, R.; Lohse, D. *J. Phys. Condens. Matter* **2006**, *18*, S2421. (c) Somani, R.H.; Yang, L.; Hsiao, B. S. *Physica A* **2002**, *304*, 145. (d) Horn, D.; Rieger J. *Angew. Chem. Int. Ed.* **2001**, *40*, 4330.
4. Balzano, L.; Kukalyekar, N.; Rastogi, S.; Peters, G.W.M.; Chadwick, J.C. *Phys. Rev. Lett.* **2008**, *100*, 048302.
5. (a) McCulloch, I.; Heeney, M.; Bailey, C.; Genevicius, K.; Macdonald, I.; Shkunov, M.; Sparrowe, D.; Tierney, S.; Wagner, R.; Zhang, W.M.; Chabinyk, M.L.; Kline, R.J.; McGehee, M.D.; Toney, M.F. *Nat. Mater.* **2006**, *5*, 328. (b) B.J. Schwartz, *Ann. Rev. Phys. Chem.* **2003**, *54*, 141. (c) Hoeben, F.J.M.; Jonkheijm, P.; Meijer, E.W.; Schenning, A.P.H.J. *Chem. Rev.* **2005**, *105*, 1491.
6. Wu, L.; Sato, T.; Tang, H.-Z.; Fujiki, M. *Macromolecules* **2004**, *37*, 6183.
7. (a) Abbel, R.; Schenning, A.P.H.J.; Meijer, E.W. *Macromolecules* **2008**, *41*, 7497. (b) Oda, M.; Nothofer, H.-G.; Lieser, G.; Scherf, U.; Meskers, S.C.J.; Neher, D. *Adv. Mater.* **2000**, *12*, 362.
8. (a) Grimsdale, A.C.; Müllen, K. *Adv. Polym. Sci.* **2008**, *212*, 1-48. (b) Knaapila, M.; Winokur, M.J. *Adv. Polym. Sci.* **2008**, *212*, 227. (c) Scherf, U.; List, E. *Adv. Mater.* **2002**, *14*, 477. (d) Neher, D. *Macromol. Rapid. Commun.* **2001**, *22*, 1365. (e) Grell, M.; Bradley, D.D.C.; Inbasekaran, M.; Woo, E.P. *Adv. Mater.* **1997**, *9*, 798. (f) Monkman, A.P.; Rothe, C.; King, S.; Dias F. *Adv. Polym. Sci.* **2008**, *212*, 187.
9. (a) Grell, M.; Bradley, D.D.C.; Ungar, G.; Hill, J.; Whitehead, K.S. *Macromolecules* **1999**, *32*, 5810. (b) Chen, S.H.; Su, A.C.; Chen, S.A. *J. Phys. Chem. B* **2005**, *109*, 10067. (c) Dias, F.B.; Morgado, J.; Macanita, A.L.; Da Costa, F.P.; Burrows, H.D.; Monkman, A.P. *Macromolecules* **2006**, *39*, 5854.
10. Chunwaschirasiri, W.; Tanto, B.; Huber, D.L.; Winokur, M.J. *Phys. Rev. Lett.* **2005**, *94*, 107402.
11. (a) Peet, J.; Brocker, E.; Xu, Y.; Bazan, G.C. *Adv. Mater.* **2008**, *20*, 1882. (b) O'Carroll, D.; Iacopino, D.; O'Riordan, A.; Lovera, P.; O'Connor, É.; O'Brien, G. A.; Redmond, G. *Adv. Mater.* **2008**, *20*, 42.
12. Chen, S.H.; Su, A.C.; Su, C.H.; Chen, S.A. *J. Phys. Chem. B* **2006**, *110*, 4007.
13. Wu, C.; Wu, B. in *Experimental methods in polymer science*, Tanaka T. Ed., Academic Press, San Diego, **1998**.
14. Bright, D.W.; Dias, F.B.; Galbrecht, F.; Scherf, U.; Monkman, A.P.; *Adv. Func. Mater.* **2009**, *19*, 67.
15. Paolantoni, M.; Sassi, P.; Morresi, A.; Cataliotti, R.S. *Mol. Phys.* **2001**, *99*, 1493.
16. (a) Schellman, J.; Jensen H. P. *Chem. Rev.*, **1987**, *87*, 1359. (b) Nordén, B. *J. Phys. Chem.* **1978**, *82*, 744. (c) Davidsson, N.; Nordén, B.; Seth, S. *Chem. Phys. Lett.* **1980**, *70*, 313. (d) Shindo, Y.; Nishio, M.; Maeda, S. *Biopolymers* **1990**, *30*, 405. (e) Kuroda, R.; Harada, T.; Shindo, Y. *Rev. Sci. Instrum.* **2001**, *72*, 3802.
17. Tsuda, A.; Alam, A. Md.; Harada, T.; Yamaguchi, T.; Ishii, N.; Aida, T. *Angew. Chem. Int. Ed.* **2007**, *46*, 8198.
18. Engel, J.; Bächinger, H. P. *Top. Curr. Chem.* **2005**, *247*, 7.
19. Tang, H.Z.; Fujiki, M.; Sato T. *Macromolecules* **2002**, *35*, 6439.
20. (a) Percec, V.; Aqad, E.; Peterca, M.; Rudick, J.G.; Lemon, L.; Ronda, J.C.; De, B.B.; Heiney, P.A.; Meijer, E.W. *J. Am. Chem. Soc.* **2006**, *128*, 16365. (b) Ciardelli, F.; Lanzillo, S.; Pieroni, O. *Macromolecules* **1974**, *7*, 174.
21. (a) Knaapila, M.; Torkelli, M.; Monkman, A.P. *Macromolecules* **2007**, *40*, 3610. (b) Knaapila, M.; Stepanyan, R.; Lyons, B.P.; Torkkeli, M.; Monkman, A.P. *Adv. Func. Mater.* **2006**, *16*, 599.
22. (a) Marcon, V.; van der Vegt, N.; Wegner, G.; Raos G. *J. Phys. Chem. B* **2006**, *110*, 5253. (b) Oda, M.; Nothofer, H.-G.; Scherf, U.; Sunjic, V.; Richter, D.; Regenstein, W.; Neher, D. *Macromolecules* **2002**, *35*, 6792.

23. Berova, N.; Nakanishi, K.; Woody R.W. *Circular Dichroism: Principles and Applications*. Wiley-VCH, Weinheim, **2000**.
24. Geng, Y.; Trajkovska, A.; Katsis, D.; Ou, J.J.; Culligan, S.W. ; Chen, S.H. *J. Am. Chem. Soc.* **2002** *124*, 8337.

Anisotropic dielectric tensor for *chiral* polyfluorene at optical frequencies

Abstract. The anisotropic dielectric tensor of *chiral* polyfluorene is determined *via* variable angle spectroscopic ellipsometry and circular dichroism spectroscopy. The anisotropy was found to be influenced by high in-plane alignment of polymer chains in the thin film. Chirality of the polymer results in small but non-zero off-diagonal matrix elements in the dielectric tensor. Consequences for these off-diagonal terms in the reflection of light are discussed. Subsequently, optical rotation and ellipticity in reflection are predicted for pristine film of chiral polyfluorene.

7.1 Introduction

Conjugated polymers such as polyfluorene and its derivatives can be applied as thin layers in a variety of optical¹ and optoelectronic devices.² To understand and describe device performance and phenomena, knowledge of the optical properties is of importance. The response of any material to alternating electromagnetic fields like light can be described by the frequency dependent dielectric constant $\varepsilon(\omega) = \varepsilon_1(\omega) + i\varepsilon_2(\omega)$, where ε_1 and ε_2 are the real and imaginary parts, and ω is the angular frequency of the wave. Optical properties such as the complex refractive index $\tilde{n}(\omega) = n(\omega) + i\kappa(\omega)$, in which n is the index of refraction and κ the extinction index, are directly related to the dielectric constant *via* $\tilde{n}^2 = \varepsilon$.

Spin coated films of polyfluorene and other conjugated polymers often exhibit anisotropy.³⁻⁷ This phenomenon can be related to the alignment of chains at a macroscopic level during the deposition process. Alignment of chains has been supported by X-ray diffraction in some cases.⁸ Polyfluorenes have a rigid rod like character and also display anisotropy in their optical properties at the molecular level. For instance, the transition dipole moment associated with the lowest optical transition is oriented along the chain direction. The combination of preferential alignment of the chains and the directionality of the molecular optical transitions results in anisotropic optical properties of the film.

Spectroscopic ellipsometry can be employed to determine anisotropic optical constants in thin films of polyfluorene.⁹⁻¹² Knowledge of this optical anisotropy is important for modeling the performance of optoelectronic devices. For polymer photovoltaic cells, absorbance of sunlight may be increased by aligning the polymer chains in the plane of the film.¹³ Likewise, out-coupling of light out of a polymer light emitting diode is influenced by the anisotropy.¹⁴ The optical anisotropy can be uniaxial or biaxial in nature. For the latter, the refractive index in all three directions is different whereas in the former, two are identical.

For uniaxial anisotropy the frequency dependent dielectric tensor can be represented as:

$$\frac{\varepsilon(\omega)}{\varepsilon_0} = \begin{bmatrix} \varepsilon_{\perp}(\omega) & 0 & 0 \\ 0 & \varepsilon_{\perp}(\omega) & 0 \\ 0 & 0 & \varepsilon_{\parallel}(\omega) \end{bmatrix} \quad (1)$$

where ε_{\perp} and ε_{\parallel} are the perpendicular and parallel components of the dielectric constant of the medium and ε_0 is the vacuum permittivity. The dielectric tensor describes the polarization of the material under the influence of the applied field \mathbf{E}_0 . Often it is assumed that the polarization $\mathbf{P}(\mathbf{r})$ at the position \mathbf{r} depends only on the value of the externally applied field at position \mathbf{r} (dipole approximation). However, this is not necessarily true and the polarization may also depend in a non-local manner on the applied field. The non-locality of the response, often also referred to as *spatial dispersion*, can be incorporated into the dielectric function by including a dependence on the wavevector \mathbf{k} of the light. In a series expansion one can write:¹⁵

$$\varepsilon(\omega, \mathbf{k}) = \varepsilon(\omega) + i\gamma\mathbf{k} + \alpha\mathbf{k}\mathbf{k} + \dots \quad (2)$$

where γ is a material's constant and \mathbf{k} is the wavevector ($= \omega n/c$, with n the refractive index). For centrosymmetric materials, $\varepsilon(\omega, \mathbf{k})$ should remain unchanged under the inversion symmetry operation. This excludes a contribution from the term $i\gamma\mathbf{k}$. This is because the wavevector \mathbf{k} changes sign under inversion while γ remains unaltered so that the contribution described by the term $i\gamma\mathbf{k}$ changes sign under inversion, which is not compatible with the supposed symmetry of the material. Hence for centrosymmetric materials $\gamma = 0$ and the first \mathbf{k} dependent term in eq. 2 is quadratic. Here we assume that all quadratic terms are negligible.

For chiral, *i.e.* non-centrosymmetric, materials γ can have non zero values. The material constant γ describes the natural optical activity of a material. Far away from any optical resonance, the value of γ relates to the magnitude of the optical rotation. The dielectric tensor for non-centrosymmetric materials can now be written as:

$$\frac{\varepsilon(\omega)}{\varepsilon_0} = \begin{bmatrix} \varepsilon_{\perp}(\omega) & 0 & 0 \\ 0 & \varepsilon_{\perp}(\omega) & 0 \\ 0 & 0 & \varepsilon_{\parallel}(\omega) \end{bmatrix} + i \begin{bmatrix} 0 & -G_{12}(\omega) & -G_{13}(\omega) \\ G_{12}(\omega) & 0 & -G_{23}(\omega) \\ G_{13}(\omega) & G_{23}(\omega) & 0 \end{bmatrix} \quad (3)$$

where the second term on the right hand side, $G = \gamma\mathbf{k}$ is a pseudo tensor that changes its sign upon the inversion symmetry operation.

In case of a uniaxial material, a light wave propagating along the optical axis (z) through a dielectric material obeys the following wave equation:

$$\begin{bmatrix} \frac{\partial^2}{\partial x^2} & 0 \\ 0 & \frac{\partial^2}{\partial y^2} \end{bmatrix} \begin{bmatrix} E_x \\ E_y \end{bmatrix} = \frac{1}{c^2} \begin{bmatrix} \varepsilon_{\perp} & -iG_{12} \\ iG_{12} & \varepsilon_{\perp} \end{bmatrix} \begin{bmatrix} E_x \\ E_y \end{bmatrix} \quad (4)$$

The two eigen polarizations of the medium, *i.e.* the two polarizations that travel through the medium without changing, can be obtained from diagonalizing the relevant part of the dielectric tensor.

$$\det \begin{bmatrix} \varepsilon_{\perp} - \lambda & -iG_{12} \\ iG_{12} & \varepsilon_{\perp} - \lambda \end{bmatrix} = 0 \quad (5)$$

Here because of the symmetry of the matrix, the eigen polarizations are purely circular. The non-zero value of G_{12} describes the difference of the material in its response to left and right circular polarized light incident along the optical axis. The eigen values correspond to the

scalar values of the dielectric constant for the left and right circular polarized eigen polarizations

$$\lambda_{\pm} = \lambda_{L/R} = \varepsilon_{L/R} = \varepsilon_{\perp} \pm G_{12} \quad (6)$$

The refractive index for the two eigen polarizations can be obtained by taking the square root of dielectric constants using Maclaurin series and neglecting high order terms in G_{12} .

$$\tilde{n}_{L/R} = \sqrt{\varepsilon_{L/R}} \cong \sqrt{\varepsilon_{\perp}} \pm \frac{G_{12}}{2} = \tilde{n}_{\perp} \pm \frac{G_{12}}{2} \quad (7)$$

The real and imaginary parts of these refractive indices $\tilde{n}_{L/R} = n_{L/R} + i\kappa_{L/R}$ can now be expressed in terms of n_{\perp} and the complex pseudo tensor $G_{12} = G_{12}' + i G_{12}''$

$$\kappa_{L/R} = \kappa_{\perp} \pm \frac{G_{12}''}{2} \quad (8)$$

$$n_{L/R} = n_{\perp} \pm \frac{G_{12}'}{2} \quad (9)$$

In this study we determine the anisotropic dielectric tensor including terms of first order in \mathbf{k} for films of a chiral polyfluorene poly[9,9-bis((3*S*)-3,7-dimethyloctyl)-2,7-fluorene] (PF811). The main motivation for this is the following. Reflection of light by dielectric materials is of major practical importance and very well studied. Yet reflection of light by chiral materials is not well understood. There are reports claiming the existence of optical activity in reflection of light incident along the surface normal, *i.e.* differences in the reflection of left and right circular polarized light incoming along the normal to the surface of the dielectric.¹⁶ Other studies have denied the existence of such effects for homogeneous materials for light incident along the normal.^{17,18} Here it is important to realize that for chiral organic and polymeric materials hardly any data for the dielectric tensor exist. In order to make progress in solving this controversial issue of optical activity in reflection, it is of importance to determine the dielectric tensors to come to a quantitative evaluation of various theoretical predictions.

Here we focus on unannealed films of chiral PF811. Earlier in Chapter 3 we have shown that this material shows intensive chiroptical properties which allow a description using eq. 3. This relation holds for homogeneous materials, showing intensive optical properties. For unannealed films of chiral polyfluorene PF811 the chiroptical properties arise on a very short length scale much smaller than the wavelength of light. In contrast, for cholesteric liquid crystals, the chiroptical properties arise from long range molecular order. Here the variation for the dielectric constants in space needs to be taken into account in an explicit way.¹⁹

In order to determine the dielectric tensor for films of the chiral polyfluorene, we use a combination of techniques: spectroscopic ellipsometry and circular dichroism. The latter

technique is used to determine the pseudo tensorial part G of $\epsilon(\omega, \mathbf{k})$, while we use the ellipsometry to determine $\epsilon(\omega)$. This particular approach is necessary because there are no procedures known to determine G directly from reflection based measurements such as ellipsometry. This is related to the controversiality of the optical activity in reflection. The fact that components of G turn out to be much smaller in magnitude than those of $\epsilon(\omega)$ may be put forward to justify the approach taken. Finally both the chirality dependent terms and the anisotropy of the dielectric response of the film of chiral polyfluorene PF811 will be interpreted in terms of the molecular orientation and organization in the film.

7.2 Experimental and modeling section

7.2.1 Film preparation and instrumentation

Chiral polyfluorene poly[9,9-bis((3*S*)-3,7-dimethyloctyl)-2,7-fluorene] (PF811, Figure 2, Chapter 1) films were prepared by spin coating the chloroform solution (conc. 10 mg/ml) on silicon (Si) wafers (with a similar copy on glass substrates) at a spin rate of 1500 rpm. The details regarding polymer synthesis can be found in Chapter 3. The films obtained were homogeneous in nature with a thickness approximately 65 nm as recorded using a Veeco surface profilometer. By varying the spin rate, films of varying thickness were obtained. For achiral polyfluorene poly[9,9-di-*n*-octyl-2,7-fluorene] (PFO, Figure 8c), an 80 nm thick film was prepared by spin coating from a 12 mg/ml chlorobenzene solution. The achiral polyfluorene (ADS129BE, American Dye Source, Inc.) used here has $M_w = 42000$ g/mol. Ellipsometric experiments were done on Woollam WVASE32 (J. A. Woollam Co., Inc) ellipsometer. UV-VIS measurements were done on a Perkin Elmer Lambda 900 UV/VIS/NIR spectrometer. CD spectra were measured on a Jasco J-815 spectropolarimeter where the sensitivity, and scan rate were chosen appropriately.

7.2.2 Ellipsometry experiments and modeling

The ellipsometer yields ψ and Δ values, which are measure of attenuation of reflected light intensity and the corresponding phase angle upon reflection. Data acquisition for ψ and Δ values is done for a wide range of incident angles in and around Brewster angle of the material. To obtain the optical constants n and κ , a model is used starting with an approximate input solution to the experimental data. The model contains mathematical descriptions of the complex dielectric constant of the various layers and information on the thickness and roughness of each individual layer in a stack. Using the Levenberg-Marquardt algorithm, a curve is then fitted to the experimental ψ and Δ values. To obtain an optimum solution, several iterations are performed over the various fitting parameters in order to minimize the difference between experimental and modeled parameters. The fitting parameters are the thickness of the layers and the parameters that describe the complex dielectric function in terms of dispersion equations and oscillators.

One of the basic equations involved in explaining the refractive index of the material is the Cauchy equation:

$$n(\lambda) = A + \frac{B}{\lambda^2} + \frac{C}{\lambda^4} + \dots \quad (10)$$

where A , B , and C are coefficients, with A a dimensionless quantity and λ the wavelength of incident light ($\lambda = 2\pi c/\omega$). This equation considers that the refractive index is wavelength dependent, common to most transparent materials (*i.e.*, $\kappa = 0$). For absorbing materials (*i.e.*, $\kappa \neq 0$) the general oscillator model is commonly used to mimic the dielectric constants. This model involves oscillators such as Gaussian (ε^G), or Lorentzian (ε^L) functions to mimic optical transitions of the material. The real part of the permittivity, ε_1 , which is related to the stored energy within the medium, can be calculated from a Kramers-Kronig transformation of the imaginary part of the permittivity, ε_2 , which is related to the dissipation of energy within the medium. The Lorentzian and Gaussian oscillators as function of the photon energy $E (= hc/\lambda)$ are given by:

$$\tilde{\varepsilon}^L = \varepsilon_1(\infty) + \frac{AE_c}{E_c^2 - E^2 - iBE} \quad (11)$$

$$\varepsilon_2^G(E) = \frac{A}{B} \left[\exp\left[-\left(\frac{E-E_c}{\sigma}\right)^2\right] - \exp\left[-\left(\frac{E+E_c}{\sigma}\right)^2\right] \right]$$

$$\varepsilon_1^G(E) = \frac{2}{\pi} \cdot P \int_0^\infty \frac{\xi \varepsilon_2(\xi)}{\xi^2 - E^2} d\xi \quad (12)$$

$$\sigma = \frac{B}{2\sqrt{\ln 2}};$$

where A is the amplitude, B is energy bandwidth at half maximum, and E_c is the resonance energy. Here, all three parameters A , B , and E_c are in energy units. The $\varepsilon_1(\infty)$ is the offset term attached to the real part of the dielectric constants in order to prevent it from converging to zero for energies below the band gap. It should be noted that though A is called the amplitude, it is more technically referred to the area under the absorbance peak.²⁴ P stands for the Cauchy principal part of the integral.²⁰ However, the aforementioned oscillators are symmetric in nature, while real absorbance spectra are often asymmetric and exhibit a steep onset. To describe these asymmetrical band shapes several other oscillators such a Cody-Lorentz (ε^{CL})^{21,22} and Tauc-Lorentz (ε^{TL})²³ are often useful.

$$\varepsilon_2^{\text{TL}} = \begin{cases} G_{\text{T}}(E)L(E) = \frac{AE_c B(E - E_g)^2}{(E^2 - E_c^2)^2 + B^2 E^2} \cdot \frac{1}{E} & E > E_g \\ 0 & E \leq E_g \end{cases}$$

where $G_{\text{T}}(E) = \frac{(E - E_g)^2}{E^2}$; $L(E) = \frac{AE_c BE}{(E^2 - E_c^2)^2 + B^2 E^2}$ (13)

$$\varepsilon_1^{\text{TL}} = \varepsilon_1(\infty) + \frac{2}{\pi} \cdot P \int_{E_g}^{\infty} \frac{\xi \varepsilon_2^{\text{TL}}(\xi)}{\xi^2 - E^2} d\xi$$

where $L(E)$ and $G_{\text{T}}(E)$ represent the Lorentz oscillator function and variable edge function respectively. E_g stands for the band gap (onset of absorbance). It can be seen that above the band gap the Tauc-Lorentz function behaves like a typical Lorentz oscillator. The real part of the Tauc-Lorentz can be found by a Kramers-Kronig transformation of the imaginary part ε_2 . In addition to A , E_c , and B which are general variables used for fitting the experimental ψ and Δ values, Tauc-Lorentz involves two more in E_g and $\varepsilon(\infty)$.

Whereas the Tauc-Lorentz model is rigid on the band gap side, Cody-Lorentz is said to offer contribution past that. It has several other fitting parameters compared to Tauc-Lorentz. Here the variable edge function $G(E)$ is different from the one used in Tauc-Lorentz as shown above.

$$\varepsilon_2^{\text{CL}} = \begin{cases} \frac{E_1}{E} \exp\left\{\frac{(E - (E_t + E_g))}{E_u}\right\} & 0 < E \leq (E_t + E_g) \\ G_{\text{C}}(E)L(E) & E > E_t \end{cases}$$

$$G_{\text{C}}(E) = \frac{(E - E_g)^2}{(E - E_g)^2 + E_p^2}; \quad E_1 = E_t L(E_t) G_{\text{C}}(E_t) \quad (14)$$

$$\varepsilon_1^{\text{CL}} = \varepsilon_1(\infty) + \frac{2}{\pi} \cdot P \int_{E_g}^{\infty} \frac{\xi \varepsilon_2^{\text{CL}}(\xi)}{\xi^2 - E^2} d\xi$$

where E_t is a transition energy between the Urbach tail and band-to-band transition, E_u is the material parameter corresponding to weak Urbach absorption. E_p is transition energy that separates the absorbance onset behavior from the Lorentzian behavior. E_p allows convergence of DOS at higher energies.²²

In order to model absorbing materials, certain steps are taken to make the convergence easier. First, the wavelength region where the material does not absorb was modeled. This was done by using a Cauchy dispersion layer. The A and B variables from the Cauchy equation and layer thickness were used as parameters to obtain a good fit. In this way, the thickness of the layer could be determined with relative ease. Upon obtaining the thickness, approximate optical constants of the polyfluorene layer were determined via point by point fit

for whole wavelength region. Point fit uses thickness, ψ and Δ values at each wavelength to calculate dielectric constants using the Fresnel equations. These dielectric constants are discrete values and hence not continuous functions. In order to obtain continuous Kramers-Kronig consistent dielectric constants, the obtained dielectric constants were now mimicked via Gaussian, Lorentzian, and other appropriate oscillators. Keeping the variables of the oscillator equations and thickness as parameters, fits to the experimental ψ and Δ values were obtained. For example, usage of three Gaussian oscillators involves a maximum of nine fitting parameters. It is easy to see that with more fitting parameters, modeling can become more difficult. By keeping the resonance energies fixed for all oscillators, the fitting parameters can be reduced to six, making modeling a little easier. However to get accurate optical constants with reduced parameters, some prior knowledge about the sample is required. For example, an absorbance curve of the material can help setting the resonance energies. Moreover, with help of the WVASE software,²⁴ extrinsic factors like surface roughness, light bandwidth, and depolarization effects can also be modeled.

The uniqueness of the fit is determined by the MSE (mean squared error) values and the correlations between the fitting parameters. If the fitting variables are dependent on each other one often gets a correlation of ± 1 . This means that the parameter values cannot be determined independently; even though the fit might be good but, the resulting n and κ values obtained might not be unique. To get unique optical constants, the correlation values between fitting parameters need to be less than 1. Moreover, upon modeling, the software also yields final values of fitting variables with their error margins. In order to obtain good fits, these error margins should be less than 10 % of the final values. This is often termed as 90 % confidence limit for fitting variables.

7.2.3 Optical constants of the substrates

As a first step, the optical constants of the substrates were determined. For the Si wafer substrate the optical constants were taken from the WVASE software.²⁴ However, Si wafers always carry a thin silicon oxide (SiO_2) layer on top. To determine the thickness of SiO_2 layer, ellipsometry experiments were carried out. Later a model was prepared utilizing the optical constants of Si and SiO_2 from the WVASE software to determine the thickness of the SiO_2 layer. Being transparent in region of 300–1700 nm, this could be achieved with relative ease. The SiO_2 thickness was determined as 2.46 nm. These substrates were further used for spin coating the polymer layers.

Similar experiments were done on bare glass substrates. The glass substrate in this case was covered with Scotch tape on the backside to minimize backside reflections. The Ψ and Δ values obtained for the glass were subsequently modeled, treating the glass substrate as dispersive Cauchy layer. The optical constants of glass as derived from the model are shown in Figure 1.

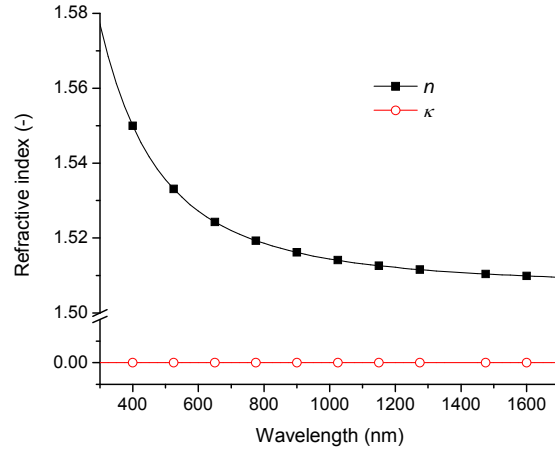


Figure 1: Optical constants of glass

7.2.4 Isotropy vs. anisotropy in the optical constants of chiral polyfluorene

In order to study chiral polyfluorene PF811 spin coated films on Si wafers, it was first assumed that the film is isotropic in nature. Using the thickness and oscillator variables as fit parameters, the experimental results were modeled using an isotropic model to obtain a fit with MSE values around 40 with maximum correlation around 8. The thickness of the film was calculated to be 64.51 nm, which is in close proximity to values calculated from the surface profilometer (~ 65 nm). The model fit complements the experimental values reasonably as shown in Figure 2(a). Subsequently, the n and κ values were derived from the model as shown in Figure 2(b). However, the shortcoming of assuming an isotropic film can be seen from the very poor overlap of the fit in the region around 350 nm (Figure 2(a)).

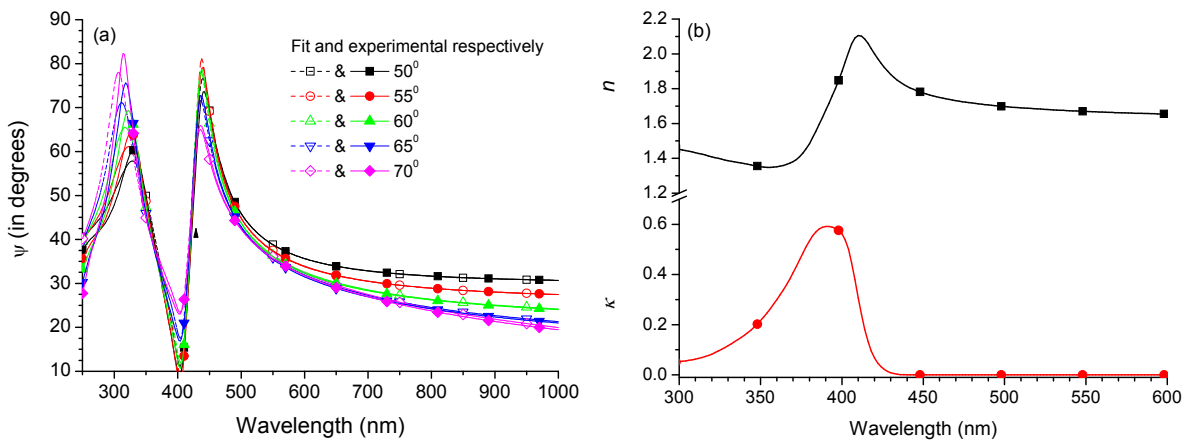


Figure 2: (a) Experimental Ψ values at different angles of incidence along with isotropic modeled fit for the thin film of PF811 (~ 65 nm) on Si wafer, (b) optical constants as obtained from the model fit.

In order to improve the fit, an anisotropic model can be considered. The uniaxial, rather than the biaxial, nature of the anisotropy of the PF811 film was established by the fact that ψ and Δ values are independent of rotation of the film about its normal (Figure 3a). Hence, the anisotropic axis is perpendicular to the plane of the film. In agreement with this conclusion, a

featureless image was observed under crossed polarizers with a polarizing microscope consistent with the isotropic nature of the film in the plane.

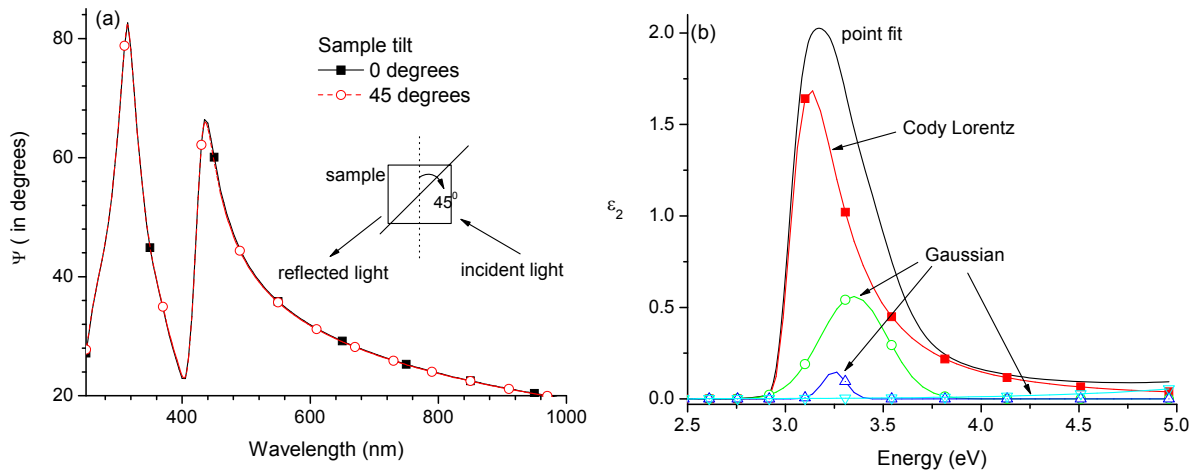


Figure 3: (a) ψ values recorded by the ellipsometer at 70° incidence for thin film of PF811 at different tilt angles. (b) General oscillator layer representing oscillators mimicking the point-by-point fit (top line).

The modeling was now performed with an anisotropic uniaxial model, taking into consideration contributions from ordinary and extraordinary optical constants. All steps were done using a coupled layer of ordinary and extraordinary optical constants. The thickness determined in this case was 64.84 nm; close to thickness calculate via isotropic model or surface profilometer. The oscillators used to mimic the point-by-point fit of the dielectric constant are shown in Figure 3b. All the oscillator variables (except, E_t , E_u , E_p in Cody Lorentz equation) were used as fitting parameters to obtain the best match to experimental Ψ and Δ values, as can be seen in Figure 4. The parameters E_t , E_u , E_p were not optimized: changing their value hardly influences the quality of the fit as estimated from the MSE values. Values used for E_t , E_u , E_p in the oscillator model are derive from point fit from the raw ϵ_2 data (the first step of the data analysis where n , κ , ϵ_1 and ϵ_2 are determined for every wavelength individually using Fresnel equations, see 7.2.2). The large value of E_u and the zero value of E_t imply essentially that there is no Urbach tail in the absorption spectrum. The best model yielded a fit with MSE around 13 and correlations around 0.9. All fitting variables and thickness are determined with 90% confidence limit. The strength of the different oscillators employed in the model, as derived from the solution are collected in Table 1.

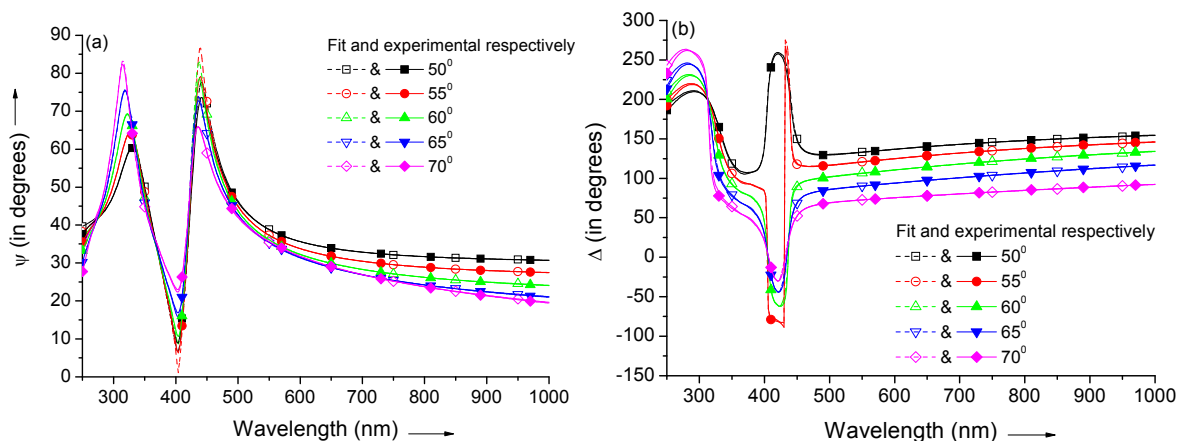


Figure 4: (a) Ψ and (b) Δ values recorded by the ellipsometer along with modeled fit for the thin film of chiral PF811 on Si wafer at different angles of incidence.

Oscillators	A (eV)	B (eV)	E_c (eV)
Cody-Lorentz (ordinary)	1.89	0.33	3.03
Gaussian (ordinary)	0.23	0.4	3.35
Gaussian (ordinary)	0.02	0.14	3.25
Gaussian (ordinary)	20.28	4.83	11.01
Gaussian (extraordinary)	0.30	0.42	3.28

Table 1: Strength of the oscillators used in the model for thin film of chiral PF811 on Si, as derived from the solution set. Additional parameters for Cody-Lorentz being (E_g 2.9 eV, E_p 0.26 eV, E_t 0 eV, E_u 100 eV). The shapes of the oscillators can be seen in Figure 3b.

7.3 Results and discussion

7.3.1 Anisotropic optical constants of chiral polyfluorene with thickness and substrate variation

By fitting the oscillator model to the experimental Ψ and Δ values, as explained in the modeling section above, anisotropic optical constants were obtained for both 40 and 65 nm thick films (Figure 5). The optical constants are largely independent of the film thickness. The ordinary (in-plane) components of the refractive index are larger than the extraordinary (out-of-plane) components. The absorption coefficient in the wavelength region corresponding to the transition from the ground state (S_0) to the lowest excited singlet state (S_1), for the light with \mathbf{E} in the direction of the normal (κ_{\perp}) is found to be 2 times less than for light with \mathbf{E} in the plane of the film (κ_{\parallel}). Because the transition dipole moment for this transition ($S_0 \rightarrow S_1$) lies parallel to the backbone of the polymer chain, the anisotropy indicates that the chains are preferentially oriented in an in-plane direction.

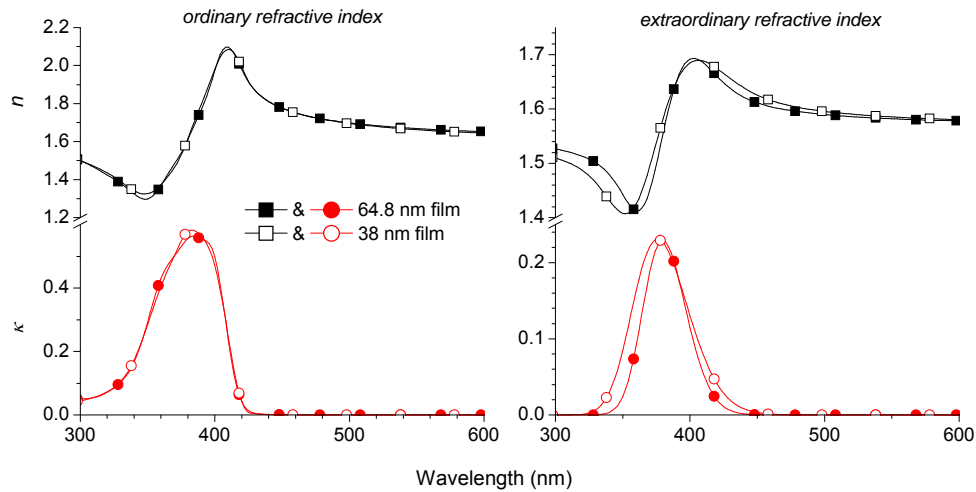


Figure 5: Anisotropic optical constants (n and κ) values of thin film of chiral polyfluorene on Si wafer as derived from the model fit for films with two different thicknesses.

Model (thin film PF811)	MSE	Max. correlation
Reported model (including all possible aberrations)	13.1	0.91
Ignoring surface roughness	22.31	0.74
Ignoring depolarization	16.4	0.92
Reduced number of fit parameters	7.61	1.0
Glass substrate	21.09	0.97

Table 2: Comparison of MSE and maximum correlation values for several models. See experimental section for details.

Several models were used in order to establish the uniqueness of the fit. The optical constants reported in Figure 5 are the solution to the model mentioned in first row of Table 2. This model takes care of surface roughness, light bandwidth, and depolarization effects. The MSE (13.1) and maximum correlation (0.91) are the best among different models and no model satisfies both the criteria of lowest MSE and lowest correlation.

The choice of the substrate has little effect as can be seen by comparing optical constants obtained from PF811 on a Si wafer (Figure 5) to those on glass (Figure 6). Optical constants obtained for chiral PF811 over glass substrates are a little lower in intensity. Oscillator strengths of the oscillators as used in the model are listed in Table 3. By using glass substrates, the modeling is complicated due to reflections from the back side of the glass. This could be a possible cause for some changes in optical constants. The obtained fit of chiral PF811 on the glass is still good but the MSE is relatively higher to around 20. The thickness determined from the ellipsometry is 67.8 nm, close to 65 nm value measured by the surface profilometer.

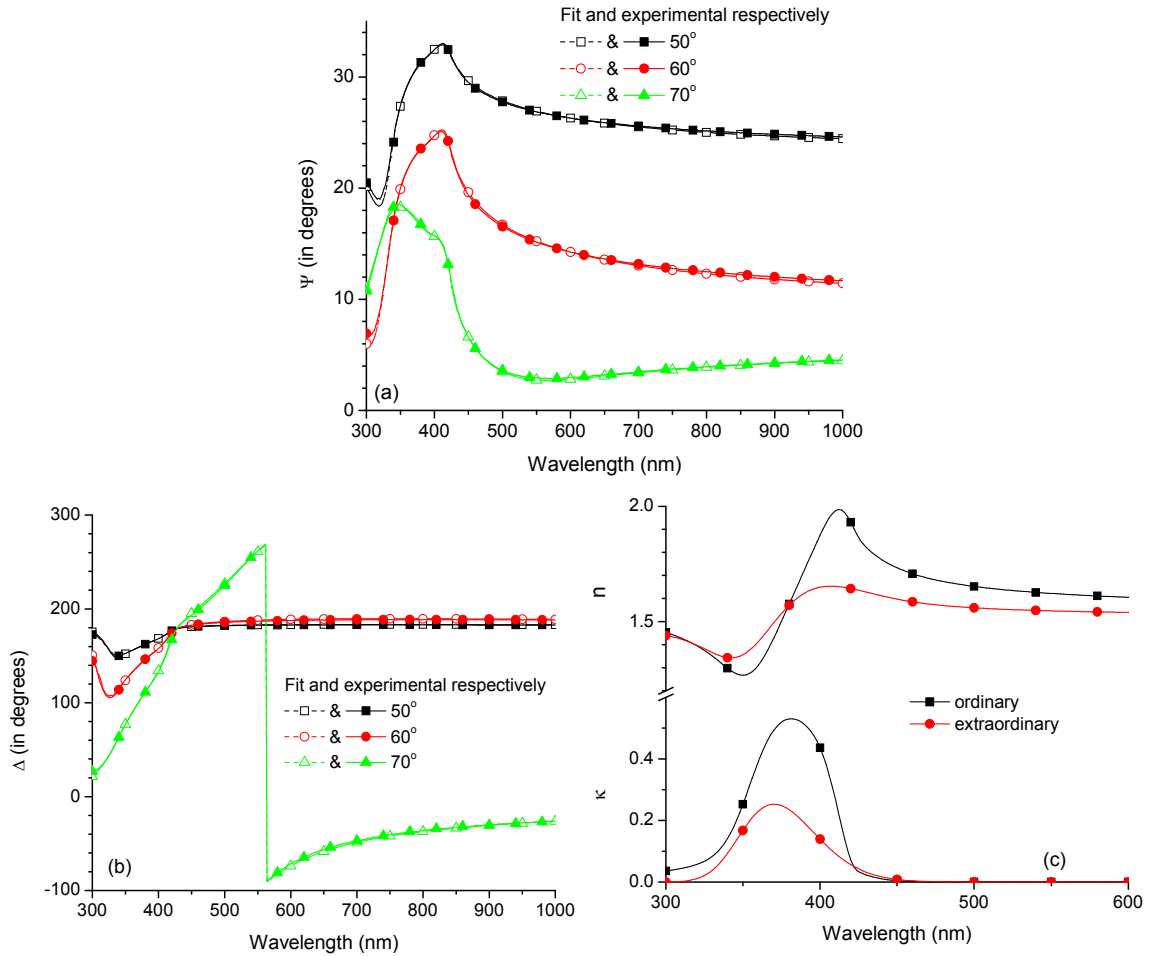


Figure 6: (a) Ψ and (b) Δ values recorded by the ellipsometer along with modeled fit for the thin film of chiral PF811 on glass substrate at different angles of incidence (c) optical constants (n and κ) of the same.

Using glass substrates, the ellipsometry experiment can also be done in transmission mode normal to the film. Using the model and oscillators as obtained from the solution (parameters mentioned in Table 1); the optical constants were used to calculate the transmission spectrum. The spectrum obtained matches well with the experimental curve, which was obtained from ellipsometry in transmission mode (Figure 7a). This confirms the validity of the optical constants. The transmission curve obtained from isotropic model is somewhat red shifted but the shape and amplitude are similar. By using the optical constants (κ) and thickness l as obtained from the model an absorbance curve can be modeled ($A = 4\pi\kappa l / (\lambda \ln 10)$). The modeled absorbance curve matches well with the experimental UV-Vis spectra, thereby validating the optical constants (Figure 7b).

Oscillators	$A(\text{eV})$	$B(\text{eV})$	$E_c(\text{eV})$
Cody-Lorentz (ordinary)	1.64	0.33	2.96
Gaussian (ordinary)	0.38	0.43	3.27
Gaussian (ordinary)	10.84	4.58	10.37
Gaussian (extraordinary)	0.39	0.52	3.32

Table 3: Strength of the oscillators used in the model for thin film of chiral PF811 on glass, as derived from the solution set. Additional parameters for Cody-Lorentz being (E_g 2.91 eV, E_p 0.23 eV, E_t 0 eV, E_u 100 eV).

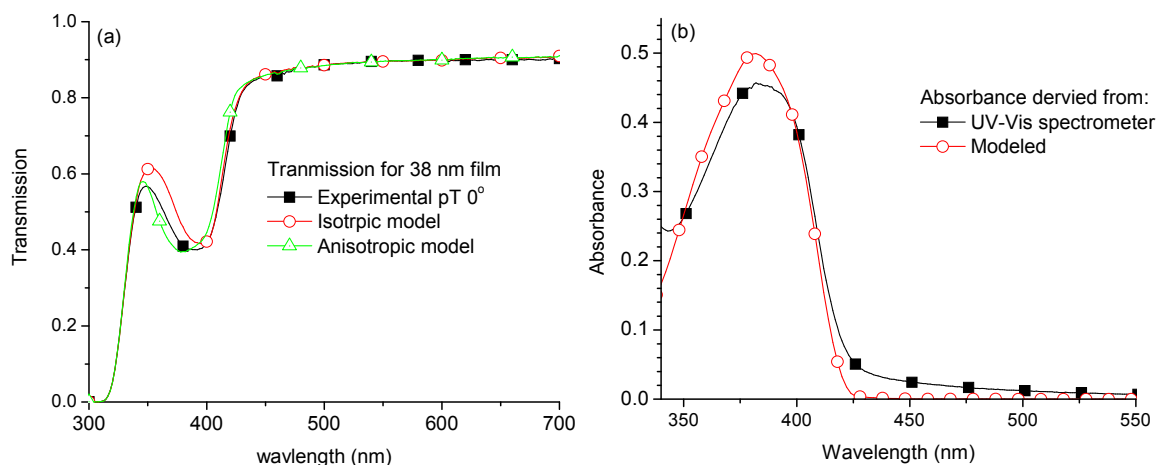


Figure 7: (a) Transmission experiments at 0° recorded from ellipsometer for a 38 nm film along with model fit. (b) UV-vis spectra for a 65 nm film and modeled spectra. The model used in both figures is of chiral PF811 on Si wafer, which also describes Figure 5.

7.3.2 Anisotropic optical constants of achiral polyfluorene

The optical constants of *achiral* polyfluorene (PFO) were also determined via ellipsometry to allow comparison to *chiral* PF811. The anisotropic optical constants determined for PFO (Figure 8) match well with the one reported in the literature.¹² Oscillator strengths of the oscillators as used in the model are listed in Table 4. The thickness measured via profilometer (~ 80 nm) matches well with the determined thickness from the ellipsometer (82 nm). Compared to its chiral analogue PF811 the optical constants of achiral PFO are somewhat higher.

Oscillators	$A(\text{eV})$	$B(\text{eV})$	$E_c(\text{eV})$
Cody-Lorentz (ordinary)	8.44	0.19	3.03
Gaussian (ordinary)	0.18	0.24	3.19
Gaussian (ordinary)	0.29	0.34	3.35
Gaussian (ordinary)	0.04	0.39	4.32
Gaussian (ordinary)	0.28	0.69	5.29
Gaussian (extraordinary)	0.16	0.31	3.21

Table 4: Strength of the oscillators used in the model for thin film of achiral PFO on Si, as derived from the solution set. Additional parameters for Cody-Lorentz being (E_g 2.91 eV, E_p 0.23 eV, E_t 0 eV, E_u 100 eV).

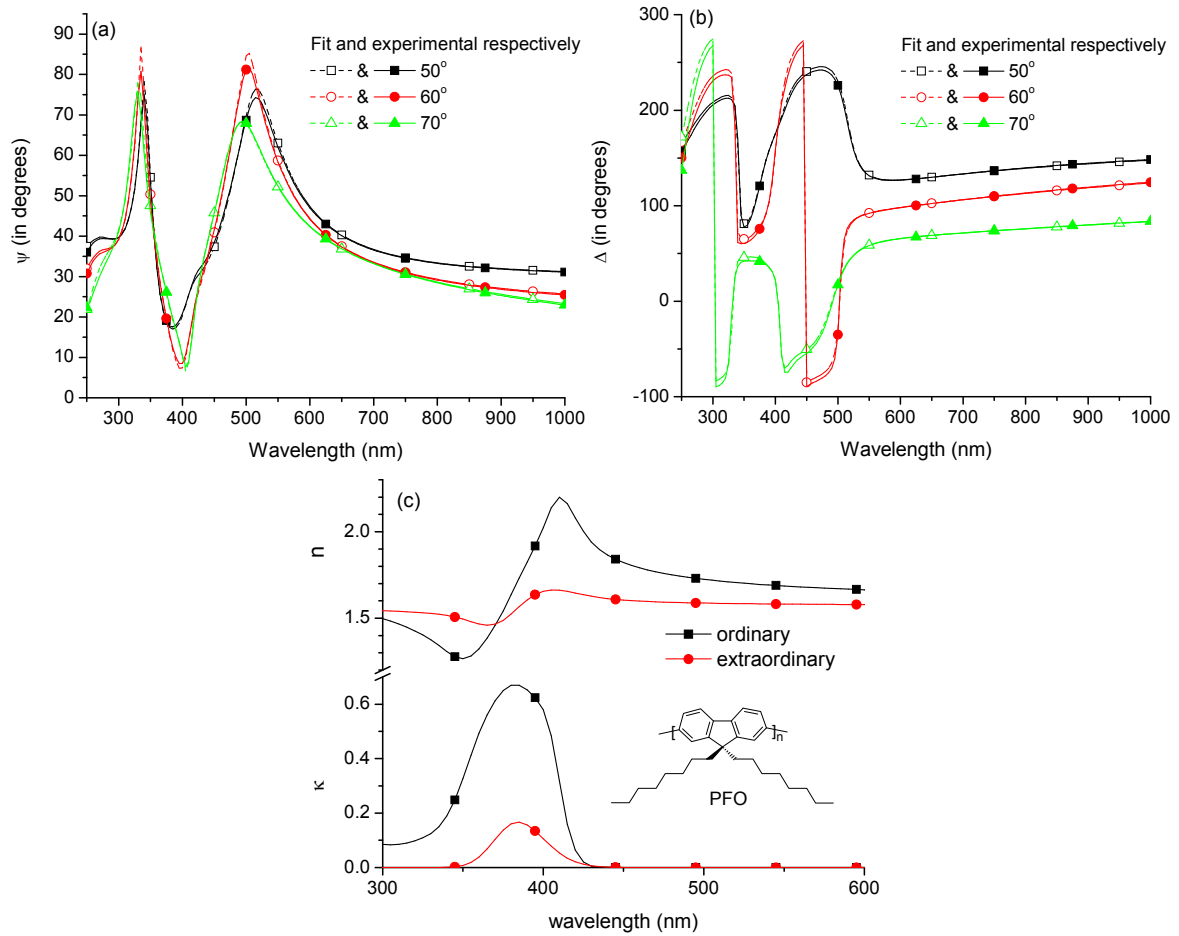


Figure 8: (a) Ψ and (b) Δ values recorded by the ellipsometer along with modeled fit for the thin film of achiral PFO on Si wafer at different angles of incidence (c) optical constants (n and κ) of the PFO alongwith structure.

Table 5 reveals that the differences in total oscillator strengths ($\int \epsilon_2(\omega) d\omega$) for the chiral and achiral polymer are about 10 %. This difference is also noticeable looking at the optical constants of both the polymers as shown in Figure 5 and Figure 8c respectively. The in-plane optical constants of achiral polyfluorene are higher in amplitude to its chiral analogue, whereas the out-of-plane component is lower for the achiral polymer. The differences in between ordinary and extraordinary optical constants of achiral polyfluorene are much larger than for the chiral counterpart, suggesting more in-plane alignment of the former (see $d_{\pi\theta}$ in Table 5 calculated for both polymers using eq. 17 explained in section 7.3.3). Both the polymers differ from each other because the chiral polymer has branched side chains. This can easily influence the way they crystallizes or aggregates in the film. This can possibly explain the differences in optical constants and preferential alignment on the polymer in the plane of the substrate.

Component	Oscillator strength of dielectric constants $\int_{2eV}^{4eV} \epsilon_2(\omega) d\omega$	
	achiral polyfluorene	chiral polyfluorene
Ordinary (in-plane) $\int_{2eV}^{4eV} \epsilon_{2,\parallel}(\omega) d\omega$	1.2	1.0
Extraordinary (out-of-plane) $\int_{2eV}^{4eV} \epsilon_{2,\perp}(\omega) d\omega$	0.17	0.3
Total $\int_{2eV}^{4eV} \epsilon_{2,\parallel}(\omega) d\omega + \int_{2eV}^{4eV} \epsilon_{2,\perp}(\omega) d\omega$	$(2 \times 1.2 + 0.17) = 2.57$	$(2 \times 1.0 + 0.3) = 2.3$
$d_{\pi\theta}$	0.93	0.87

Table 5: Total oscillator strength of dielectric constants for thin film of achiral PFO and chiral PF811 on Si.

7.3.3 Chiral polyfluorene orientation distribution in thin films

With the help of anisotropic optical constants as obtained for the thin film of chiral PF811, the extent of polymer orientation distribution, $d_{\pi\theta}$ can be determined via following equation:

$$d_{\pi\theta} = \frac{1}{1 + \frac{\int_{2eV}^{4eV} \epsilon_{2,\perp}(\omega) d\omega}{2 \int_{2eV}^{4eV} \epsilon_{2,\parallel}(\omega) d\omega}} \quad (15)$$

where $d_{\pi\theta} = 2/3$ for isotropic and $d_{\pi\theta} = 1$ for completely anisotropic (in-plane) orientation. Here it is assumed that the transition dipole for the π - π^* absorption of PF811 is oriented along the polymer chain and that the subscript θ represents the average polar angle of the polymer chains normal to the film. For a thin film of chiral PF811, the value obtained is 0.87. Assuming that the transition dipole moment is only along the polymer chain, this would indicate that up to 87% of the polymer chains lie parallel to the substrate. This result is in agreement to values reported elsewhere on various π -conjugated polymers^{4,5,25}

AFM studies on very thin films (< 20nm) of chiral PF811, as discussed in Chapter 3 and shown in Figure 9, revealed fibrillar structures. It was also found out that existence of fibrillar structures was conjoint with appearance of intensive CD spectra in pristine films. This intensive CD was found to be independent of the film thickness. These fibrillar structures are supposedly small aggregates containing few helically twisted polymer chains giving rise to bisignate CD due to intermolecular coupling.

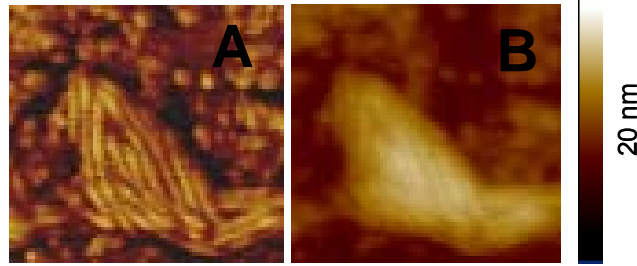


Figure 9: (A) AFM phase image of unannealed film spincoated from very dilute solution of chiral PF811 in chloroform, and B) corresponding AFM height image (height scale 20 nm, film thickness ≤ 15 nm) of the same.

We notice from the AFM images that the fibrillar structures lie in the plane of the film. The polymer orientation distribution ($d_{\pi\theta}$) as calculated from the anisotropic optical constants also reveals polymer alignment in the plane of the film. This indicates that fibril the polymer chains are is aligned parallel to major fibril axis.

7.3.4 Contribution of the pseudotensor G to the dielectric tensor of chiral polyfluorene

Chiral materials show circular dichroism (CD), *i.e.* a difference in absorbance for left and right circularly polarized light ($\Delta A = A_L - A_R$). In Figure 10 this CD is illustrated together with the absorbance for a thin, unannealed film of PF811 with a thickness of 65 nm. CD band shape of these pristine films is similar to ones reported in Chapter 3.

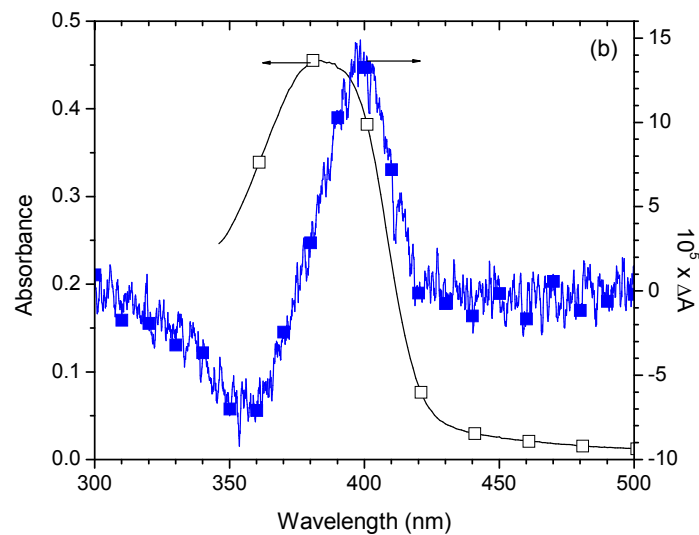


Figure 10: Absorbance and CD spectra of thin chiral polyfluorene film on glass substrate (~ 65 nm).

The measurement illustrated in Figure 10 pertains to light incident along the normal of the film. The CD measured in this way is related to the G_{12} element of the pseudotensor G in eq. 3. Using eq. 8 we can express this relation as:

$$G_{12}'' = \Delta\kappa = \kappa_L - \kappa_R = \ln 10 \Delta A \frac{\lambda}{4\pi l} \quad (16)$$

The real G_{12}' can be approximated by taking the Kramers-Kronig (KK) transform of G_{12}'' . This was done by fitting two Gaussian curves, one with positive and one with negative amplitude to G_{12}'' . Taking the regular fit parameters for the Gaussian curves, G_{12}' can be constructed as the sum of two KK transformed Gaussian curves. In this procedure, the contribution of CD bands to the optical rotation in G_{12}'' outside the window of measurements is not included. This contribution will be a slowly varying offset. In the neighborhood of resonance, the calculated G_{12}' is a reasonable approximation. Results are shown in Figure 11b.

Figure 11 illustrates the photon energy dependence of various elements of the dielectric tensor of chiral polyfluorene. As can be seen, the absolute magnitude of the real and imaginary parts of the element G_{12} is of the order 10^{-4} , *i.e.* much smaller than ε_{\perp} . This large difference in magnitudes provides justification to the procedure involved in determining the ε_{\perp} . Here we used ellipsometry and ignored the chirality dependent term in the dielectric tensor.

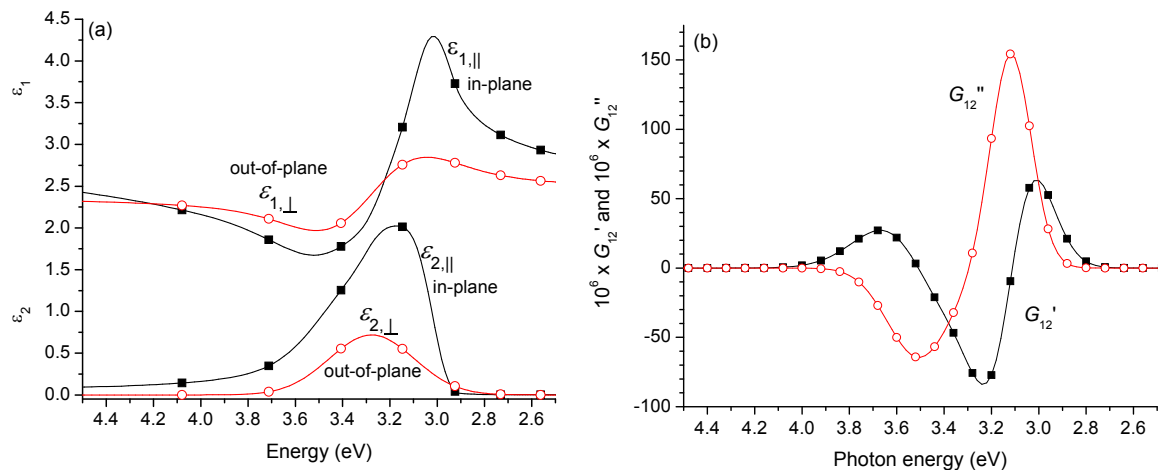


Figure 11: (a) In-plane and out-of-plane dielectric constants of chiral polyfluorene film on glass substrate ($\sim 65\text{nm}$). (b) Anisotropic tensor G_{12}' and G_{12}'' of the same.

As mentioned in the introduction of this chapter, the influence of the chirality dependent pseudotensor G on the reflectivity of chiral materials is presently poorly understood. Zheludev *et. al.* have proposed a relation between G and optical activity in reflection of light on the interface between vacuum (air) and an infinitely thick layer of homogenous chiral material:

$$\delta\eta_r + i\delta\alpha_r = \frac{G_{12}}{1 - \varepsilon} \quad (17)$$

Here $\delta\eta_r$ is the degree of ellipticity (in radians) of light reflected from the interface between air and chiral dielectric material when linear polarized light is incident along the surface normal, whereas $\delta\alpha_r$ (in radians) is the corresponding optical rotation of the plane of polarization in the reflected light. Using the elements of the dielectric tensor for the chiral polyfluorene (Figure 11) we can now make predictions for the specular optical activity. These predictions are shown in Figure 12. Based on eq. 17 rotation of linearly polarized light is predicted up to angle of 0.05 mrad (~ 3 mdeg). Although these values are small, they are comparable to the detection limit of modern optical equipment. The values predicted here are similar to those reported for α -HgS.¹⁶

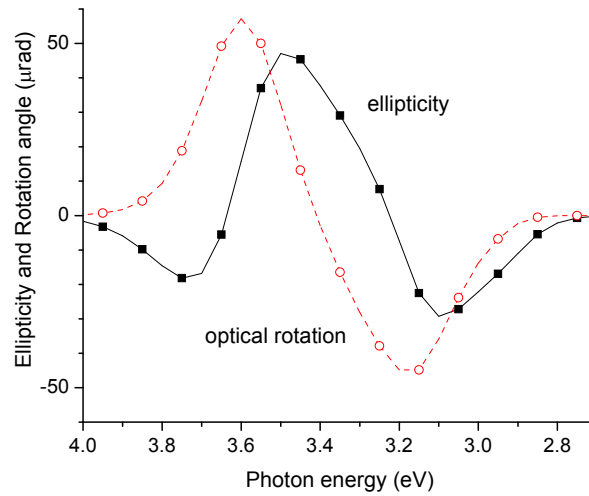


Figure 12: Prediction based on eq. 17 for the ellipticity and angle of rotation of the plane of polarization (in $10^{-6} \times \text{rad}$) after reflection of a linearly polarized light beam incident along the surface normal to an infinitely thick layer of chiral polyfluorene.

For photon energies around 3.1 eV the reflectivity of an infinitely thick layer of chiral polyfluorene reaches a maximum (Figure 13). From the predicted ellipticity of the reflected light, we can calculate the degree of circular polarization in the reflected light g_{refl} (see Figure 13a). We predict $g_{\text{refl}} = 0.2 \times 10^{-3}$ at 3.5 eV. This is slightly above to the detection limit for experimental methods to determine the degree of circular polarization of light by e.g. photon counting. From these calculations we conclude that the specular optical activity as predicted by eq. 17 is amenable to experimental verification. Finally we also estimate the contribution of selective reflection of circular polarized light to the measured circular dichroism. For an infinitely thick layer we calculate a contribution as show in Figure 13b. This prediction can be compared to the circular dichroism measured for a film of 65 nm thickness. Near the onset of the absorption at 3.0 eV, both the selective absorption and the selective reflection contribute to the positive value of ΔA . For higher photon energies the predicted reflection contribution would cause the measured selective extinction to be lower than the selective absorption. For photon energies around 3.2 eV, we estimate the contribution of reflection to the measured ΔA to be about 5×10^{-6} at 3.2 eV (Figure 13b). This contribution is about 10 times smaller than the experimental ΔA from the 65 nm thick film. The fact that the predicted contribution of

reflection to the total circular differential transmission, is significantly smaller than the experimental data used to calculate G_{12} , indicates that our method for determining G_{12} is close to self-consistent if eq. 17 is indeed correct. The results also indicate that if eq. 17 holds then CD spectra for films of chiral materials may be significantly affected by contributions from selective reflection.

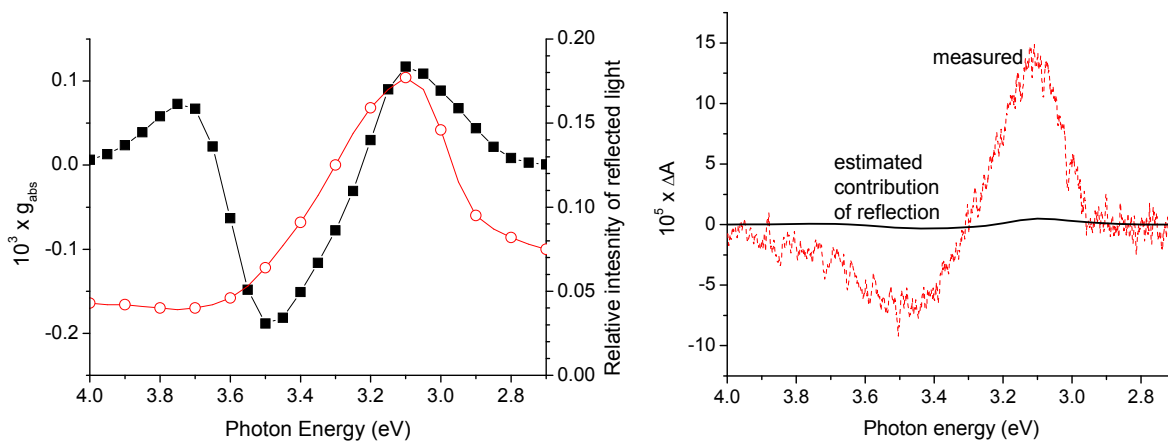


Figure 13: a) Predicted degree of circular polarization after reflection (g_{ref}) of an initially linearly polarized light beam incident along the surface normal on an infinitely thick layer of chiral polyfluorene. Corresponding intensity of reflected light relative to that of the incoming beam calculated from data on \tilde{n} as shown in Figure 6 (-o-). b) Estimated contribution of the circular selective reflection to the measured extinction (ΔA , solid line). For comparison the CD recorded on a 65 nm thick film is also shown (dashed line).

Finally we return to the elements of the dielectric tensor of the chiral polyfluorene as shown in Figure 12. A possible qualitative interpretation of these elements in terms of the orientation of the polymer chains in the film is illustrated in Figure 14.

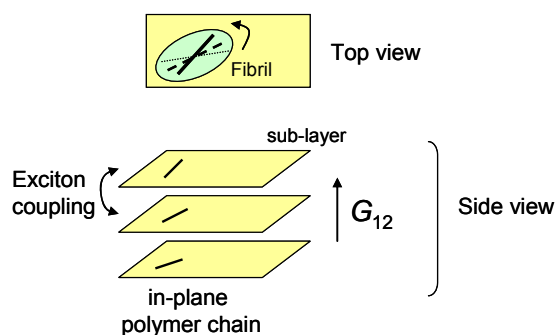


Figure 14: Pictorial representation of polymer alignment in the plain within a fibril. Only one chain is represented in order to maintain the clarity of the image.

We assume here that all polymer chains are aligned in the plane of the film and that there is a correlation in the orientation of the polymer chains in adjacent sub-layer of the film. This gives rise to a helical arrangement of the chains through the sub-layers when viewed from above. Coupling between the transition dipole moments of the chains in neighboring sub-layers gives rise to CD and hence to a non-zero value of G_{12} . A small value of the helical twist angle between plans is compatible with small values of G_{12} . Assuming that all polymers are

oriented in the same plane, the elements G_{13} and G_{23} are zero. The fibrillar aggregates observed in AFM may now be interpreted being made up of a number of coplanar chains in each sub-plane with a helical organization between the sub-planes. This is consistent with the findings from chapter 3 where the occurrence of CD in the pristine polymer film was found to be linked to the fibril formation.

7.4 Conclusion

The dielectric tensor ε for a pristine thin film of *chiral* polyfluorene is found to be anisotropic with non zero pseudoscalar off-diagonal elements determined by combining results from spectroscopic ellipsometry and circular dichroism. This is the first time that such a detailed characterization has been carried out on a film of chiral π -conjugated polymer.

The anisotropy was found to be uniaxial with a majority of the polymer chains lying in the plane of the film. AFM studies (also discussed in Chapter 3) revealed fibrillous structures on the surface of the film, also oriented along the plane of the substrate. This indicates that the in-plane alignment of polymer chains and the formation of fibrils could be coupled process taking place during spin coating upon evaporation of the solvent.

The chirality of the polymer expresses itself through a non-zero value of the pseudoscalar off diagonal element G_{12} of ε . These essentially describe a non-local response of the polymer film to incident light. This non-local response also has implications for the reflection of light, but this is not very well understood at the moment. Here we used the values of the dielectric tensor obtained to make predictions for the optical rotation and circular selectivity in reflection of light according to the theory developed by Zheludev *et al.*^{17,26} We find that the predicted optical rotation and circular selectivity in reflection are small but nevertheless of an experimentally accessible magnitude. These predictions call for attention from the scientific community in order to develop a deeper understanding of the reflection of light by molecular materials.

References

1. (a) Shkunov, M.N.; Österbacka, R.; Fujii, A.; Yoshino, K.; Vardeny, Z.V. *Appl. Phys. Lett.* **1998**, *74*, 1648. (b) Long, X.; Malinowski, A.; Bradley, D.D.C.; Inbasekaran, M.; Woo, E.P. *Chem. Phys. Lett.* **1997**, *272*, 6.
2. (a) Grell, M.; Knoll, W.; Lupo, D.; Meisel, A.; Miteva, T.; Neher, D.; Nothofer, H.G.; Scherf, U.; Yasuda, A. *Adv. Mat.* **1999**, *11*, 671. (b) Shu, C.F.; Dodda, R.; Wu, F.I.; Liu, M.S.; Jen, A.K.Y. *Macromolecules* **2003**, *36*, 6698.
3. (a) Gymer, R.W.; Friend, R.H.; Ahmed, H.; Burn, P.L.; Kraft, A.M.; Holmes, A.B. *Synth. Met.* **1993**, *55–57*, 3683. (b) Sturm, J.; Tasch, S.; Niko, A.; Leising, G.; Toussaere, E.; Zyss, J.; Kowalczyk, T.C.; Singer, K.D.; Scherf, U.; Huber, J. *Thin Solid Films* **1997**, *298*, 138. (c) Pettersson, L.A.A.; Carlsson, F.; Inganas, O.; Arwin, H. *Thin Solid Films* **1998**, *313–314*, 356.
4. McBranch, D.; Campbell, I.H.; Smith, D.L.; Ferraris, J.P. *Appl. Phys. Lett.* **1995**, *66*, 1175.
5. Tammer, M.; Monkman A. P. *Adv. Mater.* **2002**, *14*, 210.
6. Ramsdale, C.M.; Greenham, N.C. *Adv. Mater.* **2002**, *14*, 212

7. Wan, W.M.V.; Greenham, N.C.; Friend, R.H. *J. Appl. Phys.* **2000**, *87*, 2542
8. Fell, H.J.; Samuelsen, E.J.; Als-Nielsen, J.; Grubel, G.; Mardalen, J. *Solid State Comm.* **1995**, *94*, 843.
9. Campoy-Quiles, M.; Heliotis, G.; Xia, R.; Ariu, M.; Pintani, M.; Etchegoin, P; Bradley, D. D. C. *Adv. Funct. Mater.* **2005**, *15*, 925.
10. (a) Winfield, J. M.; Donley, C. L.; Kim, J.-S. *J. Appl. Phys.* **2007**, *102*, 063505. (b) Campoy-Quiles, M.; Etchegoin, P; Bradley, D. D. C. *Phys. Rev. B* **2005**, *72*, 045209.
11. Ramsdale, C. M.; Greenham, N. C. *Adv. Mater.* **2002**, *14*, 212.
12. Campoy-Quiles, M.; Etchegoin, P; Bradley, D. D. C. *Synth. Met.* **2005**, *15*, 279.
13. Zhokhaverts, U; Goldhahn, R.; Gobsch, G.; Al-Ibrahim, M; Roth, H.-K.; Sensfuss, S.; Klemm, E.; Egbe, D. A. M *Thin Solid Films*, **2003**, *444*, 215.
14. Tammer, M.; Higgins, R. W. T.; Monkman, A. P. *J. Appl. Phys.* **2002**, *91*, 4010.
15. Agranovich, V.M.; Ginzburg, V.L. *Crystal optics with spatial dispersion, and excitations*, Springer-Berlin, **1984**.
16. (a) Bungay, A.R.; Svirko, Yu. P.; Zheludev N.I. *Phys. Rev. Lett.* **1993**, *70*, 3039. (b) Bungay, A.R.; Svirko, Y.P.; Zheludev N. I. *Phys. Rev. B* **1993**, *47*, 16141.
17. Silverman, M.P.; Badoz, J.; Briat, B. *Opt. Lett.* **1992**, *17*, 886.
18. Graham, E.B.; Raab, R.E. *J. Opt. Soc. Am. A* **1996**, *13*, 1239.
19. De Vries, H. L. *Acta Cryst.* **1951**, *4*, 219.
20. Paget, D.F.; Elliott, D. *Numer. Math.* **1972**, *19*, 373.
21. (a) Ferlauto, A.S.; Ferreira, G.M.; Pearce, J.M.; Wronski, C.R.; Collins, R.W.; Deng, X.; Ganguly, G. *Thin Solid Films* **2004**, *455–456*, 388. (b) Eiamchai, P.; Chindaudom, P.; Pokaipisit, A.; Limsuwan, P. *Current Applied Physics* **2009**, *9*, 707. (c) Ohlidal, I.; Franta, D.; Šiler, M.; Vižda, F.; Frumar, M.; Jedelský, J; Omasta, J. *J. Non-Cryst. Solids* **2006**, *352*, 5633.
22. Price, J.; Hung, P.Y.; Rhoad, T.; Foran, B. *Appl. Phys. Lett.* **2004**, *85*, 1701.
23. (a) Jellison Jr, G.E.; Modine, F.A.; *Appl. Phys. Lett.* **1996**, *69*, 2137. (b) Diebold, A.C.; Canterbury, J.; Chism, W.; Richter, C.; Nguyen, N.; Ehrstein, J.; Weintraub, C. *Materials Science in Semiconductor Processing* **2001**, *4*, 3.
24. WVASE software
25. Law, C.W.Y.; Wong, K.S.; Yang, Z.; Horsburgh, L.E.; Monkman, A.P. *Appl. Phys. Lett.* **2000**, *76*, 1416.

Probing charge carrier density in a p-n junction of conducting polymer and a layer of ZnO nanoparticles by spectroscopic ellipsometry

Abstract. The Moss-Burstein shift, *i.e.* an apparent increase of the optical band gap, is observed upon UV illumination of a layer of 5 nm ZnO nanoparticles in O₂-free atmosphere using spectroscopic ellipsometry. This shift is caused by populating the conduction band with excess free charge carriers and depleting the valence band. The free charge carrier density was determined to be $2 \times 10^{19} / \text{cm}^3$, about one carrier per particle. The shift can be reversed by introduction of O₂. For junctions of ZnO nanoparticle layers with a pH neutral-PEDOT:PSS conducting polymer layer a depletion width of 5 nm in ZnO is observed under UV illumination in O₂-free atmosphere. At the junction free charge carriers in ZnO are transferred to neutral-PEDOT:PSS causing a slight reduction of the latter.

8.1 Introduction

By appropriate doping a semiconductor can be made to conduct either holes or electrons (p-type and n-type). Junctions between p-type and n-type semiconductors are used in many electronic devices (rectifier, solar cells, LEDs) and are characterized by a depletion layer in which the charge carrier density is reduced to align the Fermi levels on both sides of the junction. Upon increasing the doping levels the width of depletion layer of the p-n junction becomes very narrow and tunneling of charge carriers can take place (Figure 1). This is utilized in so-called tunnel or Esaki diodes.¹ With very high degrees of doping, the p-n junction is eventually expected to behave as Ohmic contact. p-n Junctions can be modeled accurately and are well understood both from a physics and electronics perspective. However, from a chemical point of view the formation of a quasi Ohmic contact in p-n junctions is less clear.

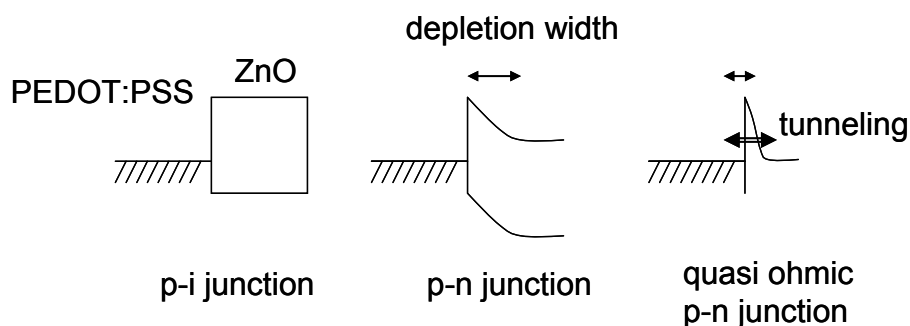


Figure 1: Band diagram of various p-n junctions. Here ‘i’ stands for insulator.

Recently formation of an quasi Ohmic junction between a heavily doped organic p-type conductor, poly(ethylenedioxythiophene):poly(styrenesulfonate) (PEDOT:PSS),² and an inorganic n-type layer of ZnO nanoparticles has been demonstrated.³ The formation of these junctions can be studied into considerable detail because the effective doping level in the ZnO layer can be controlled externally either by UV illumination or by applying a high bias voltage over appropriately applied electrodes.³

Ohmic ZnO/PEDOT:PSS junctions are of considerable practical importance. It was found that these junctions show resistive switching and may be applied as electronic memory cell.⁴ Here the resistance of the quasi Ohmic junction can be altered reversibly by applying a potential difference across the junction. A second application of the ZnO/PEDOT:PSS junctions is in solution processed multijunction solar cells.⁵ Here an internal ZnO nanoparticle/PEDOT:PSS junction between two photovoltaic active bulk heterojunction layers is used to align the conduction band of one cell with the valence band of the other. This alignment takes place when the junction becomes Ohmic after illuminating the ZnO layer with UV light. Interestingly also other metal oxides are capable of forming such a Ohmic junction like TiO_x /PEDOT:PSS.⁶ Therefore knowledge of the electronic structure of the ZnO/PEDOT:PSS interface is important for a complete understanding of the operation of these organic memories and multijunction solar cells.

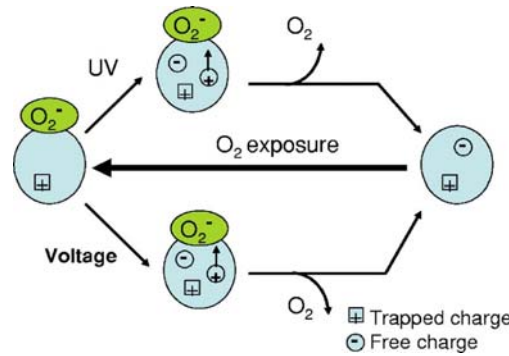


Figure 2: Schematic representation of the UV light and bias voltage induced n-type doping of ZnO nanoparticles under O_2 -free conditions.³

ZnO has n-type character, resulting from the presence of positively charged, stationary defects that are compensated by electrons in the conduction band. In the presence of O_2 , the mobile electrons are scavenged by O_2 molecules adsorbed to the surface of the nanoparticles and the n-type character is strongly suppressed (Figure 2). Under O_2 -free conditions, introduction of mobile holes and electrons, either via contacts and applying a high bias voltage or by photoexcitation, into the ZnO nanoparticles leads to recombination of the mobile holes with O_2^- and subsequent desorption of O_2 from the surface. As a result, the remaining particles have an increased density of mobile electrons, leading to persistent (photo)conductivity.⁷

Apart from changing the conductivity, the presence of the mobile electrons also changes the optical properties of the ZnO. Earlier studies on ZnO, where the level of n-type doping was varied systematically⁸ (using e.g. In⁹ and Al¹⁰ as extrinsic dopants) have revealed a correlation between the optical properties of the doped semiconductor and density of electrons in the conduction band. The changes in optical properties near the onset of the absorption resulting from the band to band transition can be understood in terms of the Moss-Burstein effect, which is a shift of the band gap with increasing doping levels.^{11,12} Photodoping of ZnO nanoparticles in dilute solution results in similar effects in the transmission spectra.¹³

After partially filling up the conduction band of ZnO with electrons, higher photon energy is required to excite an electron from the valence band of ZnO to an empty level in the conduction band. This results in an apparent increase in the semiconductor band gap that is marked by a blue shift in the absorption edge of the ZnO. The following simple relation has been proposed to describe the magnitude of the Moss-Burstein shift in ZnO:

$$E_{\min} = E_g + \frac{\hbar^2}{2} \left(\frac{1}{m_{\text{red}}} \right) (3\pi^2 n_C)^{2/3} \quad (1)$$

where n_C denotes the density of charge carriers in the conduction band and m_{red} the reduced effective mass of the electron hole pair: $1/m_{\text{red}} = 1/m_C + 1/m_V$, with m_C and m_V the effective

masses of the carriers in the conduction and valence band ($m_C = 0.28m_0$, $m_V = 0.58m_0$ and m_0 the electron rest mass).¹⁰ E_g is the undoped band gap and E_{\min} the photon energy corresponding to the onset of absorbance arising from valence to conduction band transition in the direct band gap semiconductor. Experiments on ZnO doped by various donors have indeed revealed the predicted $n_C^{2/3}$ dependence at low doping densities^{8-10,14} ($n_C \leq 2 \times 10^{19}/\text{cm}^3$). These experiments also showed that various corrections to eq 1 are necessary to quantitatively explain the observed Moss-Burstein shift, especially at high doping densities.¹⁵

Here we use ellipsometry to study the optical properties of a layer ZnO nanoparticles and to probe the electronic structure of the ZnO/PEDOT:PSS n-p junction. In these experiments we use UV light to externally modify the effective degree of doping in ZnO. From evaluating the magnitude of the Moss-Burstein shift we estimate the density of mobile electrons in the ZnO. Using ellipsometry, we investigate ZnO/PEDOT:PSS junction directly and the results are found to be consistent with transfer of electrons from the n to the p type material across the n-p junction. Kelvin probe measurements are used as an independent measurement of the estimated density of carriers and allow obtaining an estimate of the depletion width of the ZnO/PEDOT:PSS junction.

8.2 Experimental section

ZnO layers were deposited from ZnO nanoparticles which were synthesized as described previously by hydrolysis and condensation of zinc acetate dihydrate (Acros) by potassium hydroxide (Merck) in methanol (Biosolve).¹⁶ After centrifugation the nanoparticles with an average diameter of 5 nm were dissolved in acetone for spin coating to obtain 25, 35-40, and 100 nm thick layers from 10, 10 and 25 mg/ml concentrated solutions respectively on the different substrates (Si wafer, glass/indium tin oxide (ITO), and bare glass). The ZnO films on glass/ITO were used for Kelvin probe experiments whereas films on Si and bare glass were used for ellipsometry experiments.

For the ITO/PEDOT:PSS/ZnO/LiF/Al p-n devices, 50 nm of PEDOT:PSS (Clevios™ P VP AI 4083, HC Starck) was deposited on glass/ITO (Naranjo Substrates) by spin coating, followed by deposition of 40 nm ZnO from nanoparticles dissolved in acetone. The sample was subsequently transferred to a nitrogen filled glovebox for the evaporation of LiF (1 nm) and Al (100 nm) at a pressure of 10^{-7} mbar. The current density vs. voltage measurements (sweep from -2 to 2 V) were performed with a Labview controlled Keithley 2400 source meter.

For fabricating ZnO/PEDOT:PSS junctions it is important to realize that ZnO readily dissolves in the low pH PEDOT:PSS (Clevios™ P VP AI 4083) dispersion. Hence, we used a pH-neutral PEDOT:PSS (n-PEDOT:PSS, Orgacon, batch 5541073, $pH = 7$, 1.2 wt%, Agfa Gevaert NV), spin coated from water after 1:1 dilution to obtain a 15 nm layer on glass or on a layer of ZnO nanoparticles.

Spin coating neutral-PEDOT:PSS on a bare Si wafer was hampered by poor wetting of the substrate. These dewetting problems were avoided by using glass as a substrate. To minimize

reflections from the backside of the glass substrate in the ellipsometry measurements, the backside was covered with Scotch tape or scratched in order to give diffuse reflection to the incident light at this interface.

Optical constants of layer of ZnO nanoparticle and PEDOT:PSS layers were determined via ellipsometry experiments in air at variable angles over a 300-1700 nm wavelength region using a WVASE32 ellipsometer (J. A. Woollam Co., Inc). Illumination with UV light under O₂ free conditions was performed by placing the sample film in a special sample holder (VASE heat cell attachment, Heatcell.03 c) and flushing with argon. The sample holder has two fused silica windows that allow passage to incident and reflected light. Possible attenuation and phase lag of incident and reflected light when passing through these windows was taken into consideration while modeling the experimental ellipsometric data ψ and Δ . These windows are held at a fixed angle to each other, which is why ellipsometry experiments using this sample holder could only be done at 70° angle. For illumination experiments in ellipsometry a UV lamp was used (Spectroline, ENF 260C/F) that can be operated in two modes. The first gives 254 nm Hg emission with narrow wavelength distribution, the second gives a broad emission band centered on 365 nm. UV illumination on the p-n diode device ITO/PEDOT:PSS/ZnO/LiF/Al was carried out using a Money Detector ($\lambda = 350$ nm, 2 W, NCT-168M, Zhongshan Ruihe Electric Appliance).

Ellipsometric measurements were done on Si wafer or glass substrates. Ellipsometric measurements were performed on layer of ZnO nanoparticles on a Si wafer. Using Si substrates makes the measurement and modeling easier primarily because it has no backside reflections for photon energies above the band gap, unlike commonly used glass or quartz substrates. The thickness of SiO₂ layer (2.28 nm) on top of Si wafer was determined using ellipsometry and used in subsequent modeling. The optical constants of Si and SiO₂ used for modeling were provided by ellipsometer software.¹⁷ In case of glass as a substrate, the optical constants of the glass used were determined separately. The optical constants of glass are shown in Figure 1 in Chapter 7. Roughness in the films was accounted by two different methods. First, an additional (effective medium approximation, EMA) layer comprising ZnO nanoparticles and 50% voids was used on top of the ZnO layer. The thickness of this layer was an additional fitting parameter. Bruggeman approximation was used for the EMA layer. Second, ‘global’ roughness was applied from the software options. This was used as the standard method, unless mentioned otherwise.

Kelvin Probe measurements were performed in a nitrogen glove box. In every measurement, the work function was monitored over 30 minutes. A commercial instrument was used (Besocke Delta Phi, Kelvin Probe S and Kelvin Control 07) enclosed in a home-built Faraday cage. The Kelvin Probe was calibrated with freshly cleaved highly oriented pyrolytic graphite (HOPG), which has a stable work function of 4.48 eV.¹⁸ ZnO samples were put inside the glove box and measured. Next, the samples were illuminated for 30 minutes with a solar simulator (Steuernagel, Solar Constant 1200) in a nitrogen glove box and measured afterwards. Finally, the samples were exposed to air outside the glove box for 30 minutes and the work function was measured again afterwards.

8.3 Results and discussion

In this section we will first investigate the electrical properties of ZnO/PEDOT:PSS n-p junctions and illustrate the formation of the Ohmic junction between ZnO and PEDOT:PSS after illumination of the ZnO layer with UV light. Secondly, we will investigate the changes in optical properties induced in ZnO by the UV light, through spectroscopic ellipsometry. This results in an estimate of the density of free carriers after photodoping. We then determine optical constants for acidic and pH neutral PEDOT:PSS layers and subsequently investigate the optical properties of ZnO/PEDOT:PSS junctions directly with ellipsometry upon illumination with UV light. This provides evidence for charge transfer at the interface between the two materials. Kelvin probe measurements on the ZnO layer of different thicknesses will be used to check the estimate of free carriers after photodoping obtained from ellipsometry and to estimate the width of the depletion zone.

8.3.1 Formation of a quasi ohmic contact in an ITO/ ZnO / PEDOT-PSS junction

The evolution of a p-n junction towards an Ohmic contact upon increasing the doping density has been studied electrically in glass/ITO/ZnO/PEDOT:PSS/Al and glass/ITO/neutral-PEDOT:PSS/ZnO/Al. Figure 3 shows I-V characteristics of both device configurations. Before UV illumination, the pristine devices show a typical non-linear I-V characteristic, characteristic of a Schottky junction. Upon UV-illumination, the I-V characteristics of the device become linear, *i.e.* Ohmic in nature, for both device configurations. Before UV illumination the current densities are lower than after UV illumination. We attribute this to a large increase in the density of mobile electrons in the ZnO upon illumination. Upon exposure to oxygen we assume that all mobile electrons in the ZnO are scavenged by oxygen and that the ZnO behaves as an intrinsic wide band gap semiconductor.

The fact that both devices show a transition to Ohmic behavior upon UV illumination confirms photodoping of the ZnO layer.

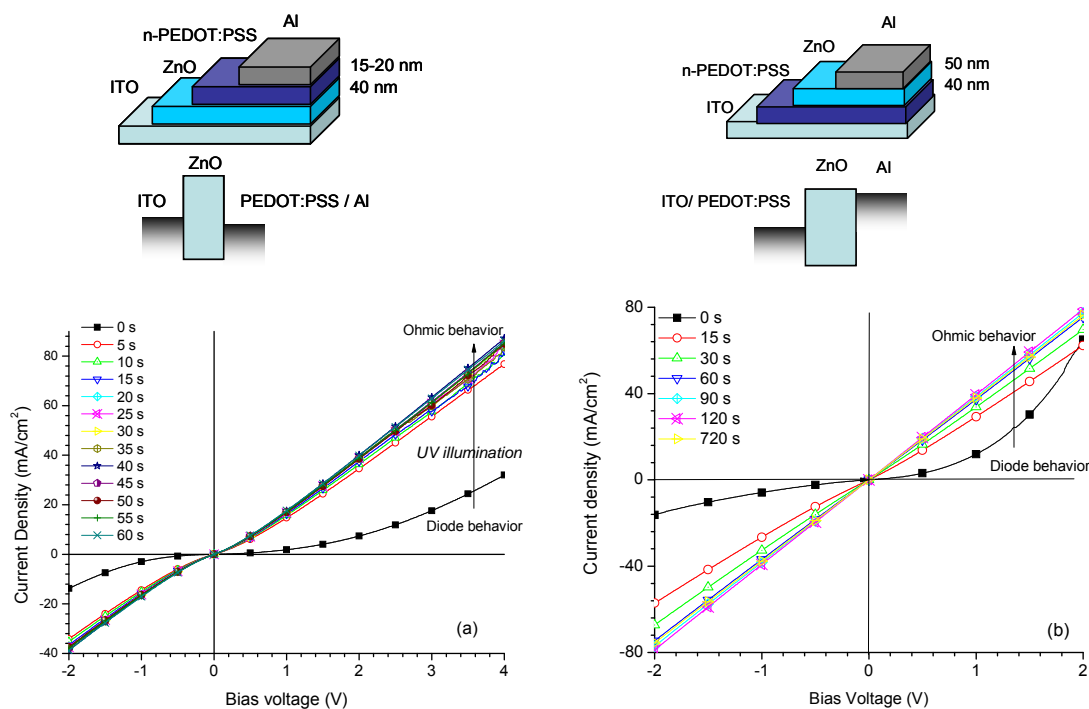


Figure 3: Diode setup and experimental current-voltage characteristics of ZnO/neutral-PEDOT:PSS interface in (a) n-p junction mode, and (b) p-n junction mode. The experiments explain the transition from diode behavior (Schottky contact) to Ohmic behavior upon UV-illumination.

8.3.2 Optical constants of layer of ZnO nanoparticles

Optical constants for a layer of ZnO nanoparticles on a Si wafer were determined in air by spectroscopic ellipsometry. While modeling the experimental data obtained from the ellipsometer for layer of ZnO nanoparticles, we assumed that the ZnO layer behaves as a homogeneous and isotropic material. An AFM image (Figure 4) shows that the surface of the ZnO layer is not completely flat and, hence, surface roughness has to be taken into account while modeling. The RMS value for surface roughness as determined from the AFM software was 10 nm.

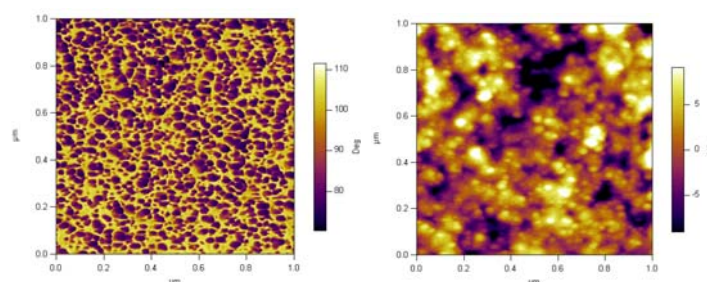


Figure 4: (a) Phase and (b) height image of a 35 nm thin film of ZnO nanoparticles on glass.

Crystalline ZnO is an anisotropic material with a hexagonal crystal structure and therefore one cannot a priori assume isotropic optical constants. However, transmission electron microscopy on the ZnO nanoparticles shows that they are approximately spherical in shape and, furthermore, the AFM image also does not show any deviations either from spherical

symmetry or of any preferential alignment. In addition, the dielectric functions for ZnO show only a very small variation for the different directions.¹⁹ Henceforth, an isotropic model would suffice to determine the optical constants ($\tilde{n} = n + i\kappa$).

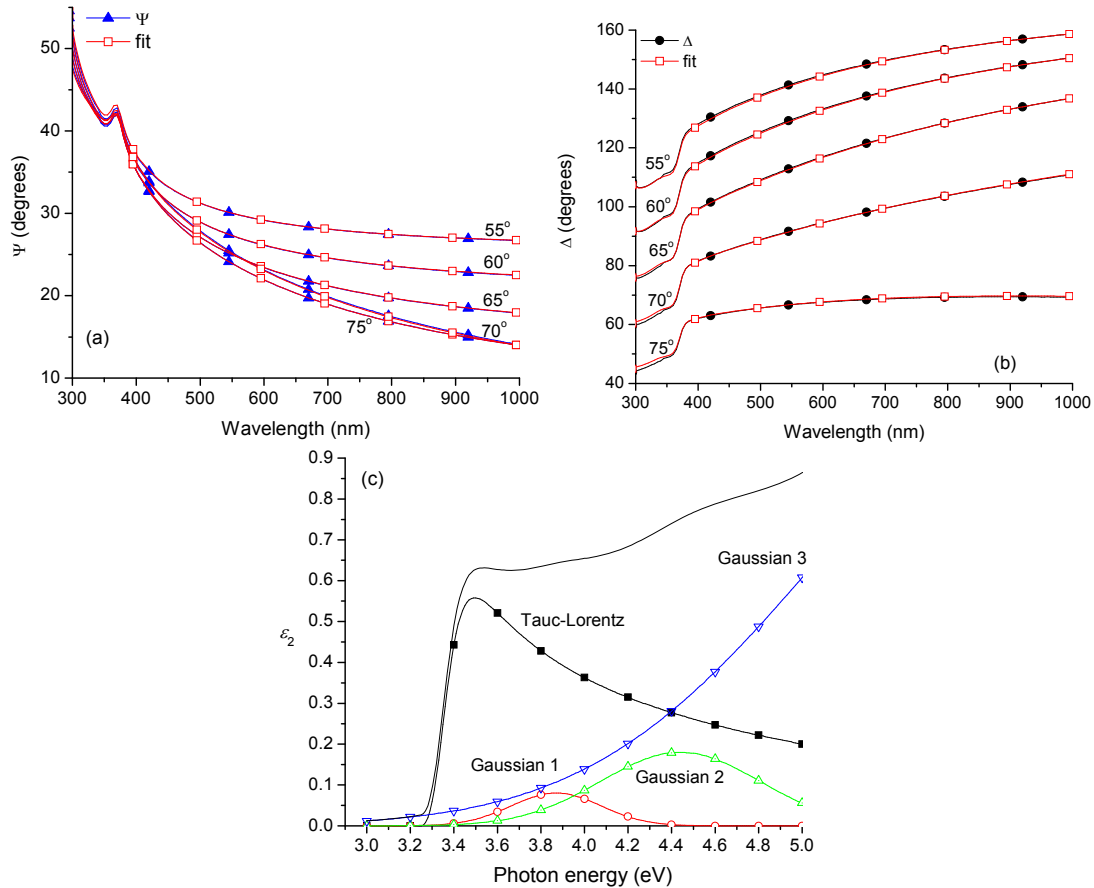


Figure 5: (a) Ψ and (b) Δ values recorded by the ellipsometer along with modeled fit for the thin film of ZnO nanoparticles on Si wafer at different angles of incidence. (c) Oscillators used to obtain the aforementioned fit. The thickness of the film as obtained from the surface profilometer is 35nm.

Results of the fits of the isotropic oscillator are also illustrated in Figure 5a and 5b. The fitting procedure is the same as explained in Chapter 7. First the transparent region was modeled as a Cauchy layer (as $\kappa = 0$) to determine thickness. Later, keeping thickness constant a point by point fit is made through the whole wavelength region. A rough estimate of optical constants is determined through this fit. This rough estimate is then used to set up a general oscillator model to describe the dielectric function. Here we use a summation of Gaussian oscillators and a Tauc-Lorentz²⁰ oscillator. Tauc-Lorentz is a useful oscillator model for semiconductors.

$$\varepsilon_2^{\text{TL}} = \begin{cases} \frac{AE_c B(E - E_g)^2}{(E^2 - E_c^2)^2 + B^2 E^2} \cdot \frac{1}{E} & E > E_g \\ 0 & E \leq E_g \end{cases} \quad (2)$$

$$\varepsilon_1^{\text{TL}} = \varepsilon_1(\infty) + \frac{2}{\pi} P \int_{E_g}^{\infty} \frac{\xi \varepsilon_2^{\text{TL}}(\xi)}{\xi^2 - E^2} d\xi$$

where A is a constant with energy units, B is energy band width at half maximum, E_c the resonance energy (peak transition energy), E_g the band gap energy (onset of absorbance), and $\varepsilon_1(\infty)$ is an additional fitting parameter. Here P stands for the Cauchy principal part of the integral.²¹ The real part of the Tauc-Lorentz can be found by a Kramers-Kronig transformation for the imaginary part, ε_2 . In addition to A , E_c , and B which are general variables used for fitting the experimental ψ and Δ values, Tauc-Lorentz involves two more in E_g and $\varepsilon_1(\infty)$.

Fitting for the variables (for example band energy, bandwidth, energy onset, amplitude) of all oscillators along with thickness and roughness for the sample, yielded a fit with a mean squared error (MSE) and correlation values. The oscillator strengths of the general oscillators used in the model to obtain the aforementioned fit are collected in Table 1 and shown in Figure 5c. The MSE obtained was 6.42 with correlation values as low as 0.83. The fits obtained adhere nicely to 90% confidence limits. The thickness determined by the ellipsometry experiments was found to be 37.8 nm which is in good accordance with thickness measured by surface profilometer (35 nm). The optical constants as obtained from the modeled fit of layer of ZnO nanoparticles are shown in Figure 6. The extinction coefficient, κ for the layer of ZnO nanoparticles shows onset at ~400 nm and a characteristic peak at ~375 nm. This is the absorption edge of the direct band gap semiconductor. A global roughness fit was performed. With the help of the Woollam WVASE32 software, surface roughness was fitted. This can be done by choosing roughness as a fitting parameter from the model options in the software. The software then treats the model as non ideal in nature and fits for average roughness. This technique was used throughout all experiments. For the layer of ZnO nanoparticles on Si, 18% roughness was found. Another way of treating surface roughness is by adding an additional layer on top of ZnO. This layer can be designed to comprise of voids as source for surface roughness. It was assumed the layer was made of 50% voids and the rest 50% were ZnO nanoparticles. The intermixing of the void and nanoparticles was based on effective medium approximation involving Bruggeman theory. The thickness of this intermix layer was an additional parameter during fitting of the experimental values. This method of roughness correction did give very similar results as obtained from global roughness in optical constants (Figure 6b).

Oscillators	$A(\text{eV})$	$B(\text{eV})$	$E_c(\text{eV})$
Tauc-Lorentz	72.88	0.26	3.34
Gaussian	0.04	0.49	3.87
Gaussian	0.15	0.86	4.44
Gaussian	2.52	2.43	6.07

Table 1: Fit parameters for oscillators used in the model for thin film of ZnO nps on Si, as derived from the solution set. Additional parameter for Tauc-Lorentz being (E_g 3.25 eV).

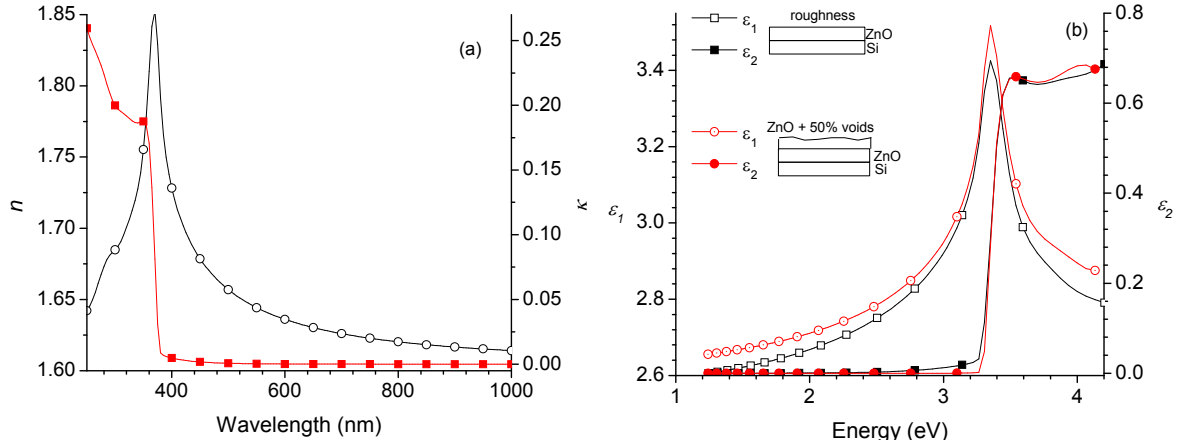


Figure 6: Optical constants (a) n and κ , and (b) ϵ_1 and ϵ_2 , values of thin film ZnO nanoparticles as derived from the model fit to experimental data shown in Figure 5. Panel (b) also shows influence of alternate methods of dealing with surface roughness.

The optical constants as shown in Figure 6 can be compared to those reported for crystalline ZnO.^{19,22} For this we calculated the dielectric spectrum $\epsilon(\nu) = \epsilon_1(\nu) + i\epsilon_2(\nu)$ and use the maximal slope of the rising flank of the $\epsilon_2(\nu)$ spectrum as a semi-empirical criterion to determine 3.38 eV as the energy of the onset of the interband transition.⁸ Using the same criterion we find for single crystalline ZnO a value of 3.31 eV for optical electric field perpendicular to the crystallographic c -axis and an onset at 3.34 eV for field parallel to the c -axis.^{19,22} The difference between the onset observed here and that reported for single crystalline ZnO may be interpreted in terms of a quantum confinement effect. Here the delocalization of the charge carriers is limited due to the finite radius of the ZnO nanocrystals in the film.²³ For ZnO particles with diameter of 5 nm quantum confinement is still relatively small and amounts to about 0.1 eV.²⁴ Apart from a relatively small difference in onset, the $\epsilon_1(\nu)$ and $\epsilon_2(\nu)$ spectra of the nanoparticle layer and of single crystalline ZnO differ considerably in amplitude. For single crystalline ZnO, $\epsilon_2(\nu)$ shows a sharp exciton feature at 3.45 eV where $\epsilon_2(\nu)$ reaches a maximum value of 2.8.²² The maximum amplitude of $\epsilon_2(\nu)$ has been shown to be very sensitive to the degree of crystallinity and decreases rapidly for multicrystalline films.¹⁹ Roughness in the films were found to have minimal effect on the dielectric constants in order to explain the difference in aforementioned amplitude. The multicrystalline nature of ZnO in spincoated films is most likely responsible for the lower amplitude in $\epsilon_2(\nu)$.

8.3.3 Optical constants of layer of ZnO nanoparticles upon UV illumination (photodoping)

Illuminating the layer of ZnO nanoparticles with UV light (365 nm wavelength) in argon atmosphere results in changes in the ψ and Δ (Figure 7). The position of the local maximum of ψ values near 375 nm shifts towards shorter wavelength to 360 nm and increases upto 42° upon UV illumination (Figure 7b). The magnitude of the shifts increases with illumination time but saturates after 1 h. Upon introduction of air into the sample chamber the changes are fully reversed and the original ψ and Δ values are recovered. This observation is well in agreement with the scheme as proposed in Figure 2.

By modeling ψ and Δ after illumination, the changes in optical constants induced by UV light can be resolved (Figure 8). The n and κ spectra clearly show a blue shift of the onset of the absorption upon UV illumination, corresponding to the expected behavior for the Moss-Burstein effect. UV illumination in inert atmosphere leads to population of the conduction band with mobile electrons because the mobile holes recombine with O_2^- at the surface. These mobile electrons are scavenged again upon exposure to O_2 from the air and the Moss-Burstein shift is reversed. Here we notice a reduction of n upon illumination at in the 1200-1700 nm region (Figure 9a). This indicates a possible rise of the absorption at wavelengths > 1700 nm where ZnO free carriers are known to absorb,²⁵ of which the onset is already observable at around 1200nm.

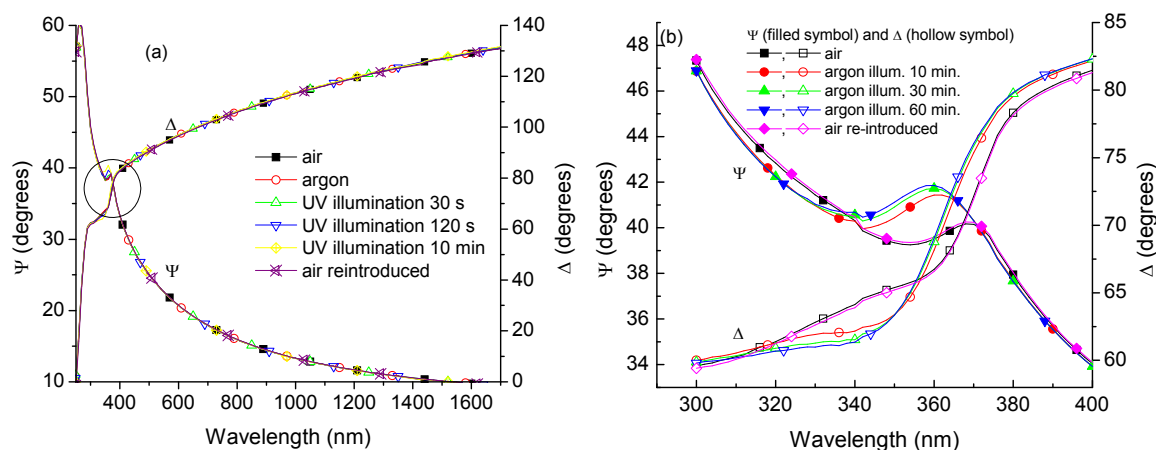


Figure 7: Ψ and Δ values recorded by the ellipsometer for the thin film of ZnO nps on Si wafer at 70° angle of incidence. Figure b is the magnified version of the circled part in Figure a.

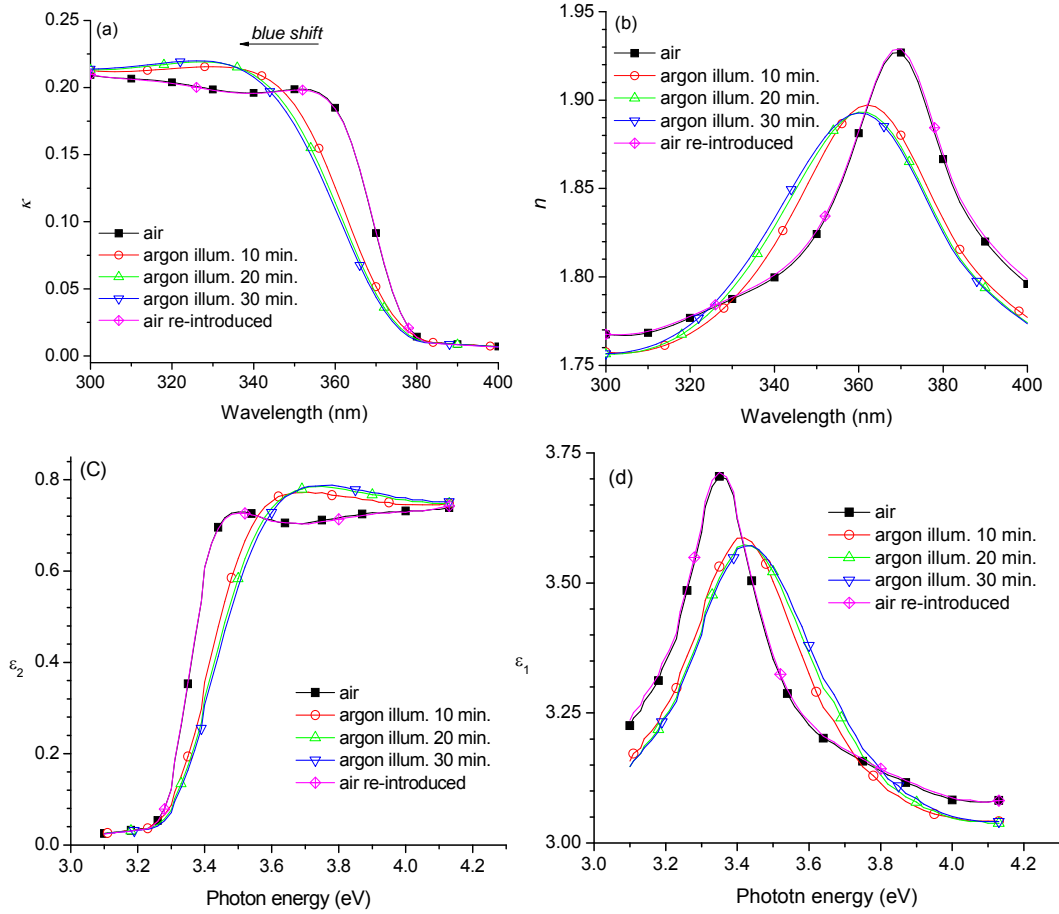


Figure 8: (a) κ , (b) n , (c) ε_2 , and (d) ε_1 values for layer of ZnO nanoparticles before and after UV illumination.

The changes in optical constants saturate for long illumination times (Figure 9b). With illumination at 365 nm, saturation seems to be reached more slowly in comparison with illumination at 254 nm. This is probably related to differences in intensity of the radiation used and differences in the absorption by the ZnO. As a control experiment we verified that the UV illumination does not cause a change in the optical properties of the underlying Si substrate (Figure 9c). In addition it was also verified that only changing the atmosphere from air to argon without illumination with UV light does not affect the optical constants of ZnO.

We can now try to estimate the magnitude of the Moss-Burstein shift using the criterion for determining the onset of absorption from the $\varepsilon_2(\nu)$ spectrum (Figure 8c). We find that the point of maximal slope shifts over 0.07 eV after illumination. By comparing with the magnitude of the Moss-Burstein shift reported by Kim and Park for ZnO doped with different amounts of Al,⁹ we estimate that the density of mobile electrons in the valence band ZnO nanoparticles layer is $\sim 2 \times 10^{19}/\text{cm}^3$. The same conclusion is reached after comparison with other studies on the magnitude of the Moss-Burstein shift with respect to the density of the dopants.^{8,10} We interpret this high doping level reached upon illumination in terms of the granular structure of the ZnO layer. O₂ molecules may be able to diffuse in and out of the layer via the amorphous material and empty space between the nanoparticles, which results in a high internal surface area of the ZnO layer available for adsorption of O₂ molecules and

trapping of mobile electrons. A doping level of $2 \times 10^{19}/\text{cm}^3$ implies a density of positively charged defects in the ZnO of at least equal magnitude. This number density corresponds to about one positively charged defect per nanoparticle. Considering the fact that these particles were synthesized in solution this number density does not necessarily imply multiple charging of the particles during their formation.

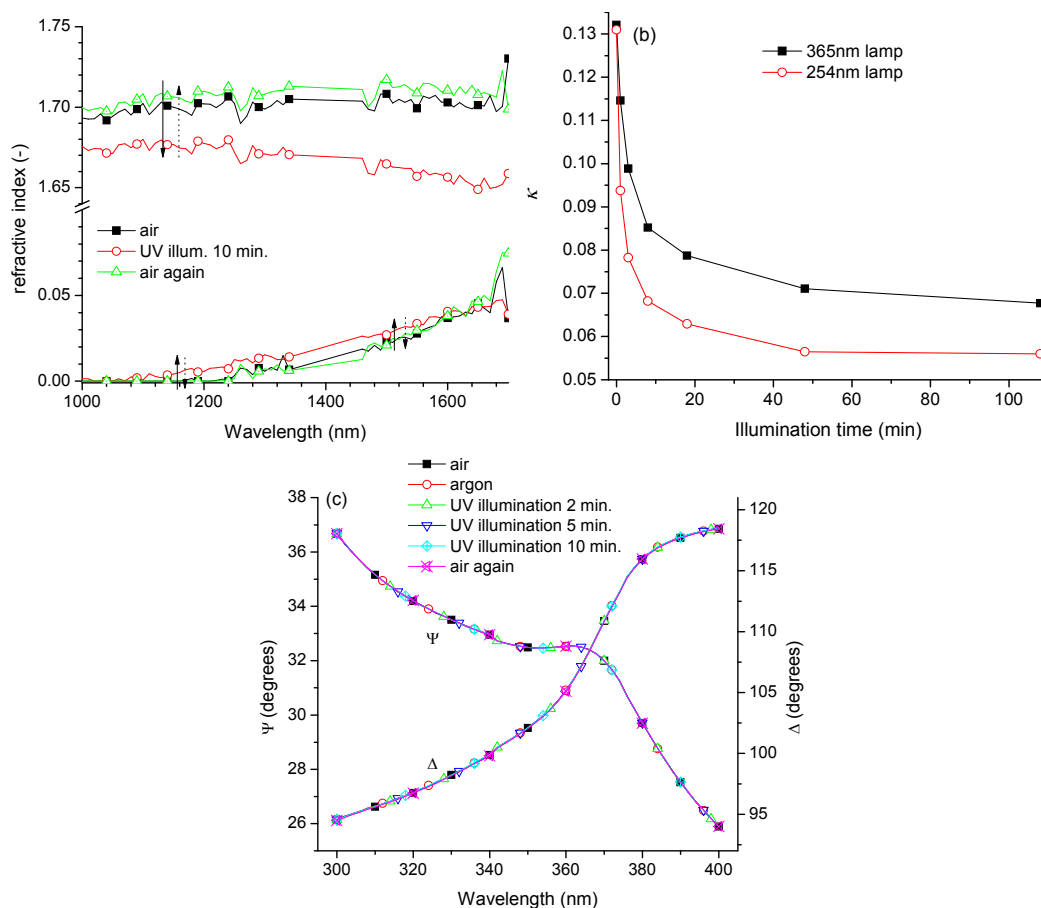


Figure 9: (a) n and κ values for layer of ZnO nanoparticles before and after UV illumination in infrared wavelength region. (b) change on optical constants monitored at 366nm using two different illumination wavelengths. (c) Ψ and Δ values recorded by the ellipsometer for the thin film of SiO₂ on Si wafer at 70° angle of incidence.

8.3.4 Anisotropic optical constants of PEDOT:PSS

In order to be able to study electron transfer processes in the ZnO/PEDOT:PSS junction spectroscopically, it is important to first determine the optical constants of PEDOT:PSS. To this end we investigated layers of PEDOT:PSS on glass. We studied the pH-neutral and acidic forms.

Optical properties of the acidic PEDOT:PSS have been reported in literature.²⁶ They are found to be anisotropic in nature. Therefore when studying the neutral-PEDOT:PSS, for which optical constants are not available from literature, we take anisotropy into account. The ellipsometric angles ψ and Δ are shown in Figure 10 together with the fit of an appropriate anisotropic oscillator model. To validate the results on the neutral-PEDOT:PSS and obtain a

fair comparison with the properties of the acidic PEDOT:PSS, we have also studied the acidic variant using the same conditions. The optical constants obtained are shown in Figures 10c (acidic) and 10d (pH neutral). Optimized parameters of the oscillator model fitted to the data are listed in Table 2. The thicknesses of the layers found from ellipsometric analysis were in accordance with those determined from surface profilometer (18.2 nm from ellipsometry on neutral-PEDOT:PSS vs. ~ 15 nm from profilometer). For acidic corresponding values are 13.6 vs. ~ 15 nm.

It can be seen that for both PEDOT:PSS films, the ordinary (in-plane) component of the refractive index is much larger than the extraordinary (out-of-plane). As the transition dipole moment for the strongly allowed low energy transitions are usually oriented parallel to the chain direction in π -conjugated polymers, this anisotropy suggests a preferential in-plane orientation of polymer chains. Looking at the spectrum for $\kappa(\lambda)$ for neutral-PEDOT:PSS, we notice a shoulder in the ordinary component position centered around 800 nm which is largely absent in the acidic form. This band has been assigned to an interband transition.²⁷

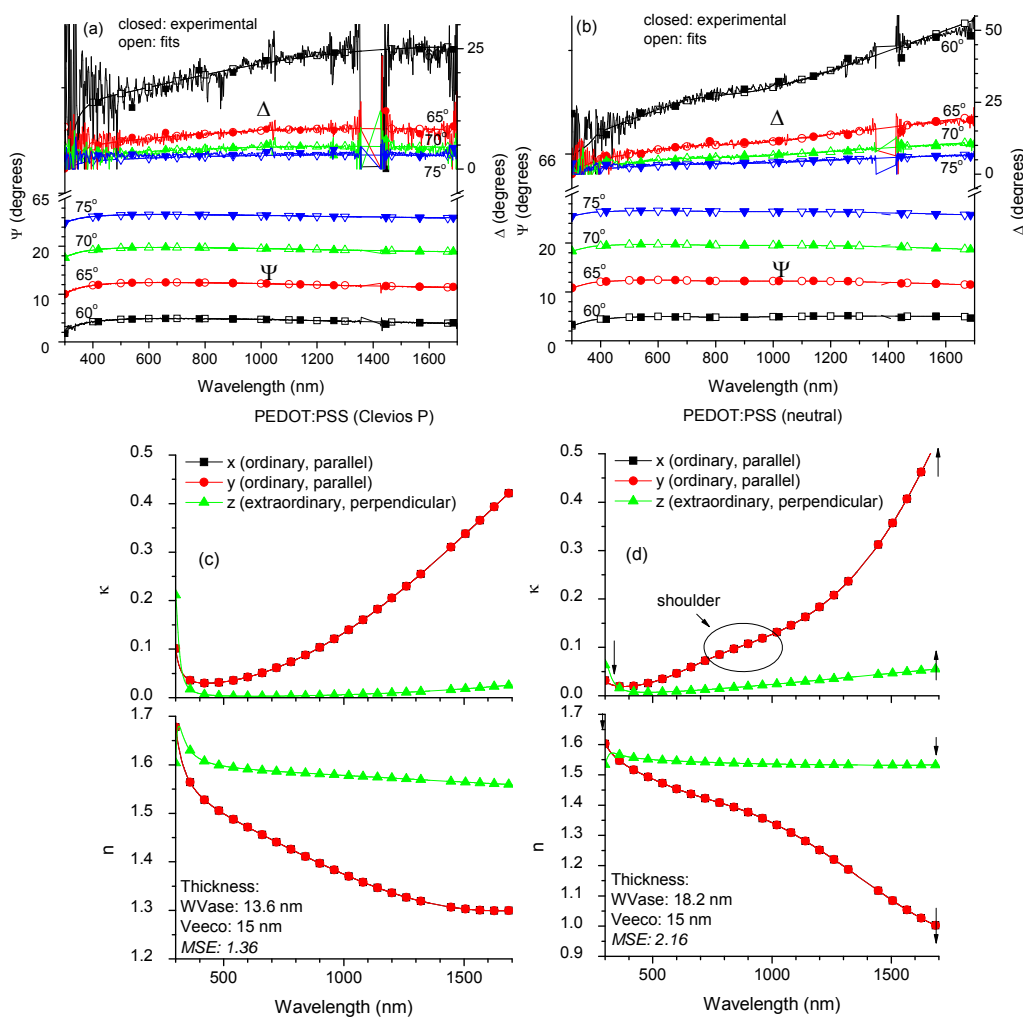


Figure 10: ψ and Δ values combined with the modeled fits for thin films of (a) PEDOT:PSS (Clevios P), and (b) neutral- PEDOT:PSS on glass substrates. (c) and (d) spectrum show anisotropic optical constants for the same respectively.

Oscillators	PEDOT:PSS (Clevios P)			neutral-PEDOT:PSS(Orgacon)		
	$A(\text{eV})$	$B(\text{eV})$	$E_c(\text{eV})$	$A(\text{eV})$	$B(\text{eV})$	$E_c(\text{eV})$
Lorentz (ordinary)	0.81	0.45	4.64	1.16	0.53	5.42
Lorentz (ordinary)	4.81	0.86	0.23	3.73	0.35	0.28
Lorentz (ordinary)	0.21	7.88	5.46	0.20	1.5	1.6
Lorentz (extraordinary)	0.29	0.43	4.16	0.13	0.69	4.1
Lorentz (extraordinary)	0.19	0.46	0.35	0.57	1.42	0.35

Table 2: Parameters describing the individual oscillators contributing to $\varepsilon_2(\nu)$ in the model used to fit the ellipsometric angles for thin films of PEDOT:PSS and neutral-PEDOT:PSS on glass substrate.

8.3.5 Influence of UV illumination on pH-neutral PEDOT:PSS

As part of a control experiment, it is important to determine the effect of UV illumination on neutral-PEDOT:PSS in inert atmosphere. Figure 11a reveals the experimental ψ and Δ values. The optical constants n and κ do not change significantly upon UV-illumination as can be seen from Figure 11b and 11c. There is a very small change when argon is introduced. This is because of the fact that air and moisture are extracted from the sample cell thereby drying the neutral-PEDOT:PSS layer, which generally contains a significant amount of water.

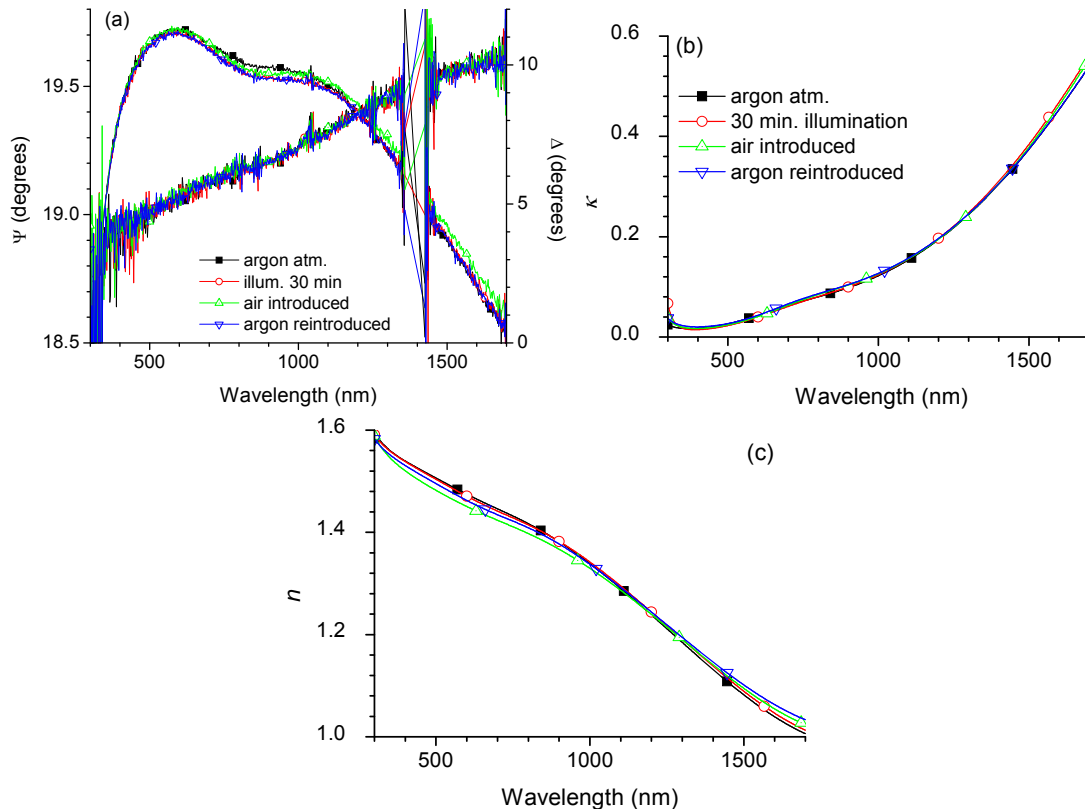


Figure 11: (a) ψ and Δ values for thin film of neutral-PEDOT:PSS on glass substrates at fixed angle of 70° together with optical constants (b ,c) as obtained from the model fit to the experimental ψ and Δ values for different conditions.

8.3.6 Photodoping at ZnO nanoparticles/neutral-PEDOT:PSS interface

After obtaining the optical constants of layers of ZnO nanoparticles and neutral-PEDOT:PSS, the next step is to investigate the bilayer of these two materials. The stack investigated by ellipsometry at different angles was glass/ZnO(100nm)/neutral-PEDOT:PSS(15 nm). To model the experiments, oscillators from the previous experiments (where each layer was treated independently) were taken. All parameters in every oscillator for effective three layers (ZnO, ordinary neutral-PEDOT:PSS and extraordinary neutral-PEDOT:PSS) including the thickness were fitted. Results in terms of optical constants are shown in Figure 12. These optical constants have similar band shapes but only differ by 10% in amplitude to their respective values as individual layers. These amplitude differences can be due to intermixing of the layers at the interface, which affects morphology compared to individual layers.

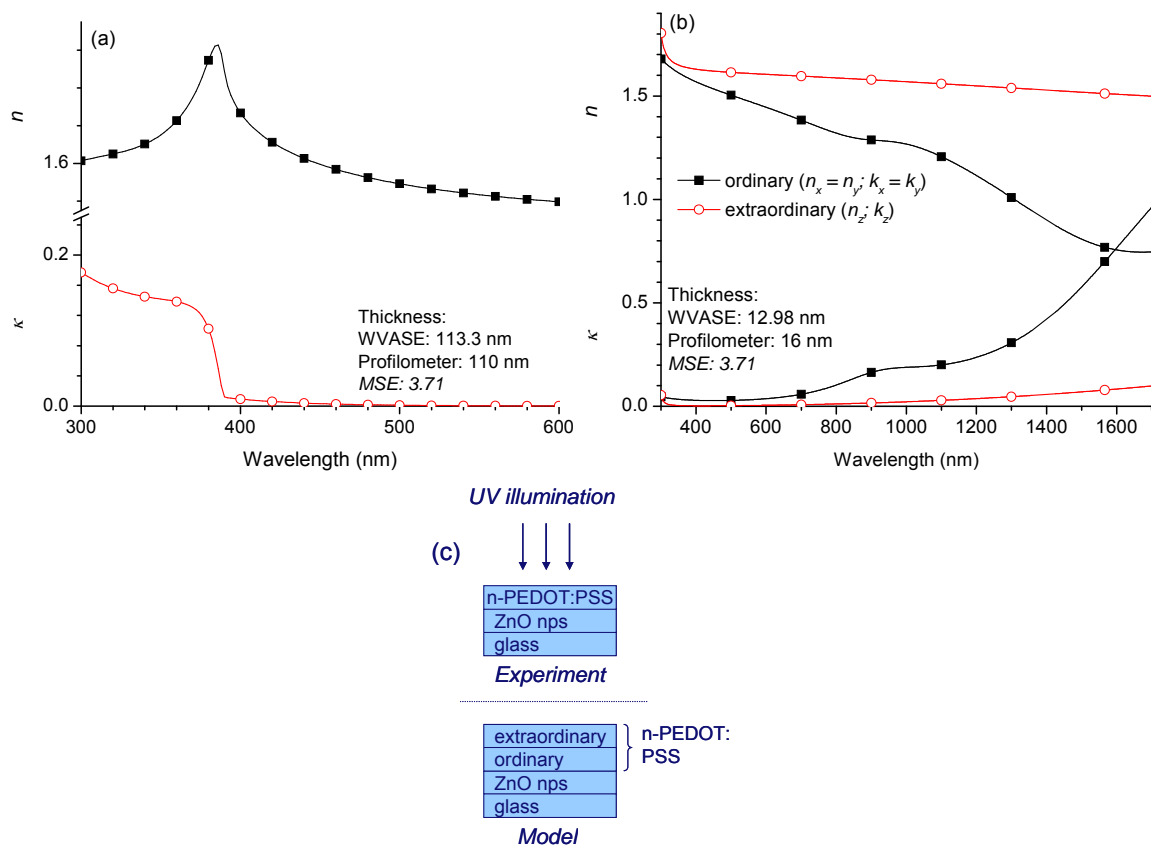


Figure 12: Individual optical constants of (a) layer of ZnO nps, and (b) neutral-PEDOT:PSS as obtained from the model fit to the experimental ψ and Δ values for the bilayer film Glass/ZnO(100nm)/neutral-PEDOT:PSS(15nm). (c) Representation of layers as treated in the experiments and the model during UV illumination experiments.

The measurements and analysis were then repeated for UV illumination experiments on the bilayer in inert atmosphere. Here UV light was incident on the neutral-PEDOT:PSS and air interface. Changes in ψ and Δ values are observed and shown in Figure 13. In the wavelength

region of ZnO absorption, we notice a small shift in the peak of ψ around 375 nm to shorter wavelength upon illumination. This shift reverses upon exposure to air. This behavior is similar to that observed for a layer of ZnO nanoparticles on Si (paragraph 8.3.3).

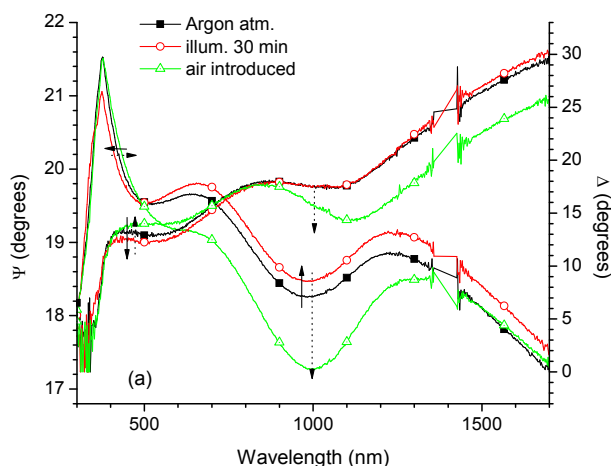


Figure 13: Change in ψ and Δ values for thin film of (a) ZnO(100nm)/neutral-PEDOT:PSS(15nm) at fixed angle of 70° . The solid arrows indicate the direction of change upon illumination in inert atmosphere (90 minute purging with argon) whereas dotted arrow shows changes occurring upon introduction of air after illumination

In the wavelength region where neutral-PEDOT:PSS absorbs light (700-1550 nm) we also observe changes in the ψ and Δ values upon illumination. Remarkably though in this wavelength region, the separate layers of ZnO and neutral-PEDOT:PSS show no appreciable change in ellipsometric response upon illumination (paragraphs 8.3.3 and 8.3.5). Changes observed in this region are not reversible upon exposure to air.

The changes in ψ and Δ were modeled to determine changes in the optical constants. In these calculations, the thickness was taken as a constant and invariant to illumination. The oscillator variables for in-plane refractive index of neutral-PEDOT:PSS and ZnO nanoparticles were used as fitting parameters to record changes upon UV-illumination. Because measurements were only possible at a fixed angle of 70° , limited data on the out-of-plane optical constants of neutral-PEDOT:PSS could be obtained, hence the variables of the associated oscillators were not deployed as fitting parameters.

Figure 14a shows that the Moss-Burstein shift still occurs in the layer of ZnO nanoparticles and that the effect is reversed upon introduction of air. This is probably because the expected depletion width is much smaller than the thickness of the ZnO film (100 nm).

Changes can also be seen in optical constants of neutral-PEDOT:PSS upon UV illumination which otherwise were absent when illumination experiments were carried out on individual layer of neutral-PEDOT:PSS (see section 8.3.5). These observations are indicative of charge transfer happening at the ZnO/neutral-PEDOT:PSS junction. Upon UV illumination, the electrons that are promoted to the conduction band of ZnO are transferred to lower lying energy levels of neutral-PEDOT:PSS. These electrons combine with the holes in the doped neutral-PEDOT:PSS and reducing the polymer. A decrease in κ value in the interband region

at ~ 900 nm of neutral-PEDOT:PSS (Figure 14b) indicates that some reduction of PEDOT occurs.²

Upon introduction of air the Moss-Burstein shift in ZnO is reversed and the κ value of neutral-PEDOT:PSS at 900 nm is restored. This is consistent with the re-oxidation of neutral-PEDOT:PSS, but the optical constants of neutral-PEDOT:PSS above 1000 nm have changed irreversibly (Figure 14b). The origin of these irreversible changes is unknown. Introducing argon at this stage did not change the optical constants.

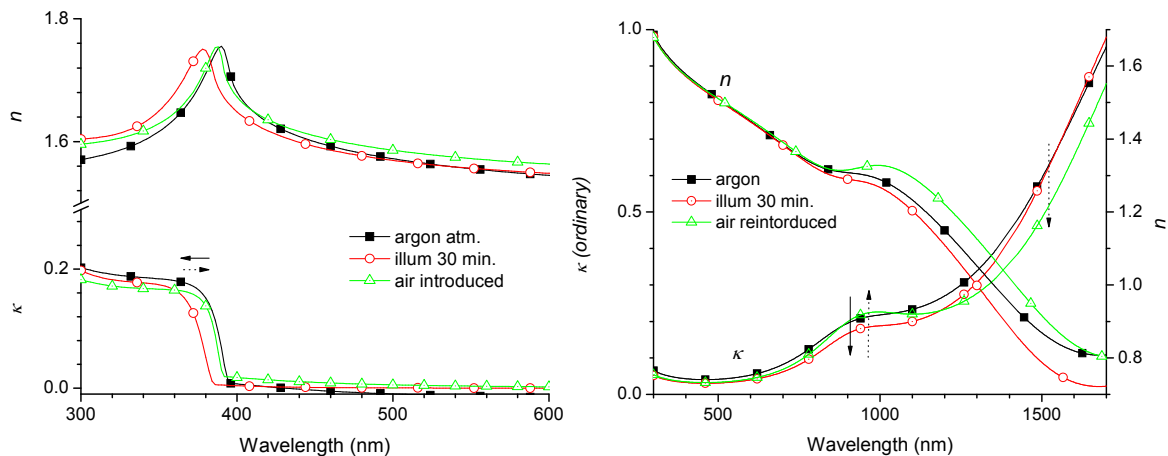


Figure 14: Optical constants of (a) layer of ZnO nps, and (b) neutral-PEDOT:PSS upon UV-illumination, as obtained from the model fit to the experimental ψ and Δ values for the ZnO(100nm) /neutral-PEDOT:PSS(15nm) film on glass substrates as shown in Figure 13. The solid arrows indicate the direction of change upon illumination in inert atmosphere (90 minute purging with argon) whereas dotted arrow shows changes occurring upon introduction of air after illumination

8.3.7 Estimation of a lower limit of the charge carrier density from Kelvin probe experiments

In order to confirm the high doping levels after illumination determined from ellipsometry, we performed Kelvin probe measurements. Here one measures the surface potential of the ZnO layer before and after illumination. For these measurements, the particles are spin coated on an ITO layer which serves as the back electrode in the Kelvin probe measurements.

In Figure 15 we have illustrated this type of measurement schematically. For simplicity we assume that the ITO substrate and the metallic probe head have the same work function. This is allowed because we are only interested in changes of the work function after illumination. Before illumination, the ZnO may be assumed to behave as an intrinsic wide band gap semiconductor. In this case, the electrical current flowing between the probe head and the ITO electrode through the external circuit upon moving the probe head to and from the ITO substrate is minimal when zero bias voltage is applied between ITO and the probe head. After UV illumination under O_2 -free conditions, free carriers are induced in the ZnO that equilibrate. Some of these migrate to the ITO electrode. This migration induces a net space charge in the ZnO which leads to a shift of the vacuum level. The migration stops when the

conduction band of the ZnO is aligned with the Fermi level of the ITO. Under these conditions, the current between probe head and ITO electrode is minimal while the potential difference (ΔV) arising from electron migration from ZnO to ITO is compensated in the external circuit of the setup.

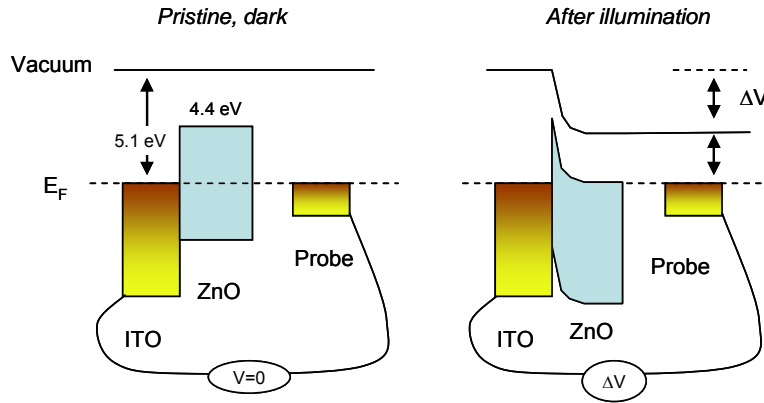


Figure 15: Band diagram illustrating the Kelvin probe experiments on ITO/ ZnO structures before (left) and after illumination. For simplicity it is assumed that the vibrating probe head has the same work function as ITO.

Based on a rough estimate of the work function of ITO (~ 5.1 eV) and the position of the conduction band edge of ZnO with respect to the vacuum level (4.4 eV), one expects a change in the work function of 0.7 eV. Here we assume of course that the charge carrier density in the ZnO is high enough for the potential difference ΔV to be reached within the finite thickness of the ZnO layer. Now by varying the thickness of the ZnO layer and measuring the change in surface potential upon illumination we can estimate a lower limit for the charge carrier density in the ZnO after photodoping.

The problem of calculating the surface potential in these planar junctions may be reduced to one spatial dimension (perpendicular to the layers). In this case the Poisson equation that relates the space charge density ρ to the derivative of the electric field E is:

$$\frac{d}{dx} E = \frac{\rho}{\epsilon_0 \epsilon_r} \quad (3)$$

If we now assume complete ionization of the donors in the depletion zone of the photodoped ZnO near the interface, *e.g.* a rectangular ionization profile, we can calculate the minimal layer thickness d that is needed to make up the potential difference ΔV for a given value of the donor density ρ

$$\Delta V(d) = \int_0^d E(x) dx = \int_0^d \frac{\rho}{\epsilon_0 \epsilon_r} \cdot x dx = \frac{\rho}{\epsilon_0 \epsilon_r} \cdot \frac{d^2}{2} \quad (4)$$

Kelvin probe experiments of a layer of 40 nm thickness yielded a change in the work function of 0.7 V upon illumination in O₂-free atmosphere. Upon exposure to O₂ the work function reverted back to its original value. Experiments on a layer of 25 nm thickness, which is practically the lower limit for obtaining continuous films, yielded a shift of the surface voltage of 0.55 V upon illumination.

Using the latter experimental numbers and a static relative dielectric constant of ZnO of 8.5, we estimate a lower limit for the charge carrier density in the photodoped ZnO of 10^{18} /cm³. For the data on the film with 40 nm thickness we calculate a lower limit of 4×10^{17} /cm³. These lower limits are in agreement with the estimate of the charge carrier density from analysis of the Moss-Burstein shift. We note however that the estimate from spectroscopic analysis is much higher (2×10^{19} /cm³).

Now using eq 4 we can estimate the depletion width of the ZnO/PEDOT:PSS junction. For this we assume a work function of the PEDOT:PSS of 5.2 eV. This gives an estimate of the depletion width of $d_{\text{ZnO}} \approx 5$ nm. Although this is a short distance, it is still quite long compared to the distances for fast tunneling of charge carriers. We note that the Debye length L_D for the doped ZnO (0.8 nm) is much smaller than the estimated depletion width for the junction. Therefore the potential barrier than a charge carrier has to overcome will be screened significantly by the surrounding charge carriers and efficient tunneling of charge carriers may be expected. Debye length can be calculated as mentioned below:

$$L_D = \left(\frac{\epsilon_r \epsilon_0 k_b T}{q^2 N_0} \right)^{1/2} \quad (5)$$

where, k_b is the Boltzmann constant, T is the temperature, and N_0 is the charge carrier density.

Furthermore we point out that the net positive charge in the ZnO responsible for the band bending is not a continuous charge density but point like due to the atomic nature of the dopants. This gives much higher local charge densities and suggests that charge transfer across the ZnO/PEDOT:PSS interface actually occurs via positively charged ions (or vacancies) at the interface serving as a point of entry for the electrons into the ZnO.

Based on the estimates of the charge carrier density in photodoped ZnO we can now predict what happens in a isolated bilayer structure of PEDOT:PSS and ZnO upon photoillumination. Upon photodoping the ZnO we expect charge transfer of electrons from the ZnO to PEDOT:PSS across the interface. The number of charge carriers transferred per unit area interface is equal to $\rho_{\text{ZnO}} \cdot d_{\text{ZnO}} = 10^{13}$ / cm². If the PEDOT:PSS layer has a thickness $l_{\text{PEDOT}} = 15$ nm, this will result a average number density of transferred charges in the PEDOT:PSS layer equal to $\rho_{\text{ZnO}} \cdot d_{\text{ZnO}} / l_{\text{PEDOT}} = 7 \times 10^{18}$ /cm³. This number may be compared to the total charge carrier density in PEDOT:PSS which is estimated at 10^{21} /cm³.²⁸ This implies a very small fractional change in the charge carrier density in the PEDOT:PSS layer upon photoillumination of a ZnO/PEDOT:PSS junction. Nevertheless, as described above, we still

find spectroscopic support for charge transfer of electrons from ZnO to PEDOT:PSS upon photoillumination.

8.4 Conclusion

The optical constants for a layer of ZnO nanoparticles were determined *via* variable angle spectroscopic ellipsometry. Upon photodoping the layer in inert (oxygen-free) atmosphere, a Moss-Burstein shift is observed in the optical constants. This shift is associated to apparent increase in band gap, which results due to population of conduction band with electrons excited from valence band of ZnO. These free electrons in the conduction band account for increased conductivity in the layer of ZnO nanoparticles explaining its Ohmic behavior. The free charge carrier density corresponding to this shift was estimated to be $2 \times 10^{19} / \text{cm}^3$. The shift can be reversed on introduction of air.

On UV illuminating the n-p junction of ZnO/neutral-PEDOT:PSS, it was observed that the free charge carriers generated in the conduction band of ZnO are transferred to neutral-PEDOT:PSS. The depletion width in the layer of ZnO for this quasi-ohmic p-n junction was estimated to be 5 nm. Though the estimated number density of transferred charges is fairly low to significantly reduce the heavily doped neutral-PEDOT:PSS, yet changes in ψ and Δ values were detected using spectroscopic ellipsometry. This suggests slight reduction of neutral-PEDOT:PSS. For the ZnO layer of the junction, a reversible Moss-Burstein is observed as expected for a ZnO film with thickness greater than the depletion width.

References

1. Sze, S. M. *Physics of semiconductor devices*, Wiley-Interscience, **1981**, 513.
2. (a) Groenendaal, L.; Jonas, F.; Freitag, D.; Pielartzik, H.; Reynolds, J.R. *Adv. Mater.* **2000**, *12*, 481. (b) Dietrich, M.; Heinze, J.; Heywang G.; Jonas, F.; *J. Electrochem. Soc.* **1994**, *369*, 87. (c) Pei, Q.B.; Zuccarello, G.; Ahlskog, M.; Inganäs, O. *Polymer* **1994**, *35*, 1347.
3. Verbakel, F.; Meskers, S.C.J.; Janssen, R.A.J. *J. Appl. Phys.* **2007**, *102*, 83701.
4. Verbakel, F.; Meskers, S.C.J.; Janssen, R.A.J. *Appl. Phys. Lett.* **2007**, *91*, 192103.
5. Gilot, J.; Wienk, M.M.; Janssen, R.A.J. *Appl. Phys. Lett.* **2007**, *90*, 143512.
6. Kim, J.Y.; Lee, K.; Coates, N.E.; Moses, D.; Nguyen, T.-Q.; Dante, M.; Heeger, A.J. *Science* **2007**, *317*, 222.
7. Collins R.J., Thomas D.G. *Phys. Rev.* **1958**, *112*, 388.
8. Roth, A.P.; Webb, J.B. ; Williams, D.F. *Solid State Commun.* **1981**, *39*, 1269.
9. Kim, K.J.; Park, Y.R. *Appl. Phys. Lett.* **2001**, *78*, 475.
10. Lu, J.G.; Fujita, S.; Kawaharamura, T.; Nishinaka, H.; Kamada, Y.; Ohshima, T.; Ye, Z.Z.; Zeng, Y.J.; Zhang, Y.Z.; Zhu, L.P.; He, H.P.; Zhao, B.H. *J. Appl. Phys.* **2007**, *101*, 083705.
11. Filipchenko, A.S.; Nasledov, D.N.; Radaikina, L.N.; Ratner, I.I. *Phys. Stat. Sol.* **1972**, *14*, 71.
12. (a) Burstein, E. *Phys. Rev.* **1954**, *93*, 632. (b) Moss, T.S. *Proc. Phys. Soc.(London)* **1954**, *B76*, 775.
13. Liu, W.K.; Whitaker, K.M.; Kittilstved, K.R.; Gamelin, D.R. *J. Am. Chem. Soc.* **2006**, *128*, 3910.
14. Zhou, X.H.; Hu, Q.-H.; Fu, Y. *J. Appl. Phys.* **2008**, *104*, 063703.
15. Sernelius, S.E.; Berggren, K.F.; Jin, Z.C.; Hamberg, I.; Granqvist, C.G. *Phys. Rev. B* **1988**, *37*, 10244.
16. Beek, W.J.E.; Wienk, M.M.; Kemerink, M.; Yang, X.; Janssen, R.A.J. *J. Phys. Chem. B*, **2005**, *109*, 9505.

17. WAVSE manual.
18. Hansen, W.N.; Hansen, G.J. *Surf. Sci.* **2001**, *481*, 172.
19. Yoshikawa, H.; Adachi, S. *Jpn. J. Appl. Phys.* **1997**, *36*, 6237.
20. Jellison Jr, G.E.; Modine, F.A. *Appl. Phys. Lett.* **1996**, *69*, 371.
21. Paget, D.F.; Elliott, D. *Numer. Math.* **1972**, *19*, 373.
22. Malandrino, G.; Blandino, M.; Fragala, M.E.; Losurdo, M.; Bruno, G. *J. Phys. Chem. C*, **2008**, *112* 9595.
23. Shim M, Guyot-Sionnest, P. *J. Am. Chem. Soc.* **2001**, *123*, 11651.
24. Meulenkaamp, E.A. *J. Phys. Chem. B.* **1998**, *102*, 5566.
25. Liu, W.K.; Whitaker, K.M.; Kittilstved K.R.; Gamelin, D.R. *J. Am. Chem. Soc.* **2006**, *128*, 3910.
26. (a) Pettersson, L.A.A.; Carlsson, F.; Inganäs, O.; Arwin, H. *Thin Solid Films* **1998**, *313-314*, 356. (b) Pettersson, L.A.A.; Ghosh, S.; Inganäs, O. *Org. Electron.* **2002**, *3*, 143.
27. (a) Chang, Y.; Lee, K.; Kiebooms, R.; Aleshin, A.; Heeger, A.J. *Synth. Met.* **1999**, *105*, 203. (b) Heywang, G.; Jonas, F. *Adv. Mater.* **1992**, *4*, 116. (c) Dietrich, M.; Heinze, J.; Heywang, G.; Jonas, F.; *J. Electroanal. Chem.* **1994**, *369*, 87. (d) Pei, Q.; Zuccarello, G.; Ahlskog, M.; Inganäs, O. *Polymer* **1994**, *35*, 1347.
28. Kiebooms, R.; Aleshin, A.; Hutchison, K.; Wudl, F. *J. Phys. Chem. B* **1997**, *101*, 11037.

Conclusion

Chapter 1, page 9: “*The aim of the thesis is to use circularly polarized light as a spectroscopic tool to understand the molecular organization associated to the chiroptical properties of conjugate polymers at various structural levels*”

To answer the above question, the thesis is structured into several chapters. *Chiral* π -conjugated polymers –especially chiral polyfluorene– are studied in great detail. *Chirality* serves mainly as a spectroscopic ‘label’ allowing us to investigate aggregation and chiroptical properties of the polymer chains using circular dichroism (CD) spectroscopy. CD spectroscopy allows us to study differential absorption between left and right handed circularly polarized light. The dissymmetry ratio in absorbance is often termed as g_{abs} . However, before looking deeply into the molecular organization associated to chiroptical properties of π -conjugated polymers, the foremost step is to define the chiroptical properties which are inherent to a material. Chiroptical properties that are independent to the amount of material are regarded as *intensive*, whereas properties dependent on the amount of the material are attributed as *extensive* properties. In order to define intensive properties of chiral conjugated polymers, we take chiral polythiophene as an example. The g_{abs} values for the films of the chiral polymer were found to be independent of film thickness. Thus g_{abs} can be regarded as the intensive property of the material. Hence, circular polarization in absorbance can be associated to arise on a molecular level at the site of photon absorbance.

Taking a step further, similar experiments were performed on chiral polyfluorene with an aim to first establish the intensive property and second to investigate its origin. Also in pristine films of a chiral polyfluorene we established that g_{abs} is an intensive property, that arises at a length scale $< 50\text{nm}$. These intensive effects seem common for unannealed films, where little or no long range order might be expected. With the help of AFM, the presence of a fibrillar structure could be associated with the origin of CD. These fibrils lie in the plane of the film. Spectroscopic ellipsometry (SE) reveals anisotropy in the films and it is found that the majority of polymer chains lie in the plane of the film. A helical arrangement of the coplanar chains across the sub-planes results in coupling between the transition dipole moments of the chains, giving rise to the CD. Such an arrangement results in non-zero off diagonal matrix elements, G_{12} in the anisotropic dielectric tensor of the polymer film determined from the CD and SE. These non-zero values of G_{12} have been related to optical rotation and ellipticity in reflection of light in a particular theory. Though the circular selectivity in reflection is predicted to be quite small and unlikely causes aberrations in CD, its existence is of paramount importance in defining the true nature of CD effects for chiral

polymer films in general. A possible follow up to these experiments would be to determine the value of G_{12} directly from the reflection measurements.

On annealing the films of chiral polyfluorene, g_{abs} is found to dependent on the film thickness. g_{abs} for annealed films of chiral polyfluorene can be associated as an extensive property arising at length scale > 50 nm. The extensive property is a result of long range mesoscopic ordering within the film. At even larger length scales, for example $1 \mu\text{m}$ thick annealed films, these extensive properties could be translated to circular selective scattering in region of no absorbance ($\lambda > 450$ nm). The multidomain nature of the film causes light scattering in the film and the dissymmetry ratio in scattering of left and right handed circularly polarized light contributes to *apparent* CD in this wavelength region. Additionally, the CD signal associated to the long range ordering in the circular differential absorbance in the *electronic ground states* of chiral polyfluorene also extends to a large monosignate photoinduced CD (PICD) associated with the triplet-triplet transition in the *excited states* of the polymer. The large effect originates from the interaction of the local linear polarization of the triplet-triplet absorption with the linear birefringence of the surrounding polymer matrix and emphasizes the role of long range molecular order in explaining the exceptionally large CD effects observed in chiral conjugated polymers.

The band shape of the CD as observed for the pristine films of chiral polyfluorene (with g_{abs} as intensive property) is also found in solutions of the polymer in mixture of solvents. A molecularly dissolved solution of the polymer in chloroform does not show CD because the polymer chains are far from each other and hence intermolecular attraction is minimal. On adding non-solvent methanol to chloroform solution, the polymer chains become less soluble in the solution mixture and interact with each other resulting in CD. This CD has same band shape and sign as CD observed for the thin pristine films of the polymer. Dynamic light scattering suggest formation of smaller aggregates. The CD of these aggregates can be interpreted to arise at molecular length scale. Similar CD is also obtained on cooling the dilute octanol solutions of the polymer from 90 °C to -10 °C. This CD is also classified as a characteristic of α -phase. However, on slow cooling concentrated polyfluorene solutions, a β -phase is formed having a different CD than the one seen in α -phase. This β -phase is found to be concentration and cooling rate dependent suggesting dependence on slow dynamics and dependence on the amount of material. Surprisingly, the β -phase is found to be form via a precursor formation. This precursor is interpreted as a small nucleus containing few intertwined polymer helices. The idea is supported by the monosignate nature of the CD. Interestingly, the occurrence of difference polymorphs like α -phase, β -phase, and precursor arising due to secondary and tertiary interactions provide a good example of synthetic polymer displaying aggregating behavior analogous to a natural polymer like DNA. It would be interesting if the β -phase formed in solution could be transferred to the film providing a relatively easier access of this highly organized phase in films, which otherwise is obtained by some cryptic techniques.

Therefore in achieving the aim of the thesis, we firstly established the intensive and extensive properties of the chiral polymers and later investigated their origins to molecular organizations. Furthermore, with that knowledge we investigated chiroptical properties in films and in solutions. Adding another facet to the current knowledge we have gained using circular polarized spectroscopy on chiral π -conjugated polymers, we investigated a p-n junction device. Here an application of polarized spectroscopy in SE provides us information at an electronic charge level like for example, about charge carrier density and depletion width in n-p junction comprising of a layer of ZnO nanoparticles and PEDOT:PSS.

In the thesis experimental evidence has been presented supporting the usefulness of circularly polarized light to probe the molecular organization on various length scales. It has been shown that spectroscopy with circularly polarized light is very sensitive to long range helical order in films of polyfluorenes. This long range ordering gives rise to various related effects like circularly polarized scattering, reflection, and CD in photoinduced absorbance. The information provided in the thesis on the origin of long range order and its interaction with the light could act as a starting point to performing similar studies on various other π -conjugated polymers. Understanding the molecular organization of π -conjugated polymers at various length scales would allow us to manipulate their optoelectronic properties in a desired way.

Probing π -conjugated polymers with circularly polarized light

Summary

In this thesis, we use circular polarized light to study aggregation in π -conjugated polymers at various structural levels. The importance of this study stems from the necessity to understand polymer packing and aggregation in thin films, used as active layer in opto-electronic devices like solar cells and light-emitting diodes. A systematic study on understanding polymer aggregation would provide freedom to tune the opto-electronic properties of the polymer in desired fashion.

π -conjugated polymer have a backbone consisting of alternating single and double bonds, which gives these polymers semiconducting properties and creates optical transitions in visible wavelength region. These opto-electronic properties depend strongly on the conformation of the polymer backbone and on interchain contacts arising from aggregation of polymer chains. Here we use circularly polarized light to probe the optical, conformational and electronic properties of π -conjugated polymers. This thesis focuses on *chiral* π -conjugated polymers. *Chirality* serves here as a spectroscopic ‘label’ allowing us to investigate aggregation and chiroptical properties of the polymer chains using circular dichroism (CD) spectroscopy.

CD spectroscopy allows us to study differential absorption between left and right handed circularly polarized light. The dissymmetry ratio in absorbance is often termed as g_{abs} . The g_{abs} can be independent of the amount of the material, in which case the g_{abs} can be regarded as *intensive* property of the material. On the other hand, if it is dependent on the amount of the material, g_{abs} can be associated as the *extensive* property. Chapters 2 and 3 utilize these definitions to study the intensive and extensive properties of chiral polythiophene and chiral polyfluorene respectively. Chapter 3 divulges further into the origins of the intensive and extensive nature of g_{abs} , hence outlining the polymer aggregation at different structural levels.

On investigating poly[3-((3*S*)-3,7-dimethyloctyl)thiophene] (PT811), g_{abs} was found to be independent of the film thickness (Chapter 2). Thus the g_{abs} in this case can be regarded as intensive, originating from a chiral molecular organization on a length scale < 50 nm. Having understood the intensive nature of g_{abs} , a detailed study on aggregation of poly[9,9-bis((3*S*)-3,7-dimethyloctyl)-2,7-fluorene] (PF811) was carried out (Chapter 3). It was found that pristine films of PF811 also show g_{abs} that is independent of the film thickness and hence can be regarded as intensive in nature. AFM reveals that the polymer chains collapse into

fibrillous aggregates upon spin coating the solutions of PF811. Similar CD effects were also observed in solution by inducing aggregation in polymer chains by adding a non-solvent (MeOH) to molecularly dissolved solutions of PF811 in chloroform. These aggregates can be transferred from solution to film. These films also show similar fibrillous aggregates. This suggests that the intensive g_{abs} is probably related to chiral arrangement of a few polymer chains within a fibril. Interestingly, it was found that thermally annealed films of PF811 show g_{abs} dependent of the thickness of the film, indicating that here the CD effects arise on a larger length scale (>50 nm). The AFM shows retention of fibrils, suggesting long range ordering of fibrils, probably cholesteric in nature.

Chapters 2 and 3 dealt with the differential absorbance of circularly polarized light in transmission mode. However, information about polymer aggregation can also be extracted from reflection and scattering of circularly polarized light, which is emphasized in Chapter 4. It was observed that the annealed films of PF811 show a CD effect for $\lambda > 450\text{nm}$, even though polymer does not absorb in this wavelength range. This anomalous behavior was investigated via a tailor-made setup and it was found that this *apparent* CD is a result of selectivity in scattering of left and right circular polarized light by the polymer film.

Interestingly CD effects are also observed in triplet-triplet photoinduced absorbance of the PF811 polymer (Chapter 5). The large CD observed here most likely arises from interaction of the linearly polarized photoinduced transition T_1 - T_n with the surrounding birefringent matrix of thermally annealed polymer.

Besides being an important blue light-emitting polymer, polyfluorenes (PFs) are also interesting because they can occur in α and β aggregates, each having its own optoelectronic properties. Processing conditions are of paramount importance in promoting the aggregation/phase. Through temperature dependent CD studies of PF811 in 1-octanol, these aggregates could be identified by their different CD spectra for the first time (Chapter 6). It was discovered that dilute solutions often yielded α -aggregates, whereas slow controlled cooling of concentrated solutions led to formation of β -aggregates. Remarkably though, β -aggregates were found to appear only via formation of a precursor involving cooperative folding of two or more chains.

Rod-like behavior of PFs is well known and anisotropy in achiral PF films has already been established by their different in-plane and out-of-plane optical constants obtained by spectroscopic ellipsometry (SE). Here one essentially measures the change of linearly polarized light into elliptically polarized light upon reflection from the polymer film. The anisotropic dielectric tensor of chiral polyfluorene is determined *via* variable angle spectroscopic ellipsometry and circular dichroism spectroscopy (Chapter 7). The anisotropy was found to be influenced by high in-plane alignment of polymer chains in the thin film. Chirality of the polymer results in small but non-zero off diagonal matrix elements in the dielectric tensor. Subsequently, optical rotation and ellipticity in reflection are predicted for pristine film of chiral polyfluorene.

In all previous chapters circular polarized light has been mostly employed to investigate optical and conformational aspects of π -conjugated polymers. Chapter 8 utilizes polarized

light to study electronic properties of π -conjugated polymer in p-n junction device involving poly(ethylenedioxythiophene):poly(styrenesulfonate) (PEDOT:PSS) and ZnO. The Moss-Burstein shift, *i.e.* an apparent increase of the optical band gap, is observed upon UV illumination of a layer of 5 nm ZnO nanoparticles in O₂-free atmosphere using spectroscopic ellipsometry. This shift is caused by populating the conduction band with excess free charge carriers and depleting the valence band. The free charge carrier density was determined to be $2 \times 10^{19} / \text{cm}^3$, about one carrier per particle. The shift can be reversed by introduction of O₂. For junctions of ZnO nanoparticle layers with a pH neutral PEDOT:PSS conducting polymer layer a depletion width of 5 nm in ZnO is observed under UV illumination in O₂-free atmosphere. At the junction free charge carriers in ZnO are transferred to neutral-PEDOT:PSS causing a slight reduction of the latter.

Het onderzoeken van π -geconjugeerde polymeren met circulair gepolariseerd licht

Samenvatting

In dit proefschrift wordt circulair gepolariseerd licht gebruikt om de assemblage van π -geconjugeerde polymeren op verschillende lengteschalen te onderzoeken. Het belang van deze studie komt voort uit het feit dat de polymeerpakking (assemblage) in dunne lagen een rol speelt in toepassingen zoals zonnecellen en lichtemitterende diodes. Een systematisch onderzoek naar de assemblage van π -geconjugeerde polymeren kan bijdragen aan het verkrijgen en verbeteren van de gewenste opto-elektronische eigenschappen.

π -geconjugeerde polymeren hebben een moleculaire structuur die bestaat uit afwisselende enkele en dubbele bindingen. Dit leidt tot een polymeer met halfgeleidende eigenschappen en optische overgangen in het zichtbare golflengtegebied. De opto-elektronische eigenschappen hangen sterk af van de conformatie van de polymeerketens en van hun onderlinge interacties. In dit proefschrift wordt circulair gepolariseerd licht gebruikt om de optische, conformationele en elektronische eigenschappen van chirale π -geconjugeerde polymeren te onderzoeken. *Chiraliteit* wordt toegepast als een spectroscopisch 'label' om de assemblage van de polymeerketens te onderzoeken met circulair dichroïsme (CD) spectroscopie.

CD spectroscopie meet verschillen in absorptie tussen links en rechts circulair gepolariseerd licht. Een maat voor dit verschil is de dissymmetrie ratio g_{abs} . De g_{abs} kan onafhankelijk zijn van de hoeveelheid materiaal en in dit geval kan de g_{abs} als intensieve grootheid van het materiaal worden beschouwd. Echter als g_{abs} wel afhankelijk is van de hoeveelheid materie, dan is g_{abs} een extensieve eigenschap. In de Hoofdstukken 2 en 3 worden deze definities gebruikt om de chiroptische eigenschappen van films gemaakt uit chiraal polythiofeen of chiraal polyfluoreen te onderzoeken.

Voor films van poly[3-((3*S*)-3,7-dimethyloctyl)thiofeen] (PT811) bleek g_{abs} onafhankelijk te zijn van de laagdikte (Hoofdstuk 2). In dit geval is g_{abs} een intensieve materiaal eigenschap die zijn oorsprong vindt in de chirale moleculaire organisatie op een lengteschaal kleiner dan 50 nm. Vervolgens is een gedetailleerde studie uitgevoerd naar de assemblage van poly[9,9-bis((3*S*)-3,7-dimethyloctyl)-2,7-fluoreen] (PF811) (Hoofdstuk 3). Ook voor polymeerlagen van PF811, gedeponereerd vanuit oplossing met behulp van spin-coating, is g_{abs} onafhankelijk van de dikte van de laag en is het CD signaal dus intensief. Uit AFM blijkt dat de polymeerketens geassembleerd zijn in fibrilachtige structuren tijdens het drogen van de film. Vergelijkbare CD effecten zijn waargenomen in oplossingen van de polymeerketens waarin de assemblage was gestimuleerd door toevoeging van een slecht oplosmiddel (MeOH) aan een moleculair opgeloste oplossing van PF811 in chloroform. Het was mogelijk om de

aggregaten vanuit de oplossing over te dragen naar een oppervlak. Deze lagen vertoonden vergelijkbare fibrilachtige structuren. Dit suggereert dat de intensieve g_{abs} aan een chirale pakking van enkele polymeerketens in een fibril kan worden gerelateerd. Thermisch behandelde lagen van PF811 vertoonden een g_{abs} die wèl van de laagdikte afhankelijk is, wat aangeeft dat deze CD effecten samenhangen met een moleculaire organisatie op een grotere lengteschaal (> 50 nm). De AFM opnames duiden op de aanwezigheid van fibrilachtige structuren. Dit suggereert een organisatie over een grote lengteschaal waarin deze fibrillen geordend zijn op een vergelijkbare manier als de moleculen in een cholesterisch vloeibaar kristal.

De eerste twee hoofdstukken behandelden de selectieve absorptie van circulair gepolariseerd licht. Informatie over de polymeerassemblage kan ook met reflectie en verstrooiing van circulair gepolariseerd licht worden verkregen. Dit is verder onderzocht in Hoofdstuk 4. Thermische behandelde lagen van PF811 tonen een CD effect voor golflengtes van licht boven 450 nm. In dit golflengtegebied absorbeert het polymeer geen licht meer. Dit effect is bestudeerd met een zelfgemaakte opstelling waarmee selectiviteit in de reflectie en verstrooiing van inkomend circulair gepolariseerd licht door de polymeerfilm gemeten kan worden. In dit geval bleek selectiviteit in verstrooiing van licht het schijnbare CD effect kwantitatief te kunnen verklaren.

CD effecten zijn ook in de fotogeïnduceerde triplet-triplet absorptie van het polymeer worden waargenomen (Hoofdstuk 5). Deze relatief sterke CD effecten worden toegeschreven aan een moleculaire organisatie op een grote lengteschaal in de film van het thermische behandelde polymeer in combinatie met lineaire polarisatie van de fotogeïnduceerde triplet-triplet overgang.

Polyfluorenen zijn interessant omdat ze zowel een α - als β -fase vertonen. Deze twee fases kunnen, op grond van hun karakteristieke opto-elektronische eigenschappen herkend worden. De omstandigheden tijdens de depositie zijn cruciaal voor de mate en onderlinge verhouding waarin de twee fases voorkomen. De afzonderlijke fases zijn voor het eerst geïdentificeerd met temperatuurafhankelijke CD metingen (Hoofdstuk 6). Het afkoelen van sterk verdunde oplossingen van PF811 in 1-octanol, geeft overwegend de α -fase, terwijl bij het langzaam afkoelen van een geconcentreerde oplossing, de β -fase domineert. Aangetoond is dat de β -fase alleen via een zogenoemde voorloper-fase wordt gevormd. De vorming van de voorloper-fase wordt voorgesteld als een coöperatieve vouwing van twee of meer polymeerketens.

Na het ophelderen van de moleculaire organisatie van polyfluoreen in dunne lagen, worden, in een volgende stap, de optische eigenschappen van dunne films van het chirale polymeer bepaald met behulp van spectroscopische ellipsometrie (SE) (Hoofdstuk 7). Deze optisch eigenschappen blijken anisotroop te zijn, een feit dat al bekend was voor achiraal polyfluoreen. De gemeten anisotropie duidt op een uitlijning van de polymeerketens in het vlak van de dunne laag. De chiraliteit van het polymeer resulteert in waarden voor de niet-diagonaal elementen van de diëlektrische tensor die ongelijk aan nul zijn. Een procedure voor het afschatten van de grootte van deze niet-diagonaal elementen uit het CD spectrum van de dunne laag is beschreven. Volgens sommige theorieën leiden deze niet-diagonaal elementen

to selectieve reflectie van circulair gepolariseerd licht door de film voor licht invallend langs de normaalvector van het oppervlak en ook draaiing van het polarisatie vlak van het licht na reflectie langs de normaal. De grootte van deze selectiviteit en draaiing is afgeschat met behulp van de waarden bepaald voor de diëlektrische tensor. De selectiviteit in reflectie blijkt klein te zijn en qua grootte vergelijkbaar met de detectielimiet van bestaande meetmethodes.

In de voorafgaande hoofdstukken is circulair gepolariseerd licht voornamelijk gebruikt om de conformationele aspecten van π -geconjugeerde polymeren te onderzoeken. In Hoofdstuk 8 wordt gepolariseerd licht toegepast om de eigenschappen een p - n junctie bestaande uit poly(ethyleendioxythiofeen)-poly(styreensulfonaat) (PEDOT:PSS) en ZnO. In deze juncties leidt fotodoping van ZnO door UV licht tot de vorming van vrije ladingsdragers. De aanwezigheid van de ladingdragers kan worden vastgesteld aan de hand van een verandering in de bandafstand. Hier leidt de aanwezigheid van ladingen tot een blauwverschuiving van de absorptieband, ook wel bekend als de Moss-Burstein verschuiving. Na UV belichting van een dunne laag van ZnO nanodeeltjes in een zuurstofvrije omgeving kon, met behulp van spectroscopische ellipsometrie, de Moss-Burstein verschuiving worden waargenomen. De dichtheid aan vrije ladingsdragers bleek $2 \times 10^{19} / \text{cm}^3$ te zijn, wat overeen komt met ongeveer één lading per nanodeeltje. De Moss-Burstein verschuiving kan door blootstelling aan zuurstof weer ongedaan worden gemaakt. Voor juncties tussen een laag van ZnO nanodeeltjes en een laag van het geleidende PEDOT:PSS met neutrale pH waarde kon berekend worden dat vrije ladingsdragers elektrostatische barrière van 5 nm moeten doorkruisen om van de ZnO laag in the polymeerlaag te kunnen komen. Deze afstand is kort genoeg voor goed elektrisch contact. De elektrostatische barrière ontstaat doordat op het grensvlak van de ZnO en polymeer laag, vrije ladingsdragers worden overgedragen van ZnO aan PEDOT:PSS waardoor deze laatste laag een klein beetje wordt gereduceerd.

Acknowledgements

It doesn't seem long since the time I was roaming around the corridor of STO 4 with a blue sheet in my hand introducing myself to people and getting their signatures. Four years have passed now- the color of the sheet has now changed to red, work is condensed to odd number of papers. What I walk away with is loads of experience, a unique approach to science and some very fond memories of friends.

First and foremost, I thank my promoter Prof. René Janssen for giving me the opportunity to be part of the research project, detailed results of which are mentioned in this thesis. Though we have drastically different choices when it comes to sport- I love to watch a patient game of five day test cricket whereas he is fanatic about fast paced soccer, yet when it came to research we could find common ground. I thank him here for showing enormous patience with me and my approach to the subject. For any question, I could always knock on his door to get immediate attention.

I am grateful to Dr. Stefan Meskers for being my supervisor. Besides being a very meticulous researcher, his passion to educate students makes him an incredible scientist. His style of teaching is very much reminiscent to Feynman lectures. During my stay at the MST, I have learnt a lot from him. He has been a great motivator and critic at the same time. I credit him a lot for the way I think now about my future research and science in general.

I would like to express my gratitude to Prof. Dieter Neher, Prof. Thierry Verbiest, Dr. Albert Schenning for being part of my reading committee and Prof. Bert Meijer and Prof. Dick Broer for the extended defense committee. I thank all of them for having read the thesis critically and providing valuable feedback.

I thank Dr. Robert Abbel and Maarten Pouderoijen for gifting me with the polyfluorene polymer and Dr. Guy Koeckelberghs for providing the polythiophene polymer. I acknowledge their efforts in synthesizing the polymer which provided me with a great subject for study. I express my gratitude to Jeroen Gielen, Dr. Peter Christianen, Dr. Wouter Habraken, Dr. Jos Lavèn for help with dynamic light scattering measurements, Dr. Martijn Kemerink for help with AFM, Jan Gilot with making of ZnO memory devices, and Auke Kronemeijer for Kelvin probe measurements. All these collaborations have resulted in good scientific discoveries. I thank Roel Roijmans for the kick start of Chapter 8. His courageous attempt to take on ellipsometry as his two month internship project is remarkable.

Thanks to Subi, Martin, Karthik, and Oren for valuable discussions on research and life in general. It was incredible the way we could discuss research so spontaneously, doesn't matter if we were standing in the corridors or enjoying a drink or out for dinner. A round of applause to office mates David, Emilie, Rafael, Jorge, Martin, Dirk, Robert, Marie-France, Arantxa, Daniele, Bram, and Stefan for having tolerated me and my erratic nature.

I have been really lucky for having found good set of friends here. They have really made me feel at home. I would miss playing pranks on Sai, to irritate Arantxa, sharing food recipes

with Nandini, beer tasting with Anish, habitual coffee breaks with mC, nerdy chats with Andreas, down to earth conversations with Yogesh and Nilesh, discussing South Park with Daniele, and family dinners with the godfather Guisseppe and mum Kate. I feel indebted to Trent, Roger, Cartman, Eddie, Syd, and David for being the best imaginary friends. Without you guys, I would have let my frustrations get the better of me. Cheers to the Fellenoord club, I really enjoyed some great tennis out there. Four years is a long time to meet and know a lot of people but there are only very few who leave an everlasting impression on you. These are the ones whom you would never like to part with. Anish and mC are the ones for me. You guys have been the best through thin and thick.

I am great believer that much credit of having survived a PhD goes to your own perseverance, basically your own nature. And nature of a human being depends a lot on the upbringing that puts one in a position to take up various challenges in life. I thank my parents and my brother for being the motivating force behind it. Without them, I wouldn't have been here penning down a whole book. I would also like to thank my teachers through my IITK years who have inspired me to learn and educate.

In between all the numbers and equations lies a design to express a scientific phenomenon, much like what drawings would do for architects. I am sure Debjani would agree with me on this. I think our critical evaluations of each other's work have been very constructive in shaping up this thesis. Notwithstanding my reluctance to understand architecture, the way you accommodated my research work and motivated me throughout is incredible. You made things simple for my complicated brain! No wonder I have survived...

- g^L

Curriculum vitae

Girish Lakhwani was born on July 2nd, 1980 in Kanpur, India. He obtained his integrated Masters degree in Chemistry in 2005 from the Indian Institute of Technology, Kanpur, India. As part of his graduation project, he worked under the guidance of prof. V. Chandrasekhar on the stabilization of ZnS nanoparticles by pyrazolyl substituted acrylate based polymers. He has also been involved in several summer internships at Hyderabad Central University, India in 2002, at Eindhoven University of Technology, The Netherlands in 2003, and at McMaster University in Hamilton, Canada in 2004.

Following up on his summer internship in 2003 on organic photovoltaics, he started his PhD in September 2005 in the same group Molecular Materials and Nanosystems, under the supervision of prof.dr.ir. R.A.J. Janssen and dr. S.C.J. Meskers. His work on using circular polarized light as a tool to investigate π -conjugated polymers is described in this thesis. Part of the work has been published in scientific journals.

